Continuous reconstruction of Holocene fluctuations of Brunnifirn, Swiss Alps: Combining geomorphological mapping and ice-flow modeling

GEO 511 Master's Thesis

Author
Jonathan Davidson
17-714-429

Supervised by
Prof. Dr. Andreas Vieli
Dr. Samuel Nussbaumer

Faculty representative
Prof. Dr. Andreas Vieli

30.06.2023
Department of Geography, University of Zurich

Continuous reconstruction of Holocene fluctuations of Brunnifirn, Swiss Alps: Combining geomorphological mapping and ice-flow modeling

GEO 511 Master's Thesis

Jonathan Davidson
jonathanmelvin.davidson@uzh.ch

Department of Geography
University of Zurich

Supervised by
Prof. Dr. Andreas Vieli
Dr. Samuel Nussbaumer

Faculty representative
Prof. Dr. Andreas Vieli

June 30, 2023

Abstract

Fluctuations of glaciers throughout the Holocene have not been uniform in the Swiss Alps. Numerous static reconstructions based on landforms have highlighted the complexity of clearly constraining past glacier fluctuations. Minimal extents are often unidentified, and reactions of glaciers to climate signals sometimes contradict. This thesis presents an approach going beyond static maximum extent reconstructions. By forcing a time-dependent 2-D ice-flow model with proxy temperature reconstructions, continuous dynamic fluctuations were created. Contrary to traditional approaches, the lag in response of glaciers to climate changes was thus included. Landforms documented with geomorphological mapping constrained the modeled fluctuations.

Archeological finds above Brunnifirn (UR), which are the oldest known radiocarbon-dated artifacts of their type in the Alps (7.97–7.75 ka cal BP), inspired this thesis. Geomorphological mapping of landforms relevant to the constrain glacier fluctuations was conducted in the field and remotely. The numerical model was forced with ELA histories derived from temperatures of two long-term Holocene proxy curves to model the last 9000 years. For the last 500 years, high-resolution yearly data for the Alps were applied.

Modeling results suggest that the artifacts were deposited after a glacial retreat following a strong advance forced by the 8.2 ka event, of which no moraines were found. Fluctuations show consistency with a peat bog radiocarbon dated to ca 3.75 ka cal BP, but they vary strongly between the two temperature forcings applied. Modeling implies that from 9 ka onwards, Brunnifirn was rarely larger than the Little Ice Age (LIA) maximum extent, with minimal extents similar to the extent of 2019. Hardly any evidence of extents before the LIA were found with geomorphological mapping, making the modeled fluctuations more compelling. The modeling of the LIA after 1500 CE shows an advance with three culminations, two of which reach the mapped moraine. The field mapping confirms the idea of two or more similar extents, as a double ridge was documented in the LIA moraine complex.

Model projections for the future based on a range of climate scenarios demonstrate that before the end of the century, Brunnifirn will retreat to the highest peak, beyond any Holocene minimum extent. This trend agrees with other future modeling scenarios for the Alps. The rates of retreat vary strongly between the different RCPs.

Acknowledgements

I want to express my gratitude to my supervisors, Prof. Dr. Andreas Vieli and Dr. Samuel Nussbaumer for guiding me through the process of this thesis. The countless meetings, support throughout modeling, and expertise on geomorphological mapping in the field offered by Prof. Dr. Andreas Vieli were central to accomplish this work. The contextual information, numerous consultations and encouragements, and knowledge in the field provided by Dr. Samuel Nussbaumer were fundamental. Thank you both.

I would also like to thank Marcel Cornelissen for sharing his archeological insights.

Furthermore, I would like to thank Dr. Dmitry Tikhomirov for introducing me to sampling boulders, and his work in the field. Thanks also to Franco Buglio for his support in the field. I am also thankful for the insight of Prof. Dr. Markus Egli on radiocarbon dating.

Many thanks to Sanne Schnyder and Samuel Bissig for their support in the field and the fruitful discussion about geomorphological landforms. I am happy that Céline Walker and I shared the process of the Master's thesis, as she helped countless times. Thanks to my friends for proofreading and the support.

Finally, I would like to thank my family and Patricia for being there, listening, consulting, and always believing in me.

Contents

1 Introduction 1

1.1 Motivation 1

1.2 Aims and research questions 2

1.2.1 Geomorphological mapping 2

1.2.2 Numerical modeling 2

1.3 Study area 4

1.4 Background 6

1.4.1 Overview of Holocene glacier fluctuations 6

1.4.2 Archeological context 7

1.4.3 Geomorphological mapping 7

1.4.4 Numerical modeling 8

2 Methods 9

2.1 Mapping 9

2.1.1 Field Mapping 11

2.1.2 Digital Remote Mapping 11

2.2 Landform Age Dating 13

2.2.1 Moraine soil and peat bog samples for radiocarbon dating 13

2.3 Flow modeling approach 17

2.3.1 Model Setup 17

2.3.2 Steady state and step change modeling 20

2.3.3 Sinus experiments 21

2.3.4 Transient experiments 21

2.3.5 1500–2020 CE 23

2.3.6 Holocene 25

2.3.7 Future glacier evolution 27

3 Results 30

3.1 Mapping 30

3.1.1 Field mapping 31

3.1.2 Remote mapping 35

3.2 Radiocarbon dating ... 39

3.3 ELA estimations ... 40

3.4 Numerical modeling ... 41

3.4.1 Steady state and step change ... 41

3.4.2 Response time ... 44

3.4.3 Sinus experiments ... 46

3.4.4 Sensitivity testing ... 50

3.4.5 1500–2020 CE modeling ... 53

3.4.6 Holocene modeling ... 58

3.4.7 Future modeling ... 64

4 Discussion ... 69

4.1 Mapped landforms and inferred extents of Brunnifirn ... 70

4.2 ELAs inferred from mapping and steady state modeling ... 75

4.3 Transient modeling for fluctuating climate ... 76

4.4 Assessing reconstructed fluctuations ... 86

4.5 Outlook ... 96

5 Conclusion ... 97

6 Appendix ... 105

Personal declaration ... 120

List of figures

Figure 1: Map of Brunnital with sample locations and archeological site. The 10Be ages of the sampled boulders will be processed after submission of this thesis. Background map: swisstopo (2023)....................5

Figure 2: Overview of glacier fluctuations throughout the Holocene in the Swiss and Western Alps, modified excerpt from Holzhauser (2010). Blue fluctuations stand for advances over the extent of glaciers in the year 2000 CE, retreats behind that level are marked in red. Question marks and the arrow stand for unknown duration or extent of fluctuations....................6

Figure 3: Map of Brunnital with sample locations. The 10Be ages of the sampled boulders will be processed after submission of this thesis. Background map: swisstopo (2023)............13

Figure 4: A) Image of the LIA moraine with two distinguishable ridges. The arrow indicates direction of (paleo-) ice flow. The sample for radiocarbon dating was taken in the outer ridge, so further downstream. B) Stable Surface that allowed for development of a soil in which the profile was dug. C) Close-up of soil profile. Photos: Jonathan Davidson in 2022....................15

Figure 5: A) Peat bog as viewed from below, the image is taken valley upwards. B) Profile of the peat bog. The sample for radiocarbon dating was taken from the lowest part of the hole. Photos: Jonathan Davidson in 2022....................16

Figure 6: Exemplary model output for a steady state ELA of 2700 m a.s.l. The map shows the ice surface elevation on the surface topography. The number in the upper left corner shows the run time (400 years). The colored lines are the flow lines of Brunnifirn (red), Staldenfirn (orange), and Glatscher da Strem (purple). The axis labels are rounded coordinates of the CH1903+/LV95 grid, one unit equals to 1 km....................20

Figure 7: The reconstructed temperatures from Casty et al. (2005a), the measured and interpolated from above 1000 m a.s.l. temperatures from MeteoSwiss (2023), and the combination of both which was used as forcing for modeling of 1500–2020 CE. Note how the reconstructed temperatures from Casty et al. (2005a) are too warm compared with the MeteoSwiss data from 1864 (beginning of MeteoSwiss data set) to almost 1950, which is why a cooling offset of 0.9 was applied....................24

Figure 8: The temperature reconstructions used for Holocene modeling. The gray dotted line is the average of the MeteoSwiss data from 1901–2000 (8.5019 °C). The offset for the GISP2 data was calculated in comparison with the average differences from the data for 1500–2020 CE (see Table 6). Note the strong variation of the GISP2 data. Nevertheless, the patterns are similar and clear signals like the 8.2 ka cooling are well visible in both reconstructions..........26

Figure 9: Exemplary CH2018 simulation (DMI-HIRHAM_ECEARTH) temperature projections for three RCPs for Disentis (closest station to Brunnifirn). The dotted lines are the respective trends. The displayed data is adjusted for Brunnifirn by fitting it to the >1000 m a.s.l. temperatures from MeteoSwiss (2023), as shown in Table 7....................28

Figure 10: Geomorphological map of the upper Brunnital, based on field mapping. A) The upper part of the valley and overview of everything that was mapped. The moraines and inferred ice flow directions (yellow arrows) give insight of past glacier extents and ice movement. B) Detail inset of the LIA moraine complex, with double ridge indicating multiple advances to the same position. C) Detail inset of the upper moraine cluster, where an abundance of moraine material was found......31

Figure 11: Transition from rounded to sharp deposited rocks, as mapped in Figure 10 (eastern line of the two mapped). The red line in image A shows the transition, where rounded material is found to the left of the line, and sharp material is deposited on the right side of the line. Image B is a close-up shot of the rounded material (assumably deposited by the glacier), image C shows the sharp material (assumably deposited by rockfall). Photos: Jonathan Davidson in 2022......33

Figure 12: A) Geomorphological map of the upper Brunnital, based on remote mapping with aerial images. Vegetation changes imply recent ice cover below the line. B) Detail inset of the LIA moraine complex, showing a second outer row of latero-frontal moraines to the orographic right, and supposed ridges as continuation of the frontal moraines on the orographic left. C) Detail inset of the upper moraine complex and numerous lateral moraines in the steep western valley slope. Most large moraines show clear ridges (bold purple lines) which indicate past ice extents. Background map: swisstopo (2023)......35

Figure 13: Classification of moraine types, based on aerial image and field mapping. Background map: swisstopo (2023)......36

Figure 14: Glacier outlines mapped from old aerial images. Note how the tongue position between 1979 and 1990 does not change. This is a result of excluding a piece of dead ice present in the 1979 image, because it is completely disconnected from the glacier tongue. Background map and old aerial images: swisstopo (2023)......37

Figure 15: Integrated map of geomorphological landforms which indicate past glacier extents. Elements of field and remote mapping are combined. Background map: swisstopo (2023)......38

Figure 16: Steady state lengths for a range of ELAs, for an advance and a retreat case (lowering or increasing ELA, respectively). Upper boundary: elevation of Oberalpstock; lower boundary: ELA causing Brunnifirn to flow into Maderanertal. Steady state was declared when the glacier did not change its length for at least 100 years......42

Figure 17: A) Detail of steady state lengths shown in Figure 16 better illustrate the hysteresis. Note that experiments where not conducted for all ELAs equally: for both decreasing and increasing ELA, 50 m increments were followed. However, additional experiments for smaller ELA variations were conducted irregularly. B) Glacier surface elevation along flow line. Light blue: steady state approximation of today's glacier surface (ELA: 2730 m a.s.l.). Dark blue: steady state surface reaching LIA moraine complex (ELA: 2585 m a.s.l.)......43

Figure 18: Sinus ELA forcing around an ELA0 of 2800 m a.s.l., with sinus periods of 20, 50, and 100 years. Even the rapid change in climate signal resulting from the 20-year period is visible in volume and length change. Length does not lag far behind volume change.............48

Figure 19: Sinus ELA forcing around an ELA0 of 2585 m a.s.l., with sinus periods of 20, 50, and 100 years. The rapid change in climate signal resulting from the 20-year period is not visible in length, however it can be observed in volume change. The lag of length changes is well illustrated..49

Figure 20: A) ELA forcing for the modeling of 1500–2020 CE with 10-year means (red line), derived from the summer temperature curve (Casty et al., 2005a; MeteoSwiss, 2023). B) Sensitivity experiment for 1500–2020 CE length evolution of Brunnifirn, using three different starting glacier surface steady state geometries (yellow, blue, and green lines). Length measurements (GLAMOS and aerial images) are displayed for comparison, and the gray dotted lines show today's extent and the possible LIA maximum extent. The red dot marks the glacier length on the Siegfried map (data content from 1859 CE, according to swisstopo, 2023).......52

Figure 21: A) ELA forcing for the modeling of 1500–2020 CE with 10-year means (red line), derived from the summer temperature curve (Casty et al., 2005a; MeteoSwiss, 2023). B) LIA fluctuations of Brunnifirn, Staldenfirn and Glatscher da Strem with the same ELA forcing (parameter configuration: ELA0 = 2720, ELA_{fc} = 130). The starting glacier surface geometry is a 2720 m a.s.l. ELA steady state. The blue box shows a range within Brunnifirn fluctuated over ca 250 years during the LIA period. The dashed gray lines show the 2019 extent of Brunnifirn and the position of the LIA moraine. The red dot marks the glacier length on the Siegfried map (data content from 1859 CE, according to swisstopo, 2023). Length measurements (GLAMOS and aerial images) are displayed for comparison...........................54

Figure 22: A) Brunnifirn LIA maximum modeling extent maintained from 1630–1650 CE. B) Modeling output of last LIA maximum reached ca 1870. Not only the LIA maximum moraine complex is matched, but also lateral moraines fit well with the modeled glacier extent. Also, the ice margins complement the supposed moraine ridges and moraine remnants..................55

Figure 23: A) Maximum extents of Staldenfirn and Glatscher da Strem during the modeling of 1500–2020 CE, output for 1610 CE. Bächenfirn, a glacier not quantified during modeling, flows towards the west. Note how ice extent match the mapped moraines. B) Detail inset for Staldenfirn flowing towards north and Bächenfirn flowing towards west, both ice extents matching large lateral moraines. Background map: swisstopo (2023).....................................56

Figure 24: Final output of the modeling for the year 2020, compared with the glacier outline 2019. Note how the south-eastern part of the plain is underrepresented by the model, where the glacier is debris-covered. Background map: swisstopo (2023)..57

Figure 25: LIA maximum extent of Brunnifirn based on modeling (output for 1640). Note how moraines in Val Cavardiras to the east are matched by the modeled ice extent. Background map: swisstopo (2023)...58

Figure 26: Holocene modeling around the period the archeological artifacts are dated for (red box in plot B). Modeling was started before the cold interval around 8.2 ka to eliminate bias of the starting glacier surface geometry (steady state for 2700 m a.s.l. ELA). A) ELAs calculated for GISP2 and Milandre temperature reconstructions (ELA0 = 2720, ELA_{fc} = 130), with nearest neighbor interpolation between data points. B) Brunnifirn length modeled from the two different ELA calculations. The gray dotted lines show known glacier extents as reference, the green dotted line shows the position of the peat bog which was radiocarbon age dated to ca 3.8–3.5 ka BP........60

Figure 27: Model output reaching the upper moraine cluster (steady state ELA = 2650 m a.s.l.), displayed with moraines mapped during field and remote mapping (no differentiation between mapping method for better readability). This extent is reached multiple times throughout the Holocene, especially for the Milandre-forced glacier (Figure 28)..........62

Figure 28: Holocene modeling for the whole analyzed period from 9 ka until today, including steady ELA from the year 2021 CE onwards until 2100 CE. Starting geometry: no ice. A) ELAs calculated for GISP2 and Milandre temperature reconstructions (ELA0 = 2720, ELA_{fc} = 130), with nearest neighbor interpolation between data points. LIA temperature reconstruction (Casty et al., 2005a; MeteoSwiss, 2023) from 1500 CE onwards, with 10-year means (red line). B) Brunnifirn length modeled from the two different ELA calculations. The gray dotted lines show known glacier extents as reference, the green dotted line shows the position of the peat bog which was radiocarbon age dated to ca 3.8–3.5 ka..........64

Figure 29: Future evolution of Brunnifirn for constant climate from 2020 onwards (2942 m a.s.l. = average ELA from 1990–2019). A) ELA with 10-year means (red line). Evolution from 1500–2019 CE modeling with parameter configuration of: ELA0 = 2720, ELA_{fc} = 130. B) Length evolution compared with length measurements (GLAMOS and aerial images). The length reached after 1950 when no more change occurs represents a steady state to the average climate from 1990–2019..........65

Figure 30: Future evolution of Brunnifirn from 1981–2099 CE for three RCPs (CH2018 simulation DMI-HIRHAM_ECEARTH), with result 1980 CE result of the 1500–2020 CE modeling. A) The bold lines are trends for the three RCPs. B) The almost vertical length change before 2060 CE marks the disappearance of a large dead ice body that remains in the plain. The steep upper part of the glacier however disconnects from the part in the plain already around 2030–2040 CE..........67

Figure 31: Hypothetical ice surface output for 2050 CE based on the DMI-HIRHAM_ECEARTH simulation. A) RCP2.6. B) RCP4.5. C) RCP8.5. Note the ice disconnected from the steep section in the center of the plain, which is counted as maximal glacier length as it is located on the flow line, causing a false length measurement. Background map: swisstopo (2023)..........68

Figure 32: Transition from Milandre and GISP2 modeling to the last 500 years. A) ELA forcing derived from the GISP2 and Milandre temperature reconstructions until 0.45 ka, from then on, the forcing of the last 500 years is applied (with 10-year means as red line). B)

Fluctuations based on the forcings. Note how temperatures of the GISP2 and Milandre record are already cooling before 1500 CE (i.e., 0.45 ka BP) but the result of the last 500 years similar: after an initial advance just before 1550 CE, the maximum is reached around 1630 CE. After a smaller third maximum, a period of retreat follows. Finally, there is a last readvance, transitioning into a strong retreat until today........77

Figure 33: A) Possible LIA maximum of Tschingelfirn. B) Possible Holocene maximum as reaction to the 8.2 ka cooling recorded in the Milandre-derived ELA forcing. Both are just possible maxima, as the length of Tschingelfirn was not recorded. Maxima of Staldenfirn and Glatscher da Strem were used as indicators. Note how the central moraine ridge in A) and the lateral moraine in B) fit the modeled ice extent. Background map: swisstopo (2023)................79

Figure 34: ELA and corresponding glacier lengths extracted from the results of the last 500 years modeling period (one value per year). The time scale corresponds to the modeled period from 1500–2020 CE........83

Figure 35: ELA and corresponding glacier volumes extracted from the results of the last 500 years modeling period (one value per year). The time scale corresponds to the modeled period from 1500–2020 CE........84

Figure 36: ELA and corresponding glacier lengths extracted from the results of the last 500 years modeling period (one value per year), with the steady state modeling length results in the background (magenta). The time scale corresponds to the modeled period from 1500–2020 CE........85

Figure 37: Culminations during the modeling of 1500–2020 CE. Note that until 1499 CE (0.451 ka), the long-term temperature data is used (Affolter et al., 2019b; Alley, 2004). From then onwards, the high-resolution temperature data is applied (Casty et al., 2005a; MeteoSwiss, 2023). The first culmination is thus more distinct than in the modeling from only 1500 CE on (see Figure 21), as the long-term data force the advance already before 1500 CE. Nevertheless, the first maximum at ca 1540–1550 CE (0.41–0.4 ka) is reproduced with all temperature forcing curves........87

Figure 38: The modeled fluctuations of Brunnifirn (forced with the high-resolution data by Casty et al., (2005) and MeteoSwiss (2023)) in comparison to cumulative length changes from the LIA maximum of Unterer Grindelwaldgletscher and Gornergletscher (data from Nussbaumer et al., 2011). The LIA moraine of Brunnifirn corresponds to the LIA maximum. The patterns of culminations are similar, the timing however is different..............89

Figure 39: Possible minimal extents of Brunnifirn during the period to which the artifacts were dated, based on the two different climate forcings (extract of 7.75 ka). A) Milandre temperature forcing. B) GISP2 forcing. Background map: swisstopo (2023).........................91

Figure 40: A) Modeled fluctuations of Brunnifirn based on the different temperature reconstructions (Affolter et al., 2019b; Alley, 2004; Casty et al., 2005a; MeteoSwiss, 2023). B) glacier fluctuations throughout the Holocene in the Swiss and Western Alps, modified excerpt from Holzhauser (2010). Blue fluctuations stand for advances over the extent of glaciers in the

year 2000 CE, retreats beneath that level are marked in red. Question marks and the arrow stand for unknown duration or extent of fluctuations. C) Fluctuation scenario of Rhonegletscher, modified except from Goehring et al. (2011), where red areas stand for an extent smaller than in 2011 CE, and blue areas stand for an extent larger than in 2011 CE. Shaded parts show transitional periods......93

Figure 41: Geomorphological map of the whole area mapped based on aerial images. Background map: swisstopo (2023)......106

Figure 42: Steady state output with an ELA of 2730. This is the closest approximation of a steady state to today's extent, as lowering the ELA by just a few meters leads to the steady state extent overflowing the edge of the plain. But compared to the mapped 2019 aerial image glacier outline, the model underestimates the ice extent in the eastern part of the plain but overestimates the eastern flank of Oberalpstock and Staldenfirn and Glatscher da Strem. Background map: swisstopo (2023)......106

Figure 43: Sinus ELA forcing around an ELA0 of 2720 m a.s.l., with sinus periods of 20, 50, and 100 years......107

Figure 44: Sinus ELA forcing around an ELA0 of 2730 m a.s.l., with sinus periods of 20, 50, and 100 years......108

Figure 45: (A) ELA history used for LIA modeling, with ELA0 = 2700 and ELA_{fc} = 120. (B) Plot of the length evolution of Brunnifirn with different steady state starting ice geometries (yellow, orange, and green line). The blue line represents an overlap of at least two of the curves, therefore also showing the point when the glacier has adjusted to the climate signal, independent of the input. The red dot is the glacier length on the Siegfried map (data content from 1859 CE, according to swisstopo, 2023). The red crosses display the measurements recorded by GLAMOS......109

Figure 46: (A) ELA history used for LIA modeling, with ELA0 = 2720 and ELA_{fc} = 120. (B) Plot of the length evolution of Brunnifirn with different steady state starting ice geometries (yellow, orange, and green line). The blue line represents an overlap of at least two of the curves, therefore also showing the point when the glacier has adjusted to the climate signal, independent of the input. The red dot is the glacier length on the Siegfried map (data content from 1859 CE, according to swisstopo, 2023). The red crosses display the measurements recorded by GLAMOS......110

Figure 47: (A) ELA history used for LIA modeling, with ELA = 2730 and ELA_{fc} = 120. (B) Plot of the length evolution of Brunnifirn with different steady state starting ice geometries (yellow, orange, and green line). The blue line represents an overlap of at least two of the curves, therefore also showing the point when the glacier has adjusted to the climate signal, independent of the input. The red dot is the glacier length on the Siegfried map (data content from 1859 CE, according to swisstopo, 2023). The red crosses display the measurements recorded by GLAMOS......111

Figure 48: (A) ELA history used for LIA modeling, with ELA0 = 2700 and ELA_{fc} = 130. (B) Plot of the length evolution of Brunnifirn with different steady state starting ice geometries (yellow, orange, and green line). The blue line represents an overlap of at least two of the curves, therefore also showing the point when the glacier has adjusted to the climate signal, independent of the input. The red dot is the glacier length on the Siegfried map (data content from 1859 CE, according to swisstopo, 2023). The red crosses display the measurements recorded by GLAMOS.........112

Figure 49: (A) ELA history used for LIA modeling, with ELA0 = 2720 and ELA_{fc} = 100. (B) Plot of the length evolution of Brunnifirn with different steady state starting ice geometries (yellow, orange, and green line). The blue line represents an overlap of at least two of the curves, therefore also showing the point when the glacier has adjusted to the climate signal, independent of the input. The red dot is the glacier length on the Siegfried map (data content from 1859 CE, according to swisstopo, 2023). The red crosses display the measurements recorded by GLAMOS.........113

Figure 50: Holocene modeling of the period the archeological artifacts are dated for (red box in plot B). Modeling was started well before the cold interval around 8.2 ka to eliminate any bias of the input geometry (steady state for 2720 m a.s.l. ELA). A) ELAs calculated for GISP2 and Milandre temperature reconstructions (ELA_{fc} = 130), with linear interpolation between data points. B) Brunnifirn length modeled from the two different ELA calculations. The gray dotted lines show known glacier extent as reference, the green dotted line shows the position of the peat bog which was radiocarbon age dated to ca 3.8–3.5 ka BP.........114

Figure 51: CH2018 simulation (MPICSC-REMO1_MPIESM) temperature projections for three RCPs for Disentis (closest station to Brunnifirn).........115

Figure 52: CH2018 simulation (MPICSC-REMO2_MPIESM) temperature projections for three RCPs for Disentis (closest station to Brunnifirn).........115

Figure 53: CH2018 simulation (SMHI-RCA_ECEARTH) temperature projections for three RCPs for Disentis (closest station to Brunnifirn).........116

Figure 54: Future evolution of Brunnifirn from 1981–2099 CE for three RCPs (CH2018 simulation MPICSC-REMO1_MPIESM), with result 1980 CE result of the 1500–2020 CE modeling. A) The bold lines are trends for the three RCPs. B) The almost vertical length change before 2060 CE marks the disappearance of a large dead ice body that remains in the plain. The steep upper part of the glacier however disconnects from the part in the plain already around 2030–2040 CE.........117

Figure 55: Future evolution of Brunnifirn from 1981–2099 CE for three RCPs (CH2018 simulation MPICSC-REMO2_MPIESM), with result 1980 CE result of the 1500–2020 CE modeling. A) The bold lines are trends for the three RCPs. B) The almost vertical length change before 2060 CE marks the disappearance of a large dead ice body that remains in the plain. The steep upper part of the glacier however disconnects from the part in the plain already around 2030–2040 CE.........118

Figure 56: Future evolution of Brunnifirn from 1981–2099 CE for three RCPs (CH2018 simulation SMHI-RCA_ECEARTH), with result 1980 CE result of the 1500–2020 CE modeling. A) The bold lines are trends for the three RCPs. B) The almost vertical length change before 2060 CE marks the disappearance of a large dead ice body that remains in the plain. The steep upper part of the glacier however disconnects from the part in the plain already around 2030–2040 CE........119

List of tables

Table 1: Overview of imagery used for mapping. All images and data are provided by swisstopo (2023a)........10

Table 2: Model parameter variables and values........17

Table 3: Overview of transient proxy-temperature-based modeling experiments. The respective periods and temperature sources are explained in the following chapters (2.3.5; 2.3.6). For better reading flow in the chapters, experiments are not referenced by the names listed here, but rather by the covered period and the forcing used........22

Table 4: Overview of temperature files used for the period from 1500–2020........23

Table 5: Overview of temperature files used for the period from 9 ka onwards........25

Table 6: Averages of comparison period for temperature reconstructions used as forcing........27

Table 7: The CH2018 simulations with respective scenario and the calculated difference from the MeteoSwiss data, which was then subtracted as offset to account for the lower elevation of Disentis compared to the glacier. REMO1 and REMO2 are based on the same model but have different initial conditions (CH2018, 2018)........29

Table 8: The ^{14}C ages of the two sampling sites (see Figure 3 for locations). A second sample taken from the LIA moraine could not be age dated due to insufficient organic content........39

Table 9: ELA values based on two theoretical methods and numerical modeling, for three glacier extents. Note that the numerical modeling ELAs are based on steady state extents......40

Table 10: Response times, i.e., *e* folding times, calculated from lowering ELA step change experiments. Due to modeling resolution, response times are given as 10-year maximum and minimum values. Step change increments are 50 m, as volume changes of smaller increments are not discernible enough........45

Table 11: Response times calculated from steady state geometries with the approach developed by Jóhannesson et al. (1989). Note how the formula is not applicable for decimal ablation values (2730 m a.s.l ELA), as this leads to irrationally high values. Ice thickness values are maximum values along the flow line........45

Table 12: Response times calculated from steady state geometries with the extended formula by Harrison et al. (2003), given for maximal and average ice thickness values along the flow line. Note how the formula is not applicable for decimal ablation values (2730 m a.s.l ELA), as this leads to irrationally high values........46

Table 13: Short summary of parameter combinations and the reasons why they were not used for further modeling. For details see Figures 45-49 in the appendix..51

List of abbreviations

Glaciers are listed with their names in the corresponding local language. “Glacier” is not added after the name, e.g., Brunnifirn instead of Brunnifirn glacier or Brunni glacier. The same principle goes for mountains or valleys.

AAR	Accumulation Area Ratio
BCE	Before Common Era
BP	Before Present, where Present = 1950 CE
cal	Calibrated radiocarbon age
CE	Common Era
ELA	Equilibrium Line Altitude
GLAMOS	Glacier Monitoring in Switzerland
ka	thousand years
LIA	Little Ice Age
m a.s.l.	Meters Above Sea Level
SIA	Shallow Ice Approximation

1 Introduction

1.1 Motivation

Fluctuations of glaciers in the Alps throughout the Holocene have not been uniform, with glaciers forming different stadial stages (e.g., Boxleitner et al. 2019). Studies focusing on overviews of alpine glacier fluctuations throughout the Holocene are numerous (e.g., Holzhauser 2010; Solomina et al. 2015) but mainly rely on static reconstructions of maximal extents. Reconstructions of minimal extents are less common. Traditional ELA reconstructions which depend on the assumption of steady climate are often the basis of reconstructions of past glacial extents. However, today's glaciers lag behind in adjustments to climate, and should hence not be directly compared to past extents. Time-transient reconstructions which consider the dynamics and delay of the response of glaciers to climatic fluctuations provide detailed insight into past glacier behavior. Knowledge about past retreats can also increase the quality of predictions for future glacier response and resulting effects. The currently observed retreat primarily caused by anthropogenic activity (CH2018, 2018; IPCC, 2013), will likely continue (e.g., Zekollari et al., 2019; Zumbühl et al., 2021). Besides implications for the landscape, the retreat of glaciers will also impact water regimes and alpine hazards (Eis et al., 2021).

Since the Little Ice Age (LIA), glaciers in the Alps have retreated. This retreat has increased during the last decades (e.g., Nussbaumer et al., 2011; Vincent, 2002), and is also observable at Brunnifirn (UR). Above this valley glacier in the central Swiss Alps, an archeological rock crystal extraction site was discovered in the autumn of 2013. The receding glacier ice released organic objects which could be radiocarbon dated to 7.95–7.75 ka cal BP (Reitmaier et al., 2016). Such preserved archeological finds serve as reference points for minimal ice extents in glacial reconstructions, as for example achieved at Schnidejoch, where archeological artifacts from different periods could be linked to the local glacier extents (Grosjean et al. 2007). Finds melting out from glacial ice may lead to the assumption of past climate being similar to today. However, such comparisons neglect the concept of response time, which highlights that the response of glaciers lags behind the climate of today.

The lack of glacial reconstructions that consider minimal extents, encompass glacier dynamics, and go beyond assumptions of steady state conditions (i.e., static reconstructions) inspired the continuous dynamic reconstruction of Brunnifirn in this thesis. The delay of glacial response to climate signals is hence incorporated. The archeological finds increase interest in a reconstruction of a possible minimal extent of Brunnifirn during the period when the artifacts were deposited. To achieve this, two approaches are combined: geomorphological mapping of landforms to infer past glacier extents, and numerical ice-flow modeling to analyze fluctuations which cannot be constrained by geomorphological features.

1.2 Aims and research questions

The aim of this thesis is to reconstruct fluctuation of Brunnifirn by combining geomorphological mapping with numerical modeling. Mapped geomorphological evidence serves as indicator of possible past glacier extents and constrains modeled fluctuations. The applied numerical model incorporates the physical behavior and delayed response of the glacier. This produces a continuous and fully dynamic reconstruction of glacier response to variable climate. Thus, the following research questions are addressed. The combined approach suggests two categories: geomorphological mapping and numerical modeling. Questions 2a) and 2c) link the results of mapping and numerical modeling.

1.2.1 Geomorphological mapping

1a) What landforms can be found in the forefield of Brunnifirn?

Alike in other forefields of glaciers in the Swiss Alps, there is an abundance of geomorphological forms in the steep valley named Brunnital, above which Brunnifirn lies. These landforms are mapped with a focus on those relevant to understand the glacial record, rather than producing a complete geomorphological map of the valley. Moraines therefore have the most relevance.

1b) What glacier extents can be identified based on the mapped landforms?

Geomorphological landforms, and especially moraines, allow for reconstructions of past glacier extents (Mackintosh et al., 2017). The mapped moraines and other landforms are therefore used to constrain different ice extents. To temporally confine glacier stages, samples were taken from a moraine and a peat bog for radiocarbon dating. The mapped moraines are also compared with the historical Siegfried map.

1c) What ELAs can be inferred from the reconstructed extents?

As an approximation of understanding the climate required for the glacier to reach the stages identified with mapping, theoretical ELA values are calculated using two methods: the Accumulation Area Ration (AAR, as described by Mackintosh, Anderson, and Pierrehumbert 2017) and the mean elevation (as described by Leonard and Fountain 2003).

1.2.2 Numerical modeling

A time-dependent 2-D ice-flow model as applied by Brown et al. (2013) and Evans et al. (2012) forced by temperature-derived ELA histories is employed to reconstruct the evolution of Brunnifirn. As this model incorporates the dynamics and delay of the glacier, it allows for a transient history of fluctuations.

2a) What steady states match the mapped extents?

The model is first applied to produce steady state (i.e., adjusted to steady climate) outputs which match the mapped extents. In doing so, an understanding of the climate required for the glacier to reach certain extents is gained.

2b) How does the glacier vary with changing climate?

ELA step-change and sinus experiments are conducted to observe the glacier's reaction to transient climate.

2c) How did glacier extents fluctuate given the Holocene climate variations and how do fluctuations compare to the geomorphological constraints?

By forcing the model with different temperature-derived ELA histories, fluctuations throughout the Holocene can be assessed. The reviewed period spans from 9 ka in the Early Holocene onwards until today, with a focus on 7.95–7.75 ka (ages of dated archeological finds), and on 1500–2020 CE. Additionally, the future evolution is explored by modeling a steady state to today's climate and by forcing the model with climate projections until 2099 CE.

2d) What did the glacier look like when the archeological site was accessed?

The ice extents produced with different ELA forcings for 7.95–7.75 ka are compared and evaluated.

1.3 Study area

Brunnifirn is a small glacier located above Brunnital, a remote valley in Kanton Uri in Central Switzerland. The glacier ranges from ca 2560–3250 m a.s.l. in elevation and covered an area of 2.19 km^2 in 2016 (GLAMOS, 2022). Its geometry is rather complex, as it flows from the steep east face of Oberalpstock into a large plain (Figure 1). After the plain, a second steep section follows, from which the glacier however has retreated since about 15 years. The bed in the large plain contains significant overdeepenings, as ice thickness measurements showed maximum values of up to 140 m. The steep upper section above the plain however is only about 20–40 m thick (Grab et al., 2021).

At the beginning of the valley, there are numerous boulders which were selected for 10Be exposure dating (Figure 1). From the large moraine complex also mapped on the official topographic map (swisstopo, 2023a), soil samples were taken for radiocarbon age dating. A peat bog further down valley than the large moraine complex was also sampled for radiocarbon dating. Up valley from the large moraine complex there is an abundance of freshly deposited moraines, i.e., without or with little vegetation cover and not weathered. The archeological site is located at the southwestern mountain pass, Fuorcla da Strem Sut. The finds were discovered in a cave just above the ice surface level (see Figure 1).

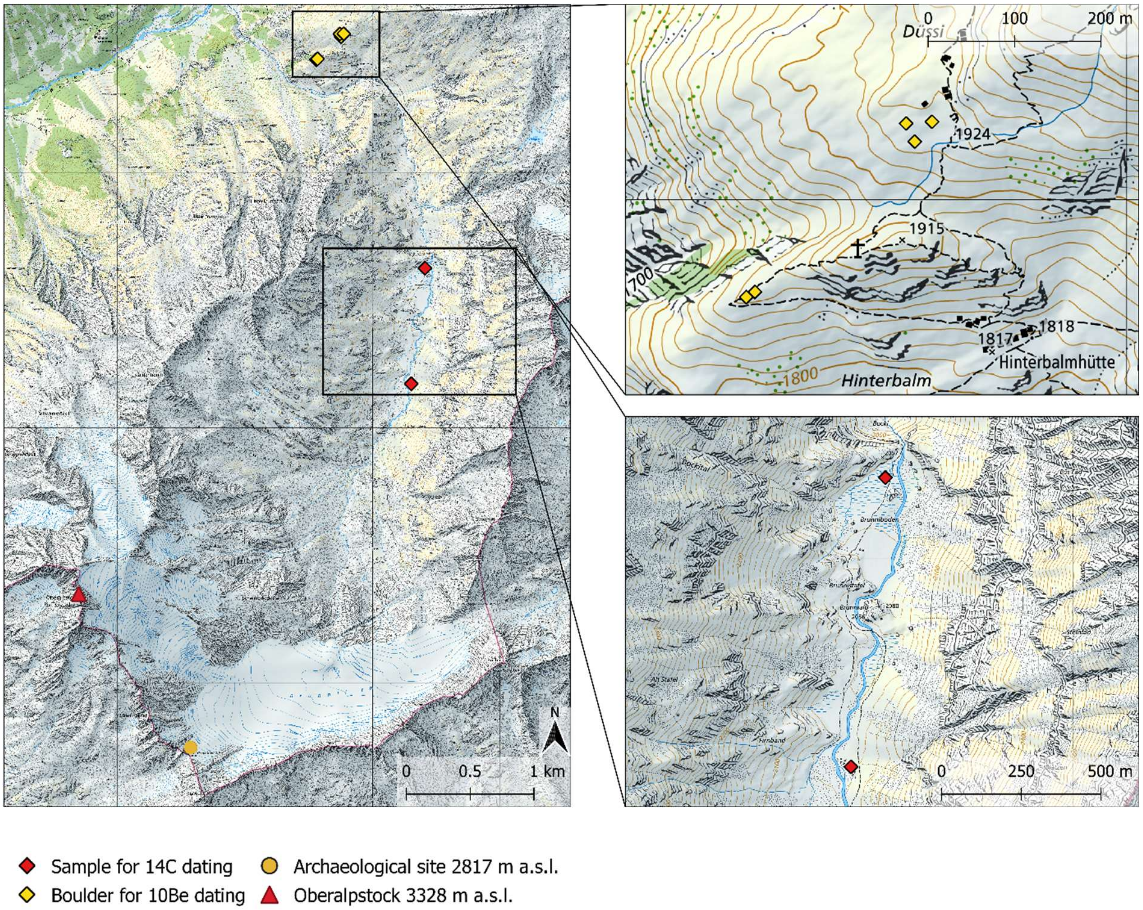

Figure 1: *Map of Brunnital with sample locations and archeological site. The 10Be ages of the sampled boulders will be processed after submission of this thesis. Background map: swisstopo (2023).*

1.4 Background

1.4.1 Overview of Holocene glacier fluctuations

In global summary, glaciers in the northern hemisphere followed a trend of growth from the mid to late Holocene, whereas glaciers in the southern hemisphere were decreasing from the early Holocene until today, both probably caused by orbital forcing. However, fluctuations cannot be matched to just one influencing mechanism, global changes are more complex (Solomina et al., 2015). On a more local scale like the Alps, trends of fluctuations are clearer and lead to studies and compilations with distinct overviews like the one by Holzhauser (2010, see Figure 2). Other studies highlight the influence of higher summer temperatures from ca 10 ka onwards (e.g., Wanner et al. 2008). These conditions caused glaciers in the Alps to not advance strongly between about 10.5–3.3 ka, except for small glaciers which might have reacted strongly to short-term cold climatic signals. After 3.3 ka, glaciers in the Alps might have followed a trend of growth, reaching maxima in the Little Ice Age (LIA; Ivy-Ochs et al., 2009).

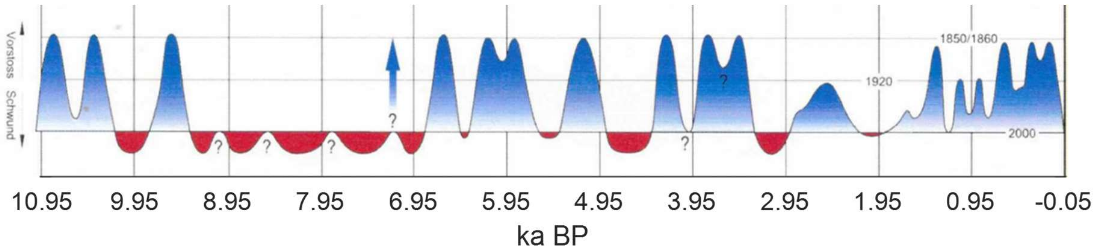

Figure 2: *Overview of glacier fluctuations throughout the Holocene in the Swiss and Western Alps, modified excerpt from Holzhauser (2010). Blue fluctuations stand for advances over the extent of glaciers in the year 2000 CE, retreats behind that level are marked in red. Question marks and the arrow stand for unknown duration or extent of fluctuations.*

Nevertheless, the extent and timing of fluctuations can be contradictory. An example are reactions to the abrupt cooling event around 8.2 ka (Alley and Ágústsdóttir, 2005). Some studies have found clear advances of glaciers (e.g., Nicolussi and Schlüchter 2012), whereas others only find small to no changes (e.g., Holzhauser 2010). A reason for such contradictions is that later advances have probably destroyed most traces of fluctuations (Kronig et al., 2018; Schimmelpfennig et al., 2014), making it difficult to assess earlier maximal extents. Another example for a disagreement are the archeological finds from Schnidejoch, which indicate permanent ice cover from 5 ka until their recent discovery (Grosjean et al., 2007). This is disputed by retreats of glaciers smaller than their 2000 CE size found for other regions of the Alps (Holzhauser, 2010). Such conflicting results highlight the importance of local reactions of glaciers to climate signals.

When comparing past glacier fluctuations to current extents and the ongoing rapid retreat witnessed almost everywhere in the world, it is crucial to highlight that the ongoing change is unprecedented throughout the Holocene (Solomina et al., 2015). In spite of orbital forcing conditions suggesting glacial growth (Solomina et al., 2015), the general global trend is one of rapid retreat, which is likely mainly caused by anthropogenic greenhouse gas emissions (CH2018, 2018; IPCC, 2013). When relating small glaciers in the past to today's sizes, the concept of response time must not be neglected. Glaciers are not in balance with current climate and their response lags behind by decades, depending on glacier geometry (Mackintosh et al., 2017).

1.4.2 Archeological context

The discovery of the glacially conserved archeological site, a vein near the mountain pass Fuorcla da Strem Sut above Brunnifirn, exposed the oldest site of this kind in the Alps (Reitmaier et al., 2016). Remains of antlers and fragments of woods could be radiocarbon dated to 7.95–7.75 ka cal BP, and were probably covered by the ice throughout most of the time until the discovery in 2013 (Cornelissen et al., 2022). The site was likely used for rock crystal extraction, which is why organic materials were transported to such high altitude (Reitmaier et al., 2016).

Archeological finds provide insight into past glacier fluctuations (e.g., Grosjean et al. 2007; Bonani et al. 1994). Just like fossil woods and peat bogs (e.g., Holzhauser 2010; Nicolussi et al. 2014; Wipf 2001), they require quasi-permanent ice-cover to be preserved. When organic material in finds can be radiocarbon dated, the derived ages suggest that the glacier could not retreat beneath the extent it had during time of deposition, as the organic material would otherwise decay. Nevertheless, fluctuations of glaciers are not always uniform to climate and random reactions to small-scale mass balance variations occur (Mackintosh et al., 2017). Artifacts have much higher chances of preservation if they remain within depressions where they do not melt out during warm summers (Pilø et al., 2023). Therefore, they should not be viewed as a direct proxy of local glacier extent, as the glacier may have retreated more than the ice at the location of the preserved artifacts. They roughly indicate permanent ice cover, but the fluctuations of glaciers may differ.

Finally, the concept of response time plays a crucial role when comparing today's glacier extent to a supposed extent during the deposition of the archeological finds. Even if the glacier once had an extent similar as what we observe today, the two extents cannot be compared, due to glaciers currently being far from a steady state and retreat rates likely being unprecedented throughout the Holocene (Bohleber et al., 2020).

1.4.3 Geomorphological mapping

Moraines can help to infer past glacier extents: if not overridden during a readvance of a glacier, they can remain in the landscape and mark the last maximum extent of a glacier (Benn and Evans, 2010). Knowing past maximal ice extents allows for reconstructions of the corresponding climate thanks to knowledge about how glacier fluctuations and climatic change are linked. Such reconstructions can be done with simple methods like the AAR or mean elevation, which allow for accurate estimations of paleoclimate. If these methods are applied thoroughly, they provide climate reconstructions similar to numerical modeling results (Mackintosh et al., 2017).

Hence, moraines must be mapped with high precision. This can be achieved by mapping with high-resolution aerial imagery mapping based on remote sensing data (or remote mapping) (Chandler et al., 2018). For studies in Switzerland the freely downloadable high-quality data from swisstopo greatly improves the potential of remote mapping. Field mapping is required when image resolution, surface topography color, or shadows complicate mapping. Thus, a holistic procedure is combining both approaches and thereby enhancing accuracy of geomorphological mapping (Chandler et al., 2018).

Moraines were the focus of the mapping process but other landforms which influence moraines or improve understanding of the glacial history were mapped as well.

1.4.4 Numerical modeling

Reconstructions of past glacier extents can also be achieved with numerical modeling. Using advanced flow models, fluctuations can be reproduced with respect of the physics of glaciers, bed topography, or exposition. Also, sensitivity assessments further improve the understanding of how glaciers react to shifts in climate (Mackintosh et al., 2017). For this study, past glacier extents were reconstructed with a time-dependent 2D ice-flow model (Brown et al., 2013; Evans et al., 2012). The model is forced simply by an ELA history derived from different paleoclimate reconstructions (Affolter et al., 2019b; Alley, 2004; Casty et al., 2005a; MeteoSwiss, 2023).

The implication of a numerical model allows for a perspective on paleo-ice extents which cannot be achieved by moraine-based reconstructions: fluctuations which did not allow for the deposition of moraines can be reproduced as well. Past glacier extents can be reconstructed for dynamic instead of static climate. The ELA forcing produces a continuous evolution of fluctuations for the period with available climate data. Naturally, the temperature-derived forcing controls fluctuations, making them dependent on the quality of the climate reconstructions. But by comparing modeling outputs with the results from geomorphological mapping, the accuracy of the temperature reconstructions can be assessed (Mackintosh et al., 2017).

2 Methods

2.1 Mapping

Geomorphological mapping serves to understand the formation of landforms and may also give information about the age of those landforms (Hubbard and Glasser, 2005). Mapping the Brunnital therefore came as an accessible and valuable tool to understand paleoglacial extents of Brunnifirn for the LIA and possible older extents. This approach allows for better interpretation of modeling results and providing constraints for the model configuration. The mapped landforms also allowed for paleo-ELA reconstructions (Accumulation Area Ratio; AAR), as described by Mackintosh et al. (2017) and mean elevation, as described by Leonard and Fountain (2003) and Porter (1975). Both were compared to ELA values based on numerical modeling.

The mapping was focused on specific aspects of the valley: moraines, moraine ridges, rock glaciers, trimlines (vegetation changes and surface characteristics), striations in bedrock, rockfall cones, debris flow fans and channels, and streams. Involving geomorphologically active landforms (debris flow channels and streams) helps understanding the chronology of the valley. Moraines and striations in bedrock were also mapped at the Düssi slope (Figure 3). The product therefore is a themed geomorphological map as described by Hubbard and Glasser (2005), focused on forms relevant for the glacial reconstruction, and not on the general geomorphology.

The focus of the mapping are the moraines. These can be compared with ice-flow modeling outputs and are helpful to estimate the size of paleoglaciers, as they show past maximum extents (Chandler et al., 2018). Terminal moraines are the most helpful here, as their position can be directly related to the glacier length in model outputs. Moreover, lateral moraines allow for comparison with model outputs, as they are marginal constraints of past ice extents. A second type of moraines the field mapping sheds light on are hummocky moraines. Due to unknown formation of the moraines, the term is used descriptively for terrain of moraine material with small irregular hills. Hypothetically, the moraine material may have been deposited at the terminus of a receding or stagnant glacier tongue that slowly melted, leaving behind hummocky moraines (as described by Benn and Evans, 2010; Hubbard and Glasser, 2005).

Combining mapping approaches leads to more coherent results, avoidance of image resolution issues of aerial imagery, and easier interpretation of landforms (Chandler et al., 2018). Mapping was therefore conducted both in the field and remotely, to then link and reevaluate the results of the two methods. A combination of field and remote mapping with the aid of aerial imagery and DEMs (imagery from swisstopo, 2023) and existing maps from the swisstopo geocover resource (swisstopo, 2023a) were used. The identification of landforms and geomorphological features was following the classification of other mapping studies (e.g., Brown et al., 2013; further examples in Chandler et al., 2018) and the general literature (Benn and Evans, 2010;

Hubbard and Glasser, 2005). The landforms relevant for tracking former glacier extents were chosen during a first field campaign. Moraines were categorized based on their freshness and appearance and hence divided into the following sub-categories: *well-preserved*, *remnant*, and *supposed*. The categories are similar to the description of Heyman et al. (2008).

- **Well-preserved moraine:** clearly visible accumulation of unsorted, partly rounded, unlayered glacially deposited material. Elongated or round hill-like features, ca 10–100 m in length. Freshly deposited, i.e., no or sparse vegetation cover.
- **Moraine remnant:** form like well-preserved moraine, but strong change of original appearance by weathering and erosion. Covered by vegetation or rock fall debris.
- **Supposed moraine:** accumulation of sediment, but form cannot be clearly identified in the landscape. Surroundings (e.g., trimlines) indicate possible presence of moraine.

Iterative mapping process

First mapping was conducted remotely with aerial images, shaded reliefs, and the geocover layer (swisstopo, 2023b). Field mapping with topographic maps and aerial images was conducted on two field campaigns. The knowledge gained from the field mapping was used to improve the remote mapping. During the field campaigns, ground truthing of the remote mapping was conducted.

Table 1: *Overview of imagery used for mapping. All images and data are provided by swisstopo (2023a).*

Imagery resource	Resolution	Application
Topographic map	1:10,000 scale	Base layer for field mapping, geomorphological landforms
Aerial image 2018/2019	0.25 m	Geomorphological landforms
swissALTI3D mono- and multidirectional shaded relief	0.25 m	Geomorphological landforms, mostly moraines
Geocover (geological vector data set)	none (vector)	Geomorphological landforms
Old aerial images: 1946, 1958, 1979, 1990	Varying for each image. Irrelevant, as large-scale information was used.	Glacier extents

2.1.1 Field Mapping

Mapping was carried out by hand on printed topographic base maps (scale: 1:10,000), on printed aerial images, and on shaded reliefs (overview in Table 1). The geological vector dataset layer available on *map.geo.admin.ch* was also consulted. The hand drawn maps were afterwards digitalized in QGIS.

After consulting the mapping from the existing geocover (swisstopo, 2023b) and the aerial image and shaded relief (swisstopo, 2023b), a first field scouting day was performed to get an overview of the study area and the related geomorphological features. Moraines and boulders at the Düssi slope, at the beginning of Brunnital, were marked for further analysis. The area around the moraine complex, which was supposedly assigned to the LIA maximum according to historical maps (Dufourkarte; Siegfriedkarte, accessed through swisstopo, 2023a), was traversed and moraines were mapped roughly. This preparation allowed for a second long campaign, during which the lower and especially upper part of the valley were mapped, and marked areas were further analyzed. A longer campaign allowed for closely inspecting moraines away from the hiking trail, and especially presented the landforms during different daylight situations, which allows more precise mapping due to longer shadows of landforms (Chandler et al., 2018). The goal therefore was to map moraines and other landforms in reasonable distance of the main hiking trail, and not moraines or rock glaciers on steep and remote slopes. A last field campaign allowed on focusing on an upper section of the valley, where ground truthing was essential due to a complex accumulation of hummocky moraines.

2.1.2 Digital Remote Mapping

The area of interest was inspected remotely prior to the first field campaign as preparation. After the first field campaign, the mapped areas were refined remotely, to then have the possibility of validation and reassessment on the subsequent field campaigns. The last field campaign focused on the hummocky moraines, the respective areas were again further refined, using remote imagery. After conclusion of the field campaign, the areas that were not part of the field mapping were mapped remotely. This includes the rock glaciers and moraines in Val Strem, Val Cavardiras, on the northwestern slopes of Oberalpstock, and around Tschingelfirn. Past glacier extents were also mapped with aerial images from swisstopo for the years 1946, 1958, 1979, 1990.

The imagery used for the process was already georeferenced and not processed further (overview in Table 1). Firstly, aerial images, or orthophotographs were used. These proved to be especially helpful for the mapping of hummocky moraine complexes, as mapping these chaotic structures in the field would have taken too much time. Due to simplicity of switching between images, overlaying, and especially simple vectorization of the landforms, QGIS was used for digital mapping. Further, Digital Elevation Models (DEMs) were used. As described in the literature, DEMs are useful to map depositional landforms like moraines, and erosional forms like debris flow channels (Chandler et al., 2018, and references therein). The geological vector dataset layer available on *map.geo.admin.ch* served as an initial impression of the field site, and as validation and comparison of the mapping results. Finally, a historical map (Siegfriedkarte, available online by swisstopo, 2023) were used to find the LIA glacier extents which point towards possible terminal moraine deposition areas.

2.2 Landform Age Dating

Sedimentological investigations with radiocarbon dating provide crucial information to validate the interpretations of field mapping (Chandler et al., 2018). Radiocarbon ages to landforms also allows for a better understanding of the evolution of the landscape and puts modeling outputs into scale. Samples for age dating were collected from the LIA moraine and from a peat bog located ca 900 m down valley. Also, boulders from the Düssi slope and Hinterbalm hill were sampled.

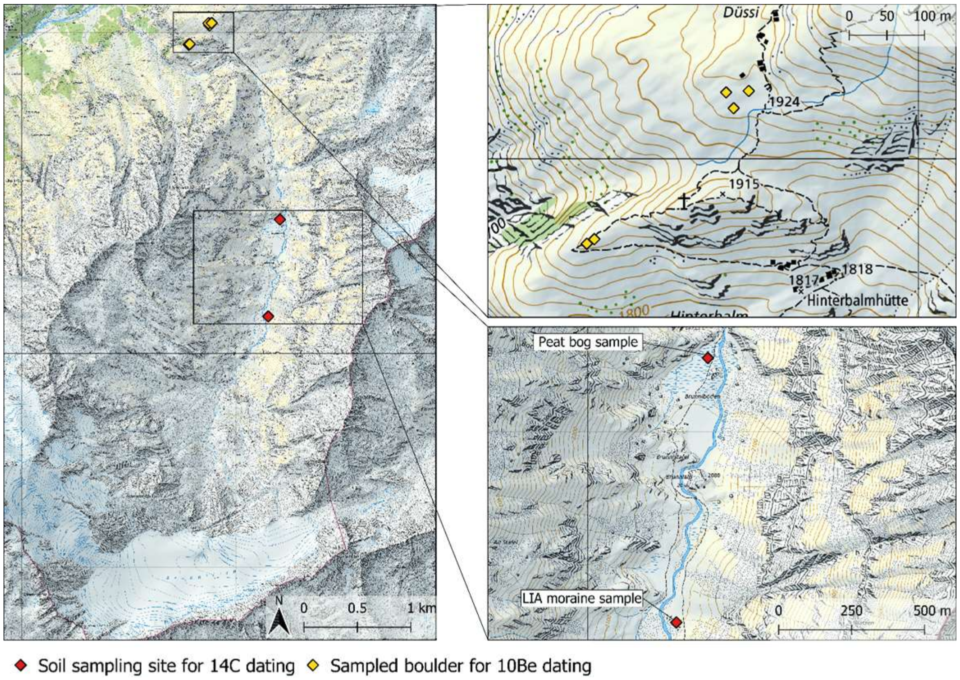

Figure 3: *Map of Brunnital with sample locations. The 10Be ages of the sampled boulders will be processed after submission of this thesis. Background map:* swisstopo (2023)*.*

2.2.1 Moraine soil and peat bog samples for radiocarbon dating

Two samples of soil were collected from the main ring of the LIA moraine for radiocarbon dating. The goal of these samples was to constrain the age, respectively the deposition time, of the moraine. However, due to a lack of organic material, only one of the samples could be dated. The dated sample was taken from the outer ridge of the prominent LIA moraine (Figure 4).

A peat bog further down valley from the LIA was sampled as well (Figure 5). The goal here was to find the age of the peat bog, as this would serve as proxy for past glacier length: within the period of existence of the peat bog, the glacier could not have reached that location, as an advance further down valley would have destroyed the peat bog. Luckily, a small stream had cut a channel into the peat bog, exposing a profile of the peat bog, which made sampling quite easy. As the exposed profile is visible from the main hiking path, we chose not to dig much further into the profile to not disrupt the landscape. There are layers below the sampled layer, which needs to be considered in the age analysis.

Thanks to the deposition of cosmogenic ^{14}C in organic matter, the age of the organism's death and the onset of radioactive decay can be calculated. The measured age of samples is influenced by changes in atmospheric ^{14}C content, so radiocarbon ages need to be calibrated, which provides calendar ages in BP. As the calibration process is a probabilistic procedure, ages are associated with a probability distribution represented by a 68% (1 sigma error) and a 95% (2 sigma error) confidence interval (Hajdas, 2008). The calendar ages were obtained using the OxCal 4.4 calibration program (Bronk Ramsey, 2009, 2001; Reimer et al., 2020) by applying the IntCal 20 calibration curve. Calibrated ages are given in the 1 sigma and 2 sigma range (minimum and maximum value for each).

The peat sample was cleaned by an acid-alkali-acid (AAA) treatment. To know the start of soil formation and thus the deposition of the moraine site, the oldest organic matter that was attached to mineral surfaces needs to be dated. This carbon fraction was obtained by using a chemical treatment with H2O2 (for details see: Calitri et al., 2021, 2019; Favilli et al., 2009a, 2009b; Zollinger et al., 2013). The treated material was combusted at 900 °C to produce CO2 which was then reduced to graphite. After reduction, the mixture is pressed into a target and carbon ratios are measured by Accelerator Mass Spectrometry (AMS) using 0.2 MV radiocarbon dating facility (MICADAS) of the Ion Beam Physics at the Swiss Federal Institute of Technology Zurich (ETHZ).

Figure 4: *A) Image of the LIA moraine with two distinguishable ridges. The arrow indicates direction of (paleo-) ice flow. The sample for radiocarbon dating was taken in the outer ridge, so further downstream. B) Stable Surface that allowed for development of a soil in which the profile was dug. C) Close-up of soil profile. Photos: Jonathan Davidson in 2022.*

Figure 5: *A) Peat bog as viewed from below, the image is taken valley upwards. B) Profile of the peat bog. The sample for radiocarbon dating was taken from the lowest part of the hole. Photos: Jonathan Davidson in 2022.*

Boulder samples for beryllium-10 age dating

Five samples from boulder deposited on the ridge of Hinterbalm hill will be age dated using the ^{10}Be method. These results will constrain the period when the glacier had an extent immense enough to deposit these boulders on the ridge.

2.3 Flow modeling approach

A time-dependent 2-D ice-flow model as applied by Brown et al. (2013) and Evans et al. (2012) is used to investigate the evolution of glacier geometry in relation to climate variations.

2.3.1 Model Setup

The MATLAB-based model was provided by Andreas Vieli. Minor adjustments were made to make it suitable for the case of the Brunnifirn area. The ice flow is calculated based on a Shallow Ice Approximation (SIA; Hutter, 1983), with local ice flow calculated in respect of the local ice thickness, ice surface slope, and a given ice softness parameter *A*. Basal sliding is ignored but indirectly included by enhancing the ice softness A (see below). The climate forcing is approximated by an ELA-history which is related to summer temperatures (sections 2.3.5; 2.3.6), and an elevation dependent surface mass balance function is applied (see below). Precipitation, evaporation, sublimation, and wind redistribution are not explicitly included in the model.

The goal of this model is not to recreate every aspect of real ice flow, but rather to quantify glacier extent and volume for a certain climate. Nevertheless, the model output produces useful representations of (paleo-) glacier extents (e.g., Figure 6). Including ice geometry (thickness and surface slope), ice softness, bed geometry, flow velocity, and the mass balance ratio allows for reliable glacier extent modeling. The most relevant model parameters are listed in *Table 2* and described when necessary.

Table 2: *Model parameter variables and values.*

Parameter	Description	Value	Units
ELA0	Reference ELA for climatic changes	varying	m a.s.l.
dt	Modeling time interval	0.05, 0.1, 0.5	a
dx	Grid resolution	50	m
γ_{abl}	Mass balance gradient in ablation area	0.007	a^{-1}
γ_{acc}	Mass balance gradient in accumulation area	0.004375	
$\gamma_{abl}/\gamma_{acc}$	Mass balance gradient ratio, i.e., ablation-accumulation gradient ratio	1.6	–
A	Ice softness	1.42×10^{-16}	$Pa^{-3}\ a^{-1}$

- The elevation-dependent mass balance is approximated in the model by two separate gradients above and below the ELA (i.e., accumulation and ablation area), resulting in a ratio of 1.6 which corresponds to an AAR of 2:1. Using just one gradient would result in too high accumulation rates and hence overestimate the transfer of mass. This is based on the non-linearity of mass balance gradients, as for valley glaciers they are usually flatter in the accumulation area than in the ablation area. Reasons for flatter accumulation area mass balance gradients are altitudinal changes in solar radiation, heat transfer, evaporation and sublimation, shielding by rock walls, and snow redistribution by wind (Benn and Evans, 2010).

- The calculation of the surface mass balance includes a solar radiation correction, which adjusts the ELA depending on the annual potential radiation for the slope and aspect given the surface topography (based on the DEM) and at the given latitude (48.2° for Brunnifirn). This leads to a lowering of the ELA of a 150 m for north-facing slopes compared to south-facing slopes.
- Ice properties (expressed by ice softness *A*) were not changed for the experiments and are based on values from Paterson and Budd (1982), corresponding to temperate ice (Cuffey and Paterson, 2010), which fits for this case due the elevation of the glacier and the presence of melt in the accumulation area. As this still often leads to model outputs in which the ice is too stiff, the softness is then multiplied by an enhancement factor of 3.0, indirectly also taking basal sliding into account.
- Ice flux is calculated from Glen's flow law given by

$$Q_i = \bar{u}_i H = \frac{2A}{n+2} \tau_i H^2 \qquad i = x, y \tag{2.1}$$

with

$$\tau_i = \rho g H \frac{\partial z_s}{\partial_i} \tag{2.2}$$

which gives

$$Q = \frac{2A}{n+2} \left(\rho g \frac{\partial z_s}{\partial x} \right)^n H^{n+2} \tag{2.3}$$

where the ice flux Q is given by the vertically averaged ice flow ū multiplied by the ice thickness H, with Glen's *A* and exponent = 3. τ represents the gravitational driving and basal shear stress, which is defined by the density ρ multiplied by gravitational force g along the surface slope $\frac{\partial z_s}{\partial_i}$ at height *H*.

- Bed geometry is given by the digital elevation model swissALTI3D by swisstopo (2023) and the ice thickness analysis with ground-penetrating radar by Grab et al. (2021).
- Slopes steeper than 45° do not receive accumulation.
- The grid size of 50 m was kept constant throughout the experiments, as the SIA-assumption does not justify a further refinement. The glacier extent can only be resolved to the 50 m spatial scale. The related uncertainties in extent are however considered to be minor in comparison to other uncertainty aspects like temperature-ELA conversion

factor or temperature data offset due to proxies from other regions which will be discussed in chapter 4.3.

- The model saves several parameters as outputs, including glacier length (along a defined flow line), volume, area, ELA, and effective mass balance at the tongue, which can be used for glacier evolution plots or theoretical calculations like response time estimates.

To run the model, the starting and ending time, as well as the modeling and output time intervals must be selected. The ELA0 needs to be set, which serves as constant ELA for a steady state run, or during a time dependent steady state run as a baseline, from which the change in ELA is added or subtracted. An experiment can be initiated without ice, or with a prescribed existing glacier surface geometry. Finally, three types of ELA-forcing experiments were undertaken: (i) for a *static* mass balance forcing (steady state), the ELA remains constant throughout the run; (ii) for a sinus forcing experiment, the ELA changes as a sinus wave with given period (time) and amplitude (extent of change of ELA); and (iii) for a *time*-transient experiment, the input of ELA difference is calculated into the ELA0 at each point in modeling time.

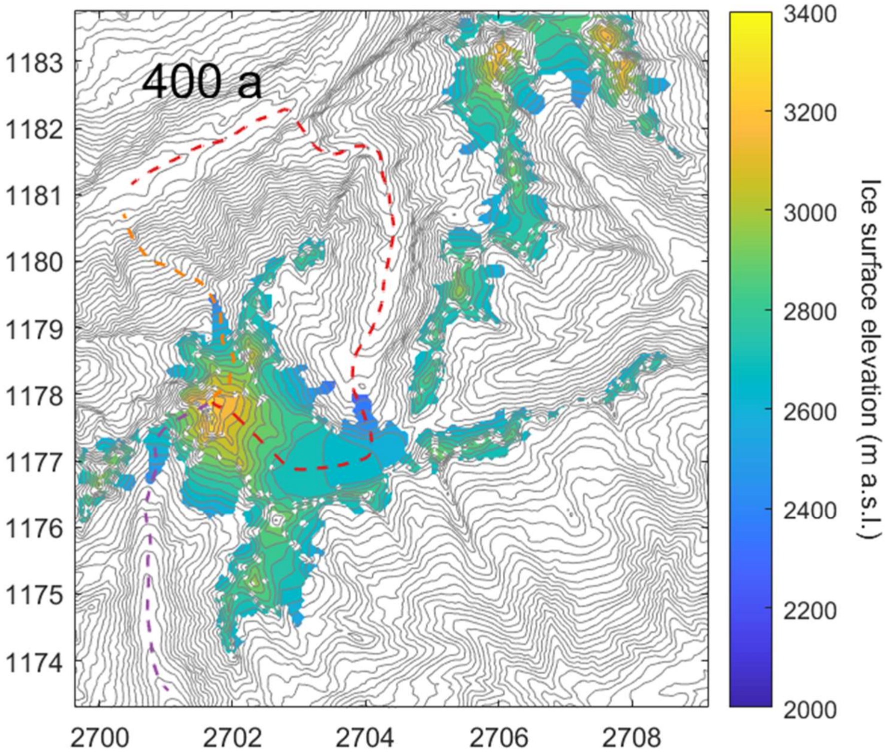

Figure 6: *Exemplary model output for a steady state ELA of 2700 m a.s.l. The map shows the ice surface elevation on the surface topography. The number in the upper left corner shows the run time (400 years). The colored lines are the flow lines of Brunnifirn (red), Staldenfirn (orange), and Glatscher da Strem (purple). The axis labels are rounded coordinates of the CH1903+/LV95 grid, one unit equals to 1 km.*

2.3.2 Steady state and step change modeling

The first runs with the model consisted of steady state modeling, with no ice as initial state. After finding the parameters to produce outputs which correspond to defined extents (2019 CE extent, possible LIA extent), the ELA was lowered by constant increments of 50 m (25 m or smaller for extents of high to minor ELA changes). This produced series of steady state extents, from a tiny glacier with an ELA just below the peak of Oberalpstock, to a large glacier, reaching Maderanertal. These steady states could be compared to theoretical ELA calculation methods like the AAR or the mean elevation. The ice buildup was continued until steady state was reached, meaning no more change in glacier geometry for at least 50 years (or even for more in cases of large glacier extents, as minor size changes can occur over large time intervals). With the step change experiments, the procedure was the same as with the steady state experiments, but the end geometry of the last experiment (steady state with higher ELA) was used as starting glacier surface geometry. After producing steady state conditions, the change in volume was used to calculate estimations of response times (*e* folding times, as done by Leysinger Vieli and Gudmundsson, 2004), corresponding to the ELA of the steady state experiment.

These response times were compared to results of theoretical response time calculations. Firstly, response times are calculated as $\tau v = H/(-b_t)$, where H is the thickness of the glacier, and b_t is the ablation (Jóhannesson et al., 1989). Secondly, response times are calculated as $\tau v = He/(-b_e) - \gamma eHe$, where He stands for the effective and mean thickness of the glacier, b_e is the effective ablation at the tongue, and γe is the effective mass balance gradient (Harrison et al., 2003).

2.3.3 Sinus experiments

To estimate response times of different glacier extents and to find ELA thresholds at which glacier length changes are most sensitive, a series of sinus experiments were conducted. Time periods of 20, 50, 100, and 200 years were tested, i.e., the ELA sinus period was varied from short to long. The amplitude which defines the change in ELA during a period was kept at 200 m, so the ELA was raised and lowered by 100 m during a full period. Each of these periods was applied to four different ELA0 values which are results of steady state modeling glacier extents: to a small glacier (ELA0 = 2800 m a.s.l.), to the 2019 CE extent in steady state (ELA0 = 2730 m a.s.l.), to an extent where minor changes in ELA lead to strong length variations (ELA0 = 2720 m a.s.l.), and to the possible LIA steady state extent (ELA0 = 2585 m a.s.l.).

2.3.4 Transient experiments

For modeling reconstructions of the Holocene and the Little Ice Age, temperature data was converted into ELA change and used as forcing for the model. The climatic change in the forcing was calculated as change in ELA, given by

$$\Delta ELA = ELA_{\mathrm{fc}}\,(T_{\mathrm{ann}} - T_{\mathrm{avg}}) \tag{2.4}$$

with the average of temperatures T_{avg} from the MeteoSwiss data from 1901–2000 (8.5019 °C; MeteoSwiss, 2023) subtracted from the yearly temperature T_{ann} (with varying data source, depending on the respective time period that is modeled) and then multiplied with a sensitivity factor $ELA_{\mathrm{fc}} = 130$. The temperatures for T_{avg} were taken over the entire 20th century to best ignore small variations in temperatures. The ΔELA is then added to the set value of ELA0 for the respective transient experiment, which leads to a variation in ELA, therefore expressing climatic change over time. The model has two ways of interpolating temperature if there is no data for one or several years: using the nearest next or last value or interpolating linearly between values.

Oerlemans and Hoogendoorn (1989) found that 1 °C in temperature change would lead to a 130 m change in ELA for a glacier in the Alps, however more recent studies have applied values of 60–70 m °C^{-1} (Vincent, 2002), 113 m °C^{-1} (Oerlemans, 2010), 97 m °C^{-1} (Thibert et al., 2013), 80–100 m °C^{-1} (Lüthi, 2014), or 50–85 m °C^{-1} (Six and Vincent, 2014). Due to these variations in ELA temperature sensitivity, three different factors (100, 120, and 130) were tested with the numerical model to find the best fitting factor for this model when applying it to Brunnifirn.

Table 3: *Overview of transient proxy-temperature-based modeling experiments. The respective periods and temperature sources are explained in the following chapters (2.3.5; 2.3.6). For better reading flow in the following chapters, experiments are not referenced by the names listed here, but rather by the covered period and the forcing used.*

Name	Time period	Temperature reconstruction/projection used as forcing	Reference ELA (m a.s.l.)	ELA$_{fc}$ (m °C^{-1})
Sensitivity testing	1500–2020 CE	Combined yearly summer temperatures (Casty et al., 2005b; MeteoSwiss, 2023)	2700, 2720, 2730	100, 120, 130
Transient1500_2020	1500–2020 CE	Combined yearly summer temperatures (Casty et al., 2005b; MeteoSwiss, 2023)	2720	130
Transient9ka_2020_mil	9 ka until 2020 CE	9–0.451 ka: Milandre (Affolter et al., 2019b) 1500–2020 CE: Combined yearly summer temperatures	2720	130
Transient9ka_2020_gisp	9 ka until 2020 CE	9–0.451 ka: GISP2 (Alley, 2004) 1500–2020 CE: Combined yearly summer temperatures	2720	130
Future1500_2099	1500–2099 CE	1500–2020 CE: Combined yearly summer temperatures 2021–2099 CE: steady state ELA	2720	130
Future1981_2099	1981–2099 CE	CH2018 future temperature projections (CH2018, 2018)	2720	130

2.3.5 1500–2020 CE

This period is confined by the chosen temperature reconstructions listed in this chapter. It only covers a part of the LIA, from 1500 until its end at ca 1850 (Braumann et al., 2021; definition varies in literature). 2020 CE is the last modeled year.

The most recent large glacier advances occurred during the LIA, a period characterized by glacial advance in many regions of the world. Depending on the regional differences in advances, the beginning of the LIA can be set to around 1350 or 1450 CE, and the end to around 1850 CE, when fast retreats of glaciers followed (Benn and Evans, 2010; Brönnimann et al., 2019). In this thesis, temperature data from the last 500 years serve as forcing to model the fluctuations of Brunnifirn.

The first data set consists of the area-mean temperatures of northern Switzerland for elevation above 1000 m a.s.l. from 1864–2021 CE (MeteoSwiss, 2023: version 1.1.), which were produced by integrating air temperature data from a small number of measuring stations with long-term measurements (Begert and Frei, 2018). Thanks to the specific temperatures for high elevations, these can be applied to the case of Brunnifirn.

This temperature series was combined with a temperature reconstruction for the European Alps from 1500 onwards, with a grid resolution of 0.5° x 0.5° (Casty et al., 2005a). This reconstruction was produced based on early measurement stations, but also applying documentary records like narratives and annals, resulting in seasonal resolution from 1500–1658 CE, and monthly resolution from 1659–2000 CE (Casty et al., 2005b).

Table 4: *Overview of temperature files used for the period from 1500–2020.*

Name	Source	Type	Temporal application
Area-mean temperatures Northern Switzerland >1000 m a.s.l.	MeteoSwiss (2023)	Measured area mean summer temperatures (JJA)	1864–2020
Temperature variability in the European Alps since 1500	Casty et al. (2005a)	Measured and proxy evidence summer temperatures (JJA)	1500–1863 (1500–1658: seasonal resolution; 1659–1863: monthly resolution)

The temperature file to model from 1500–2020 (Figure 7; Table 4) firstly consists of the summer temperatures of the reconstruction from 1500–1863 (Casty et al., 2005a). From 1500–1658, the resolution is seasonal (summer season was used), and from 1659 to 1863 the resolution is monthly, where the summer months (June, July, August) average was used. A cooling offset of 0.9 was applied to the reconstructed temperatures, as the curve shows the same variation as the measured temperatures (MeteoSwiss, 2023), just with an offset. From 1864 to 2021, the averages of the measured summer months (June, July, August) were used.

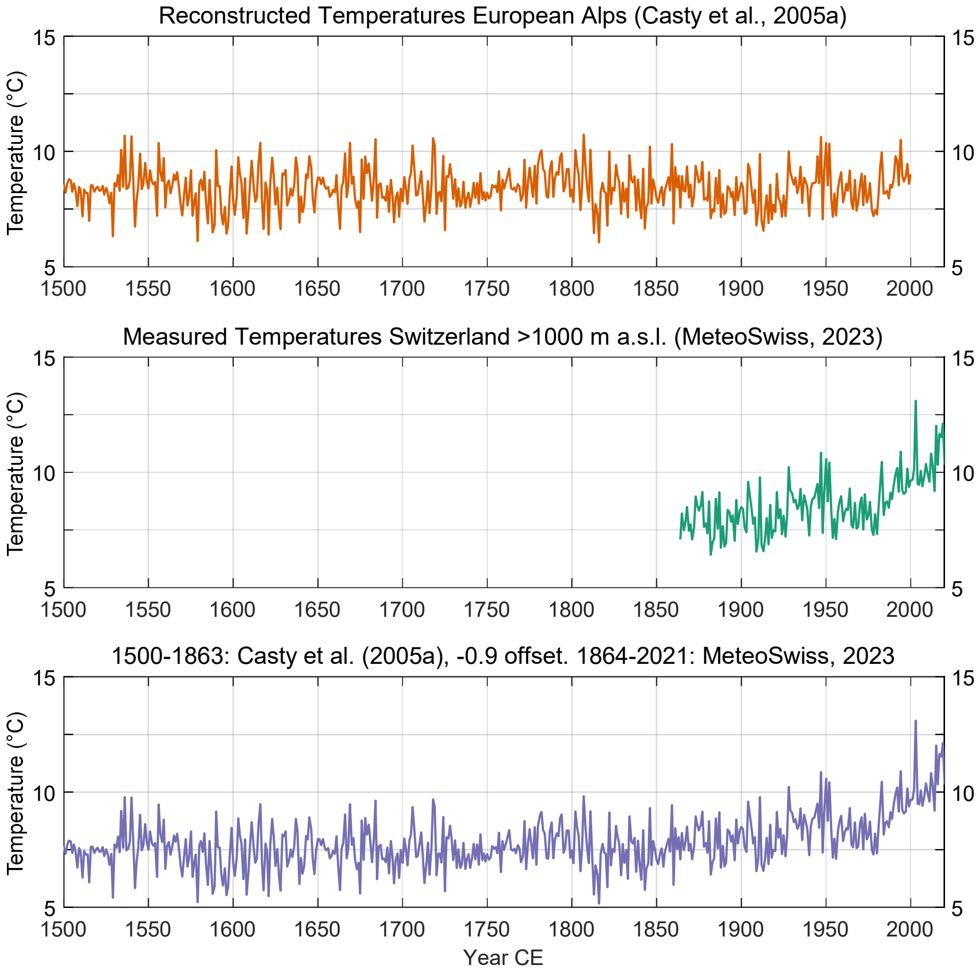

Figure 7: *The reconstructed temperatures from Casty et al. (2005a), the measured and interpolated from above 1000 m a.s.l. temperatures from MeteoSwiss (2023), and the combination of both which was used as forcing for modeling of 1500–2020 CE. Note how the reconstructed temperatures from Casty et al. (2005a) are too warm compared with the MeteoSwiss data from 1864 (beginning of MeteoSwiss data set) to almost 1950, which is why a cooling offset of 0.9 was applied.*

2.3.6 Holocene

Holocene modeling stands for long modeling of long periods from 9 ka BP onwards. For the sake of simplicity, model runs from 9 ka until today are hereafter called Holocene modeling.

Table 5: *Overview of temperature files used for the period from 9 ka onwards.*

Name	Source	Type	Temporal application
GISP2	Alley (2004)	Yearly ice core temperatures	9–0.45 ka
Milandre Cave	Affolter et al, (2019b)	Mean yearly fluid inclusion temperatures	9–0.45 ka

To analyze the evolution of Brunnifirn around the deposition time of the archeological finds, the Middle Holocene (ca 8.2 to 4.2 ka, as defined by Walker et al., 2018, 2012) was modeled, using two different temperature reconstruction datasets. Furthermore, longer parts of the Holocene were modeled, but the onset of the Holocene could not be included, as the much colder climate of the Early Holocene (until ca 10 ka, as shown by Alley, 2000; Affolter et al., 2019a) would produce a glacier reaching the main valley (Maderanertal), resulting in poorly modeled geometry due to the resolution. Therefore, 9 ka BP was selected as starting point. At that time, the cooling of the Younger Dryas is not visible in the climate scenario anymore, and the modeling starts in a relatively warm period. The glacier therefore reaches a representative extent quite fast (see Figure 20). The 8.2 ka event is also included in the modeling.

Two proxy temperature records were used in this thesis to reconstruct glacier extents of the Holocene (Figure 8): the fluid inclusion temperature record from the Milandre cave in northwestern Switzerland (Affolter et al., 2019b) and the ice core temperature reconstruction from the Greenland Ice Sheet Project 2 (Alley, 2004). These proxy temperatures were both converted into change in ELA (see equation 2.4). The reconstruction from the Milandre cave is based on water isotope analysis. This is meaningful for surface air temperature reconstruction, as the rain water is exposed to the surface temperature, making it a robust proxy for central Europe (Affolter et al., 2019a). The GRIP2 temperatures were inferred from the water isotope analysis of the ice cores, providing a history of local temperature evolution (Alley, 2000b). The ice core data stems from a continental region which normally does not experience melt, meaning that there are almost no dampening effects from water, resulting in stronger variations in climate (Alley, 2000a).

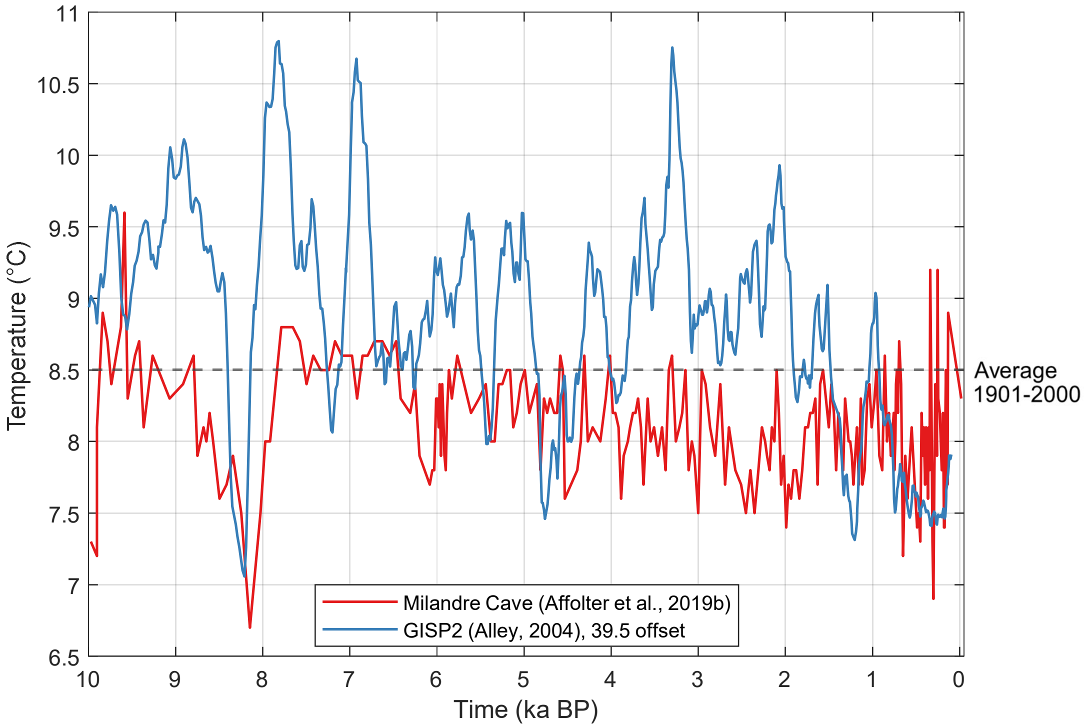

Figure 8: *The temperature reconstructions used for Holocene modeling. The gray dotted line is the average of the MeteoSwiss data from 1901–2000 (8.5019 °C). The offset for the GISP2 data was calculated in comparison with the average differences from the data for 1500–2020 CE (see Table 6). Note the strong variation of the GISP2 data. Nevertheless, the patterns are similar and clear signals like the 8.2 ka cooling are well visible in both reconstructions.*

An offset of 39.5 was applied to the Greenland Ice Sheet Project 2 (GISP2) data after comparison of averages with the temperature data for 1500–2020 CE (see *Table 6*). On the other hand, no offset was applied to the Milandre data, as a Milandre forcing with offset produces an unrealistically large glacier. As the Milandre and GISP2 data do not provide annual temperatures, calculating weighted means to allow better comparison with the data for 1500–2020 CE (annual resolution) was considered, however, weighted means would give outliers in the data set too much importance. Therefore, standard average calculations were chosen. The GISP2 data set sometimes contains two temperature values per year. In those cases, the average was calculated between the temperatures, as the model can only work with one value per year.

Table 6: *Averages of comparison period for temperature reconstructions used as forcing.*

Application period	Data source	Average temperature 1500–1649 CE	Average temperature 1650–1799 CE	Average temperature difference from 1500–2020 CE
1500–2020 CE	Casty et al. (2005a); MeteoSwiss (2023)	7.4206	7.587534	
9–0.45 ka	Affolter et al. (2019b)	8.0167	8.025	0.51576667
9–0.45 ka	Alley (2004)	-31.995132	-32.002738	-39.503001

2.3.7 Future glacier evolution

In this thesis, model runs from 2020 to the end of the 21st century are called future modeling to make experiments more distinguishable.

To assess the future evolution of Brunnifirn, two approaches were conducted to provide different perspectives on possible future change for the 21st century: firstly, results of the modeling of 1500–2020 CE were used as starting glacier surface geometries, and temperature was kept constant at the average of the MeteoSwiss data from 1991–2020 and 2001–2020 (MeteoSwiss, 2023) to produce change in ELA, as described in equation 2.4. Secondly, the Swiss climate scenarios CH2018 (CH2018 Project Team, 2018) were used to force the model. The modeled period starts in 1981, so a starting surface geometry of the modeling of 1980 was used to then model the period from 1981 to 2099. The daily temperatures were transferred into averages of summer months (June, July, August) to get one value per year, which was then translated into change in ELA (according to equation 2.4). Strongest warming occurs during summer (CH2018, 2018), the modeled glacier therefore represents the most extreme aspects of the future projections.

The CH2018 scenarios are based on the EURO-CORDEX regional climate simulations, which provide three different future projections for future climate change according to three different Representative Concentration Pathways (RCPs) (CH2018, 2018). The data was produced by applying statistical bias-correction and downscaling (Quantile Mapping) to the EURO-CORDEX data (CH2018 Project Team, 2018). The three future projections are: strong reduction of emissions through mitigation measures (RCP2.6; global mean temperature warming < 2 °C until 2100), less emissions after 2050 (RCP4.5; global mean temperature warming of ca 2 °C), and no reduction of emissions and unceasing warming (RCP8.5; global mean temperature warming of 4–5 °C until 2100) (IPCC, 2013). It is important to note that these projections were modeled including political, economic and social decisions, and therefore are not predictions (CH2018, 2018). By modeling three different RCP projections, the future change of Brunnifirn can be constrained as precisely as possible with the CH2018 temperature data.

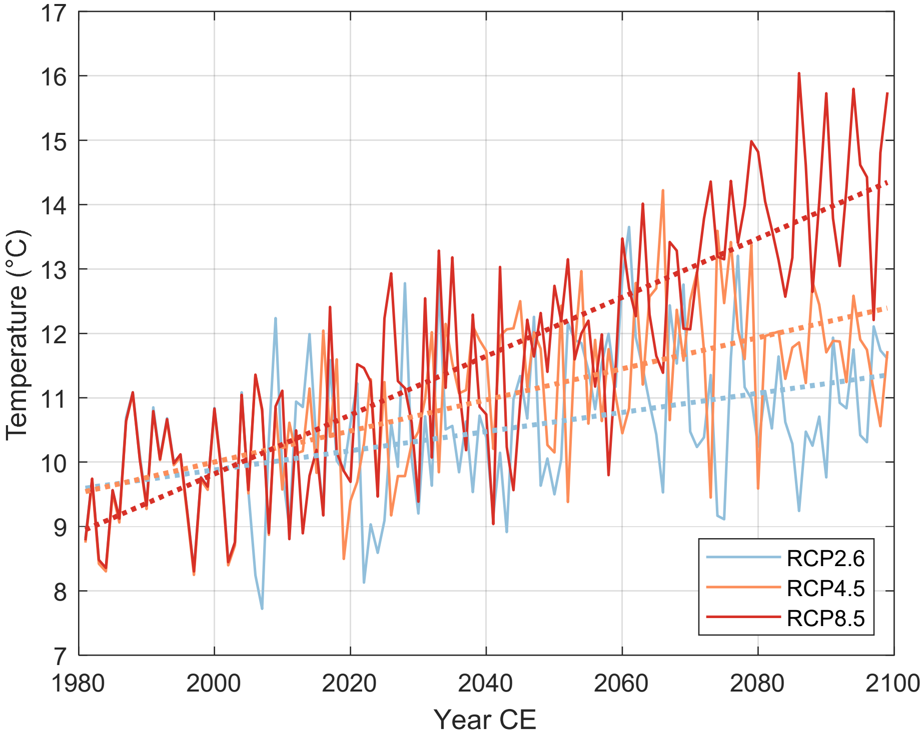

Figure 9: *Exemplary CH2018 simulation (DMI-HIRHAM_ECEARTH) temperature projections for three RCPs for Disentis (closest station to Brunnifirn). The dotted lines are the respective trends. The displayed data is adjusted for Brunnifirn by fitting it to the >1000 m a.s.l. temperatures from MeteoSwiss (2023), as shown in Table 7.*

The data utilized here comes at station-based resolution, meaning the closest station had to be selected. From all EURO-CORDEX model simulations, the projections were selected by availability of daily temperatures and according to high spatial resolution (EUR11: ca 12km), leaving four data sets, listed in *Table 7*. The simulations are quite similar and usually values do not differ more than ca 1 °C, except for the SMHI-RCA simulation, in which warming is stronger. To increase robustness of the possible future glacier evolution, all four simulations were used. An exemplary simulation is plotted in Figure 9, the other three simulations are displayed in the appendix (Figure 51; Figure 52; Figure 53). The closest station represented in all four data sets is Disentis (CH2018, 2018). With an elevation of 1197 m a.s.l., the data had to be approximated to fit the alpine climate of Brunnifirn. This was achieved by correcting the temperatures with an offset (cooling) found by comparing the 1981 to 2021 period of each data set with the MeteoSwiss data for elevations above 1000 m a.s.l. in northern Switzerland (MeteoSwiss, 2023). The overlap for the 1981 to 2021 period is therefore more precise, providing a better transition from present to future temperatures. The offset in temperature was rounded to the second decimal point (all offsets are listed in *Table 7*). This translates to an accuracy of 1.3 m ELA change, as the sensitivity factor ELA_{fc} is set to 130.

The result of modeling of 1980 served as starting surface geometry, and all four possible future projections were modeled for each RCP scenario from 1981 to 2099. Modeling as many simulations as possible minimizes the climate model and greenhouse gas scenario uncertainties (Feigenwinter et al., 2018), which increases understanding of the future evolution of Brunnifirn.

Table 7: *The CH2018 simulations with respective scenario and the calculated difference from the MeteoSwiss data, which was then subtracted as offset to account for the lower elevation of Disentis compared to the glacier. REMO1 and REMO2 are based on the same model but have different initial conditions (CH2018, 2018).*

Simulation name	Greenhouse gas scenario	Average difference from MeteoSwiss data (1981–2021)
DMI-HIRHAM_ECEARTH	RCP2.6	4.97
MPICSC-REMO1_MPIESM	RCP2.6	5.14
MPICSC-REMO2_MPIESM	RCP2.6	5.06
SMHI-RCA_ECEARTH	RCP2.6	4.89
DMI-HIRHAM_ECEARTH	RCP4.5	4.96
MPICSC-REMO1_MPIESM	RCP4.5	5.1
MPICSC-REMO2_MPIESM	RCP4.5	5.08
SMHI-RCA_ECEARTH	RCP4.5	4.91
DMI-HIRHAM_ECEARTH	RCP8.5	4.87
MPICSC-REMO1_MPIESM	RCP8.5	5.08
MPICSC-REMO2_MPIESM	RCP8.5	5.15
SMHI-RCA_ECEARTH	RCP8.5	5.03

3 Results

This chapter follows the structure of the methods, starting with mapping outcomes, then continuing with landform age dating results, and ending with numerical modeling outputs. Even though ELA estimations incorporate results of modeling, they are listed before the modeling results, as they are relevant for steady state modeling. Modeling outputs are displayed in geomorphological maps for the LIA extents of Brunnifirn, Staldenfirn and Glatscher da Strem, and for the moraine cluster above 2200 m a.s.l. This makes modeling results more graspable and conversely provides visualizations of glacier extents for the mapped moraines.

3.1 Mapping

The field mapping as well as the digital remote mapping provided an abundance of landforms. The digital remote mapping was crucial to prepare for the field and focus on the sections of the valley with relevant moraines. Vice versa, the field mapping allowed in-situ analyses of remotely mapped moraines and addition of missed forms. In the field, especially mapping on printed aerial images proved to be useful, as identifying landforms in the field is mostly easier than doing so remotely. Nevertheless, the digital remote mapping allowed for mapping in areas inaccessible due to time constraints, such as the Val Strem (where Glatscher da Strem used to flow through), Staldental (where Staldenfirn used to flow through), Tscharren (a valley where a glacier named Bächenfirn, flowing westward from below the peak of Oberalpstock, used to flow through), and Val Cavardiras and its side valleys (see Figure 23).

The mapping results are displayed as field maps, digital remote maps, and a combination of both.

3.1.1 Field mapping

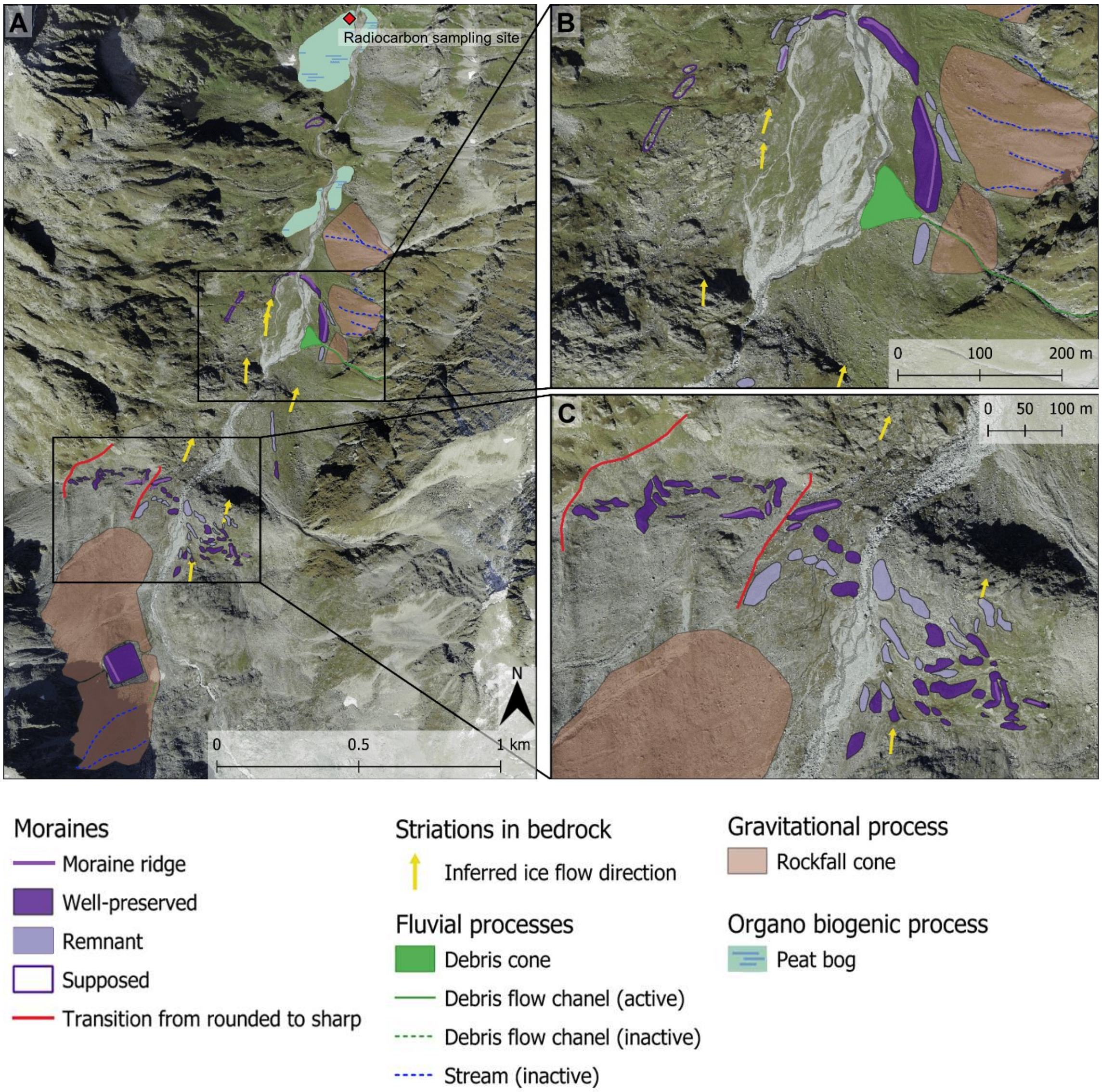

Figure 10: *Geomorphological map of the upper Brunnital, based on field mapping. A) The upper part of the valley and overview of everything that was mapped. The moraines and inferred ice flow directions (yellow arrows) give insight of past glacier extents and ice movement. B) Detail inset of the LIA moraine complex, with double ridge indicating multiple advances to the same position. C) Detail inset of the upper moraine cluster, where an abundance of moraine material was found.*

The mapping in the field allowed for a detailed analysis of small forms and ridges. Especially the large *well-preserved* moraine in the front of the moraine complex (on the orographic right of the river, see map B in Figure 10) revealed a second ridge, which could not be deciphered on the aerial images. Generally, ridges were mapped onto moraine features, to mark the highest point and shape of moraines. Further, all moraines categorized as *remnant moraines* could only be identified in the field. Though they could be suspected on the aerial images, validating these assumptions in the field was essential. Mapping was easiest when conducted from a high vantage point, and when the sun hit the surface at an angle casting short shadows, as this made the smaller moraine *remnants* more distinguishable. In the next paragraphs, the significance of the mapped landforms other than the latero-frontal moraines is briefly explained.

***Supposed moraines*:** Four small hills in the landscape were classified as *supposed moraines.* The northernmost moraine (map A in Figure 10) lies just before a steep section of the valley, after which a plain with the mapped and age dated peat bog follows. During a retreat, the glacier would rapidly recede over the steep section and stand still above it, allowing for the deposition of a moraine. The three *supposed moraines* on the orographic left of the LIA moraine complex (map B in Figure 10) seem like extensions of the latero-frontal *moraine remnants.* They would complete the large latero-frontal moraine complex, which is indicated by the *well-preserved moraines* on the orographic right.

Peat bog: Mapping and age dating this landform proved to be a useful constraint for maximum extents and a form of temperature forcing validation: if a temperature forcing caused the glacier to override the peat bog within the age it was dated for, this would make the forcing less credible. During an advance the glacier would erode at least the upper layers of the peat bog, resulting in a younger age dating result.

Transitions from rounded to sharp: The deposited rock material at the surface changed its appearance from rounded to sharp at these boundaries (red lines in Figure 10, photos in Figure 11). On the orographic left of the red lines, sharp material was probably deposited by rockfall, whereas the glacier could have deposited the rounded material on the orographic right. The change in material interestingly occurred again at the outer second line (further to the west), which might indicate two different limits of glacier extent.

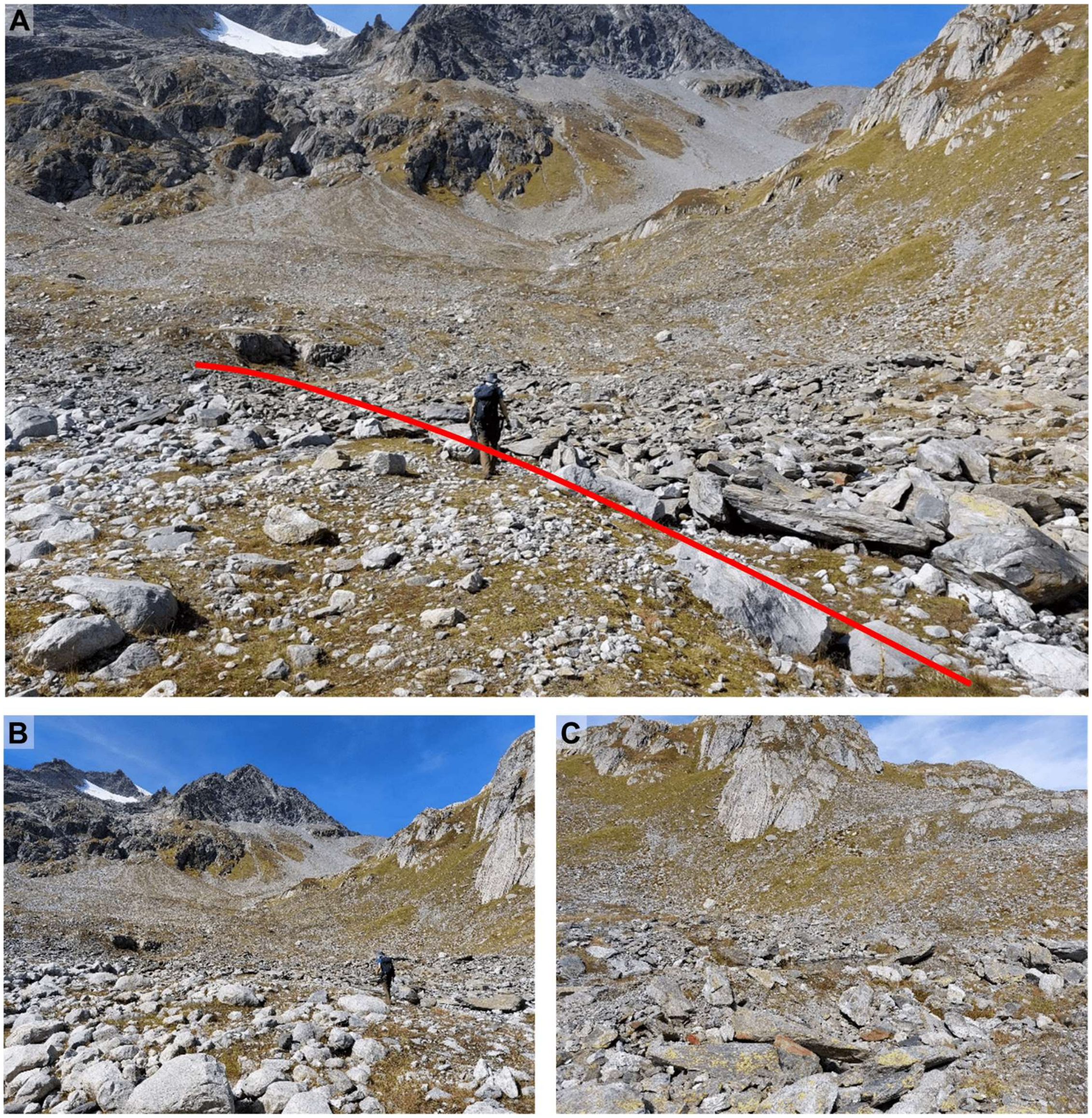

Figure 11: *Transition from rounded to sharp deposited rocks, as mapped in Figure 10 (eastern line of the two mapped). The red line in image A shows the transition, where rounded material is found to the left of the line, and sharp material is deposited on the right side of the line. Image B is a close-up shot of the rounded material (assumably deposited by the glacier), image C shows the sharp material (assumably deposited by rockfall). Photos: Jonathan Davidson in 2022.*

Fluvial and gravitational process area: To help understand the chronology of moraine deposition, fluvial and gravitational processes were included, as they affect moraines. The rockfall cones are signs of high geomorphological activity, as many of the rocks were not overgrown by vegetation, indicating that they were deposited quite recently. High rockfall activity also points towards burial of moraines, which explains why the eastern latero-frontal moraines of the LIA moraine complex are just *moraine remnants*.

The debris flow channel divides a *well-preserved moraine* and a *moraine remnant* (see map B in Figure 10), and debris flows might have destroyed other moraines there. Concerning the chronology, the debris flow channel must have recently been active, as the fan was deposited after the glacier has retreated from its LIA maximum.

Finally, the inactive streams mapped within the rockfall cones are again a sign of geomorphological activity. The inactive streams in the large southern rockfall cone (see map A in Figure 10) seem to be signs from when there was more ice in that steep slope of the valley.

3.1.2 Remote mapping

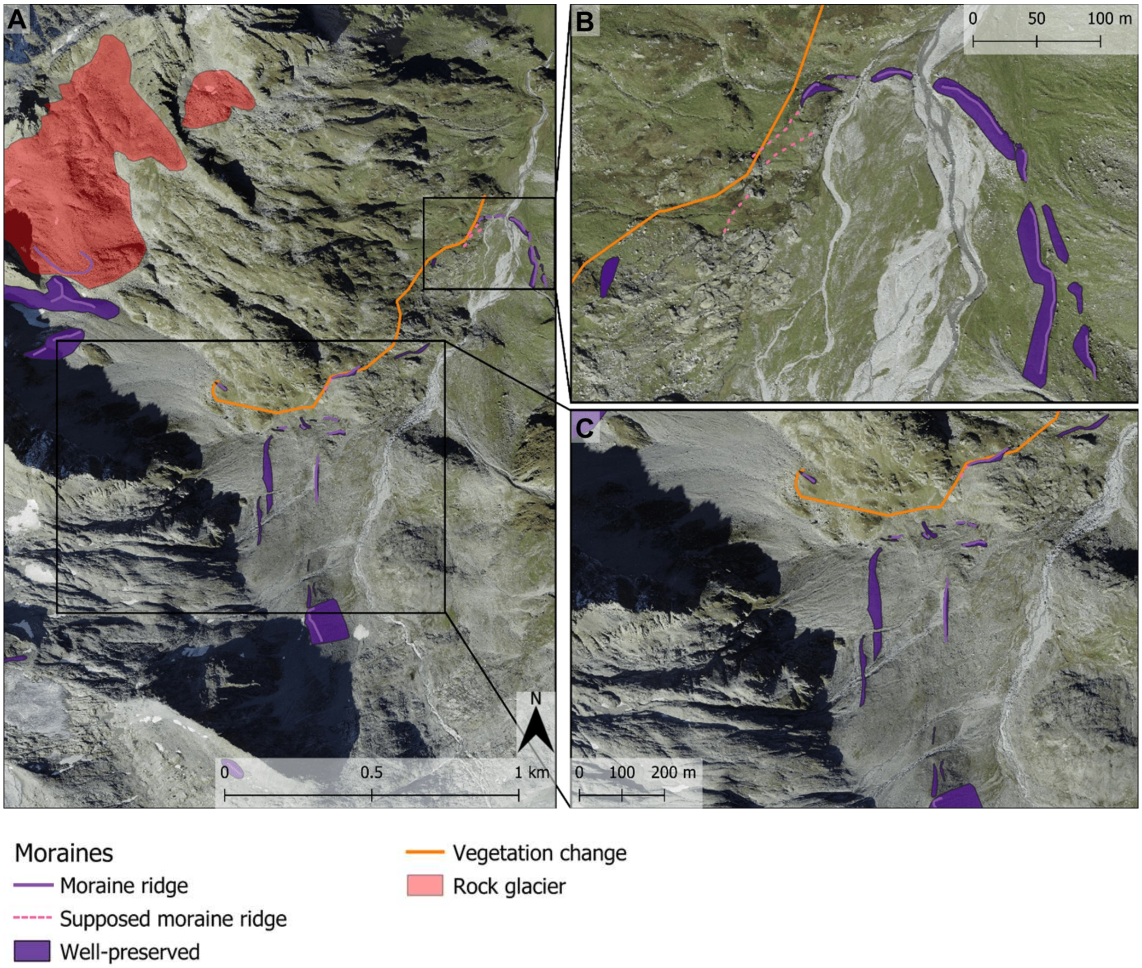

Figure 12: *A) Geomorphological map of the upper Brunnital, based on remote mapping with aerial images. Vegetation changes imply recent ice cover below the line. B) Detail inset of the LIA moraine complex, showing a second outer row of latero-frontal moraines to the orographic right, and supposed ridges as continuation of the frontal moraines on the orographic left. C) Detail inset of the upper moraine complex and numerous lateral moraines in the steep western valley slope. Most large moraines show clear ridges (bold purple lines) which indicate past ice extents. Background map: swisstopo (2023).*

The field map (Figure 10) is more detailed, however the aerial image map covers larger areas (see Figure 41 in the appendix for entire remote mapping overview). This allows for inclusion of rock glaciers and moraines in other valleys which are especially insightful for model validation, as they can be compared to glacier extents of modeling outputs.

Moraines: Only *well-preserved moraines* were mapped in the remote mapping process. Moraines which are not *well-preserved* are not distinctive enough to be recognized in remote mapping. However, supposed ridges were included, which are linear extensions of moraines or connections between moraines. They cannot be classified as clear ridges due to only consisting of little deposited moraine material, or sometimes even just resembling trimlines. They are, however, visible linear forms in the surface, recognizable in aerial images.

Vegetation changes: The remote mapping revealed strong changes of the surface vegetation, which could only be suspected in the field. Below these lines, vegetation is sparse and does not appear as developed as above. This is an indicator of recent ice cover below the lines, where vegetation did not have a lot of time to develop yet.

Rock glaciers: These periglacial forms were mapped because they complement the position of moraines. As rock glaciers can originate in debris-covered glaciers (Benn and Evans, 2010), finding a current rock glacier surrounded by moraine ridges points towards past ice coverage of that area.

Latero-frontal and hummocky moraines: The form of the moraine outlines offered an easy distinction of moraine types into two classes: latero-frontal and hummocky (descriptive terms as proposed by Benn and Evans (2010)). They were found in remote and field mapping, which is why a combined map was produced (Figure 13).

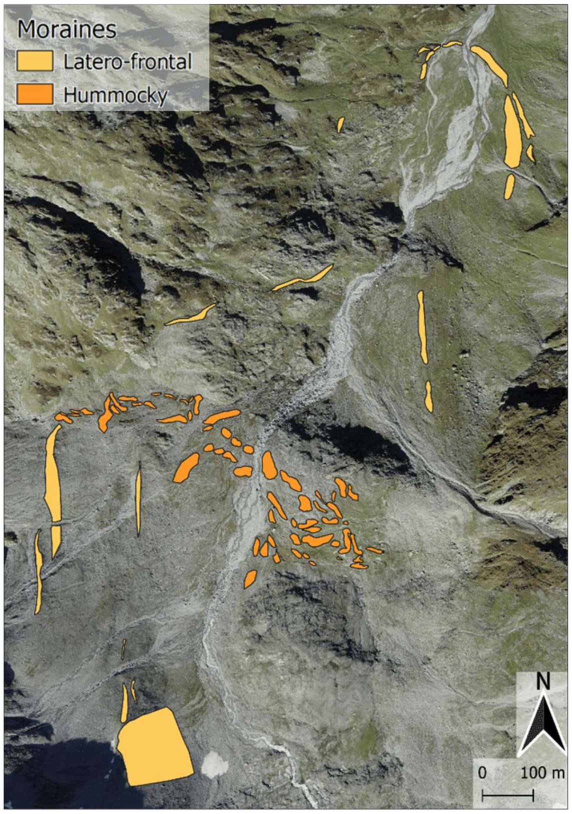

Figure 13: *Classification of moraine types, based on aerial image and field mapping. Background map: swisstopo (2023).*

Old aerial images: To help constraining the retreat of the glacier in the last century, the glacier extent was mapped from aerial images (swisstopo, 2023a) which show significant length changes. This resulted in an overview of the retreat since 1946 (Figure 14), and even if only four images were used, the outlines provide an understanding of how the glacier acts during rapid warming as experienced in the last ca 60 years. Mapping errors along the mountain ridges occur due to inaccuracies in the orthorectification process.

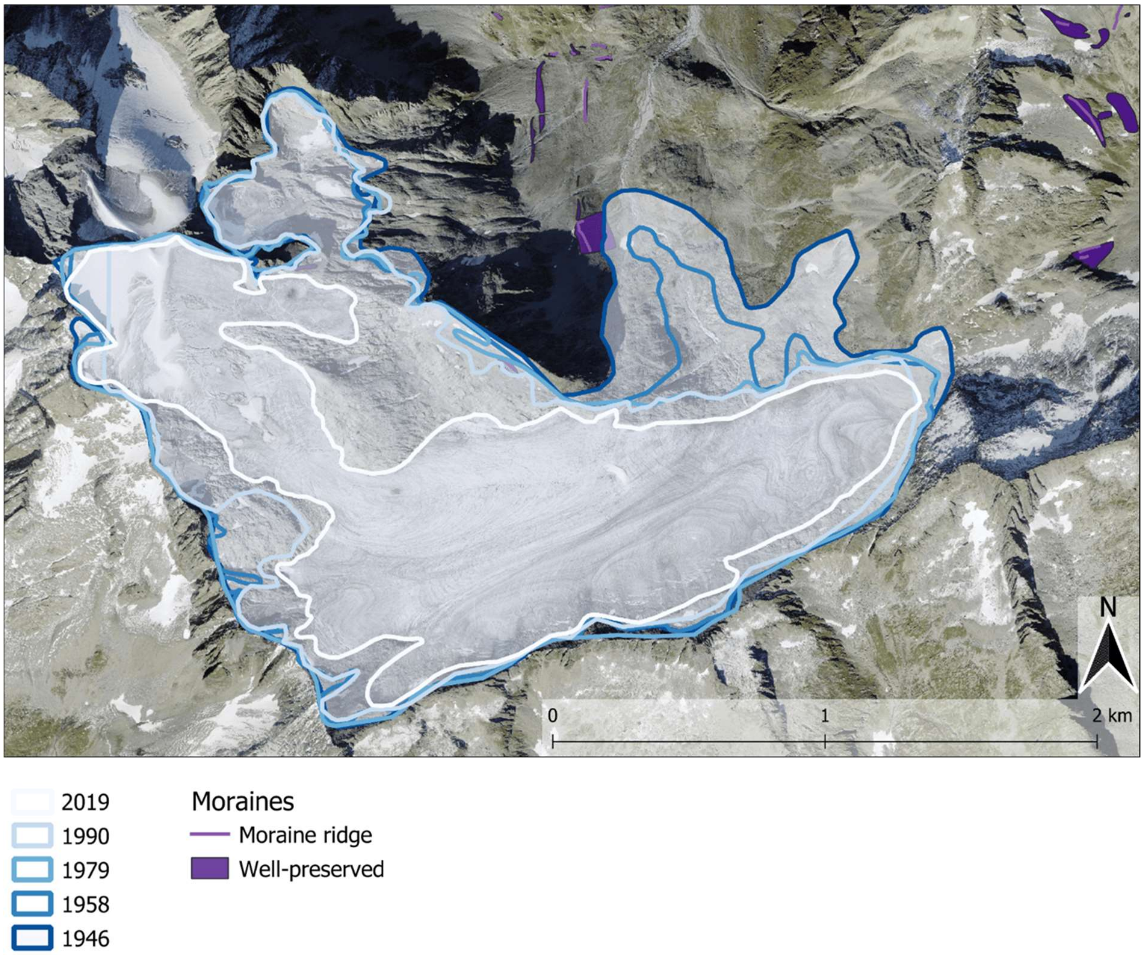

Figure 14: *Glacier outlines mapped from old aerial images. Note how the tongue position between 1979 and 1990 does not change. This is a result of excluding a piece of dead ice present in the 1979 image, because it is completely disconnected from the glacier tongue. Background map and old aerial images: swisstopo (2023).*

In the images from 1979 and 1990, the tongue is located at same position, but in the 1979 image, there is a big piece of disconnected dead ice which is not an active part of the glacier anymore. For the sake of length change reconstruction, it was however counted as part of the glacier to allow comparison with the results of the modeling of 1500–2020 CE. The model takes the furthermost piece of ice along the flow line to measure length, so it makes sense to include the dead ice located on the flow line as part of the glacier when comparing with modeling outputs.

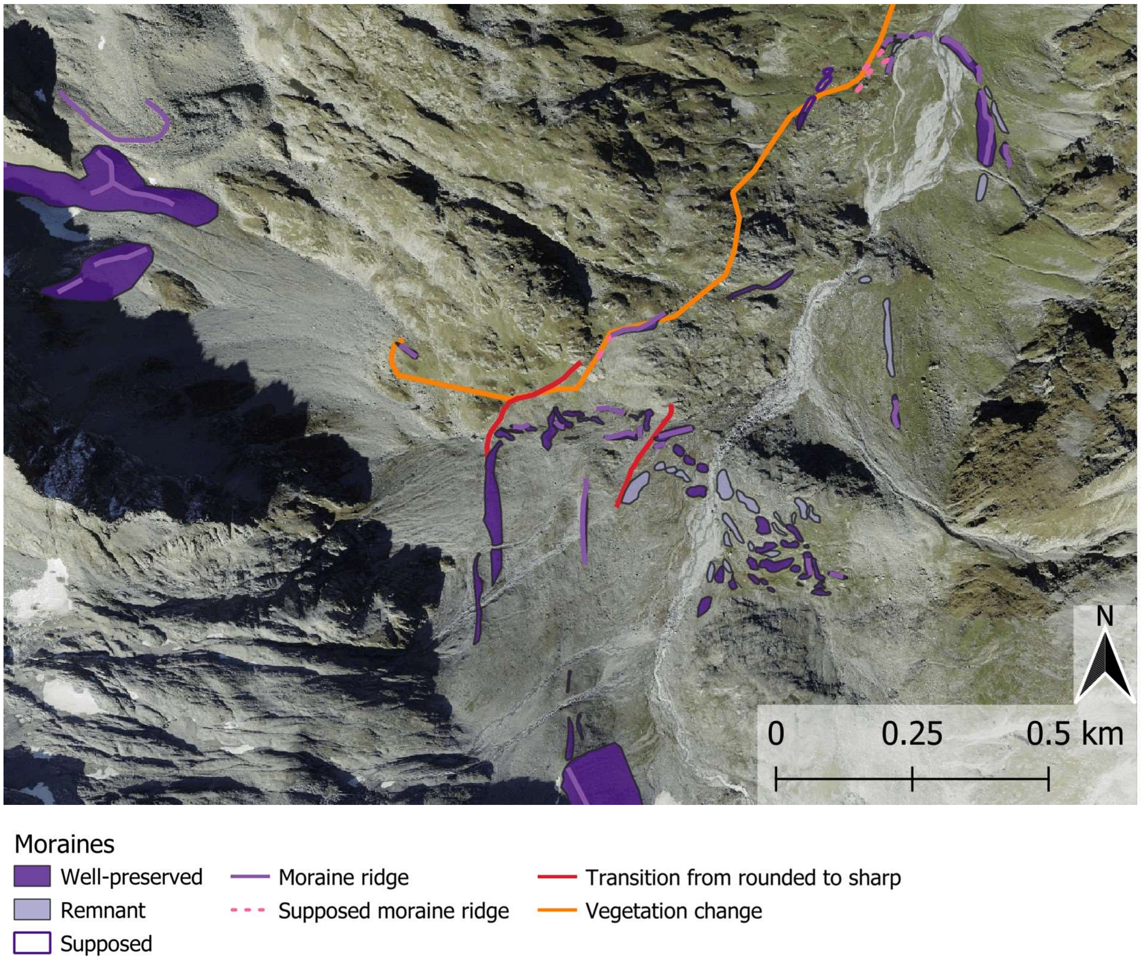

Figure 15: *Integrated map of geomorphological landforms which indicate past glacier extents. Elements of field and remote mapping are combined. Background map: swisstopo (2023).*

The combination of field and remote mapping shows how the results of the different mapping methods fit together (Figure 15). Vegetation changes and transition from rounded to sharp rock debris at the surface are in line with moraines and seem like connections between them.

3.2 Radiocarbon dating

The ages of the dated organic material allows to constrain fluctuations of Brunnifirn temporally. The soil sample extracted from below boulders in the LIA moraines is far older than the period of the LIA with a calibrated age of ca 12.5 ka BP (see Table 8 for exact ages). This indicates that the glacier deposited the material that was dated before ca 12.5 ka BP, or that an old soil was eroded at a different location and deposited at the moraine.

The sample from the peat bog was not extracted from the deepest horizon (see Figure 5) meaning that the deeper layers are probably older than the one dated to ca 3.8–3.5 ka BP. Here, the age of the sample implies that the glacier did not extend over the position of the peat bog, as it would have been destroyed by an advance of those dimensions.

Table 8: *The ^{14}C ages of the two sampling sites (see Figure 3 for locations). A second sample taken from the LIA moraine could not be age dated due to insufficient organic content.*

Sample location	Elevation (m a.s.l.)	Uncalibrated age BP	Calibrated age BP (68.3% probability)	Calibrated age BP (95.4% probability)
Moraine soil (LIA)	2070	10556 ± 52 a BP ($\delta^{13}C$: -18.8 ± 1.0‰)	12673–12491	12703–12476
Peat bog	2035	3388 ± 33 a BP ($\delta^{13}C$: -21.9 ± 1.0‰)	3685–3574	3814–3494

3.3 ELA estimations

Based on the mapping and numerical modeling, ELAs for three extents were compared: today's extent, an extent reaching the upper moraine cluster (see map C in Figure 10), and an extent reaching the LIA moraine complex. It is important to keep in mind that the ELAs derived from numerical modeling are based on steady state geometries, as this is the clearest way to match a specific extent, but this also results in an overestimation of ELA values. The steady states were reached with buildup of ice, which means that in transient phases, the same ELA would probably produce a shorter extent (or a longer one during a phase of retreat from a larger extent, respectively). The ratio between accumulation and ablation area was found to be around 0.66 but this assumption varies depending on glacier geometry and mass balance gradient (Mackintosh et al., 2017). Nevertheless, the glacier area was measured and divided into two parts where the accumulation area is double the size of the accumulation area. This results in large inaccuracies, as the division, i.e., the ELA, between the two areas is hard to find at constant elevation while still respecting the ratio of 0.66. The values in Table 9 are therefore given with a range or strongly rounded. The mean elevation method is calculated by adding the elevation of the lowest point at the glacier tongue to the elevation of the highest point of the bergschrund (Leonard and Fountain, 2003). This was achieved by determining the elevation of the frontal LIA moraine, an average elevation of the upper moraine cluster, and an average elevation of today's tongue. The elevation of the bergschrund was determined with the 2019 aerial image and had to be averaged as well, as it does not lie at the same elevation over its whole width.

Table 9: *ELA values based on two theoretical methods and numerical modeling, for three different glacier extents. Note that the numerical modeling ELAs are based on steady state extents.*

ELA calculation method	Current extent ELA (m a.s.l.)	Upper moraine cluster ELA (m a.s.l.)	LIA extent ELA (m a.s.l.)
Mean elevation	2'904.25	2'740.92	2'657.58
AAR	2740–2750	2600–2650	2600
Steady state modeling	2730	2650	2585

The current extent steady state ELA of 2730 m a.s.l probably is set too high, as compared to the aerial image, the model output is too small. Lowering the ELA by just one meter however resulted in the tongue flowing over the edge of the plain into the steep slope. As steady states are a theoretical concept, comparisons must remain critical, and thus the approximation to the actual glacier extent can be used.

3.4 Numerical modeling

The 2-D ice-flow model (as applied by Brown et al., 2013; and Evans et al., 2012) was first employed for steady state experiments. Glacier response to fluctuating climate was explored in sinus experiments. The next step was to use the temperature reconstructions as climatic forcing and adjust the reference ELA and temperature-ELA conversion factor. For this, the temperature forcing of 1500–2020 CE was used (Figure 7). Finally, the period of 1500–2020 CE, the Holocene, and the future scenarios were modeled, each based on the temperature forcings listed in Table 3.

3.4.1 Steady state and step change

After initial reproduction of current and past glacier extents (extents reaching: the edge of the plateau, the upper moraine cluster, the LIA moraine complex), the ELA was lowered by 50 m increments. The end geometry of the next respective higher ELA steady state was used as starting glacier surface geometry (with no ice for the first experiment). The upper boundary was given by the maximum elevation of Oberalpstock (3328 m a.s.l., so a maximum ELA of 3300 m a.s.l.), and the lower boundary was set at 2400 m a.s.l., and ELA value which caused the glacier to extend over the steep section at the end of Brunnital, into the main valley, Maderanertal. This lower boundary was chosen because an extent of Brunnifirn flowing into Maderanertal would require colder climatic conditions than the ones found during the part of the Holocene considered in this thesis (from 9 ka onwards).

The 50 m increments of ELA change were repeated for a retreating glacier, meaning the 2400 m a.s.l. ELA steady state geometry was the starting point, and the ELA was increased for each steady state. The respective next lower ELA steady state served as starting glacier surface geometry.

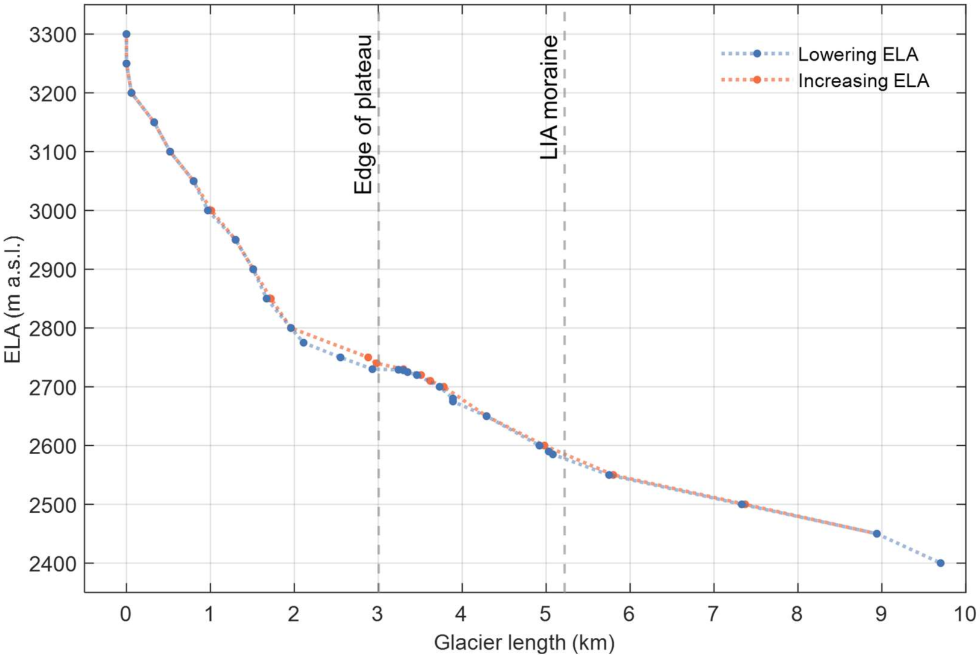

Figure 16: *Steady state lengths for a range of ELAs, for an advance and a retreat case (lowering or increasing ELA, respectively). Upper boundary: elevation of Oberalpstock; lower boundary: ELA causing Brunnifirn to flow into Maderanertal. Steady state was declared when the glacier did not change its length for at least 100 years.*

Length results of lowering and increasing the ELA are mainly similar (Figure 16), except for especially the zone between ca 2 and 4 km length, where a hysteresis is discernible: the steady states modeled by increasing ELA are longer than those modeled by lowering the ELA (plot A in Figure 17). This hysteresis probably occurs because during an advance the ground in front of the glacier is ice free, and the glacier needs to advance into warmer climate. During a retreat on the other hand, the glacier tongue moves into colder regions where there already is ice. This influence on local climate probably is enough to alter mass balance, causing steady states reached by increasing the ELA from larger starting extents to reach equilibrium with bigger lengths. The bed geometry (plot B in Figure 17) probably supports the hysteretic behavior, as the large overdeepening first needs to be filled during glacial advance, leading to smaller changes in length, even when the tongue starts to flow over the edge of the plateau. When the overdeepening is filled sufficiently, however, lengths increase strongly.

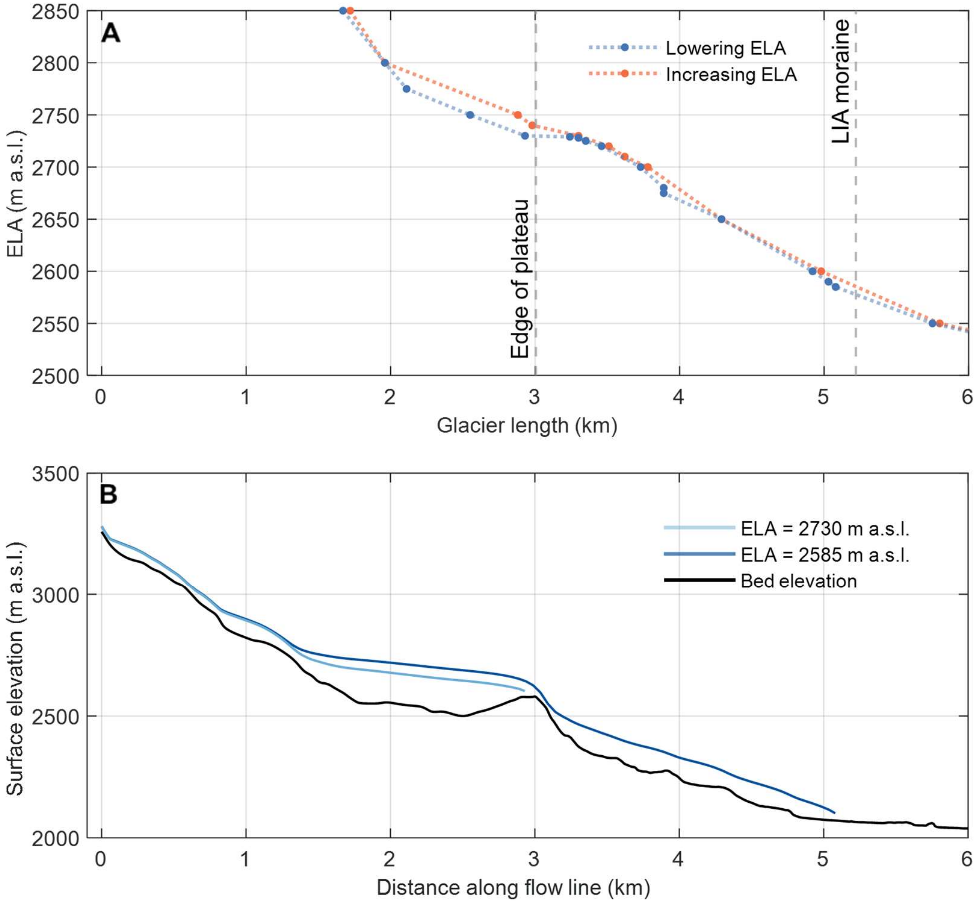

Figure 17: *A) Detail of steady state lengths shown in Figure 16 better illustrate the hysteresis. Note that experiments where not conducted for all ELAs equally: for both decreasing and increasing ELA, 50 m increments were followed. However, additional experiments for smaller ELA variations were conducted irregularly. B) Glacier surface elevation along flow line. Light blue: steady state approximation of today's glacier surface (ELA: 2730 m a.s.l.). Dark blue: steady state surface reaching LIA moraine complex (ELA: 2585 m a.s.l.).*

The steady state for 2730 m a.s.l. ELA is the best approximation of today's extent but does not fill whole plain towards the east (see Figure 42 in the appendix). Lowering the ELA by just a few meters causes glacier to flow over the edge, which is not the case anymore today. Compared to the 2019 aerial image extent, the model overestimates the ice extent at the eastern flank of Oberalpstock, where there is no more ice left today. The extents of Glatscher da Strem and Staldenfirn are overestimated as well. However, this is a comparison of a theoretical steady state to a rapidly retreating glacier, and therefore can be used as reference of today's glacier size, if the disparities are kept in mind.

3.4.2 Response time

To better understand the climate sensitivity of Brunnifirn, response times were calculated. Transient modeling results can be better interpreted when the reactions of the glacier are better understood.

Volume *e* folding time

Thanks to working with a numerical ice-flow model, theoretical response times could be calculated. Changes in climate cause changes in glacier length, which come with a time lag but are easily documentable in the field. Glacier volume however immediately adjusts to climatic changes. The resulting response time, the time until a glacier has fully adjusted to climatic change and has reached a new equilibrium state, cannot be measured (Solomina et al., 2015). Thus, when working with field observations only the reaction time resulting from measuring length changes can be looked at. The numerical ice flow-model on the other hand also documents changes in volume, allowing for calculations of the immediate response times.

The step change experiments of lowering the ELA show clearly how long it takes the overall volume to reach equilibrium state after initiation of an ELA step change. From these results, volume *e* folding times were calculated (Table 10). As ELA step change experiments were conducted for an advancing glacier, the *e* folding time thus is the time until glacier volume reaches $1 - e^{-1}$ of the steady state volume (as applied by Leysinger Vieli and Gudmundsson, 2004), roughly corresponding to two thirds of the total volume change.

Table 10: *Response times, i.e.,* e *folding times, calculated from lowering ELA step change experiments. Due to modeling resolution, response times are given as 10-year maximum and minimum values. Step change increments are 50 m, as volume changes of smaller increments are not discernible enough.*

ELA (m a.s.l.)	Steady state volume before step change (m^3)	Steady state volume after step change (m^3)	$\frac{2}{3}\,\Delta V$	$(1 - e^{-1})\,\Delta V$	Min./max. response time (a)
3050	5133387.3	8200155.3	7157454.18	7071954.4	60–70
3000	8200155.3	11890145	10635548.5	10532673.7	30–40
2950	11890145	19037615	16607475.2	16408207.7	60–70
2900	19037615	26227857	23783174.7	23582714.8	40–50
2850	26227857	35436035	32305254.5	32048535.6	40–50
2800	35436035	50573532	45426783	45004758.1	50–70
2750	50573532	83036723	71999238.1	71094182.4	80–100
2700	83036723	189417330	153247924	150282092	160–180
2650	189417330	247039370	227447876	225841406	60–70
2600	247039370	306436610	286241548	284585587	40–50
2550	306436610	387522930	359953581	357692940	40–60

Theoretical response time

Thanks to modeling outputs including the mass balance at the terminus, simple calculations for theoretical response times could be conducted. Results of these calculations are expected to be comparable to the adjustment time of the glacier volume, i.e., the *e* folding time (Jóhannesson et al., 1989).

Table 11: *Response times calculated from steady state geometries with the approach developed by Jóhannesson et al. (1989). Note how the formula is not applicable for decimal ablation values (2730 m a.s.l. ELA), as this leads to irrationally high values. Ice thickness values are maximum values along the flow line.*

ELA (m a.s.l.)	H_{max} (m)	b_t (m a^{-1})	τv (a)
2800	67.1417	-1.3475044	49.8267019
2730	145.4416	-0.6134903	237.072363
2720	166.5243	-2.1079712	78.9974265
2585	188.1549	-3.0227569	62.2461237

Values calculated according to Jóhannesson et al. (1989) for steady states of a glacier smaller than today (2800 m a.s.l. ELA), approximately as large as today's extent (2730 m a.s.l. ELA), slightly flowing over the edge of the plateau into the steep section (2720 m a.s.l. ELA), and as large as the LIA maximum, are compiled in Table 11. For the thickness, the maximum, H_{max}, determined along the flow line was used. The ablation b_t was extracted from the last grid point along the flow line.

Response times were calculated for the same steady state extents as above with the method described by Harrison et al. (2003) and are compiled in Table 12. For the thickness, the effective maximum, He_{max}, and the average effective maximum, He_{avg}, along the flow line were used. The ablation b_e was again extracted from the last grid point along the flow line.

Table 12: *Response times calculated from steady state geometries with the extended formula by Harrison et al. (2003), given for maximal and average ice thickness values along the flow line. Note how the formula is not applicable for decimal ablation values (2730 m a.s.l. ELA), as this leads to irrationally high values.*

ELA (m a.s.l.)	He_{max} (m)	He_{avg} (m)	b_e (m a^{-1})	γ_e (a^{-1})	τv_{max} (a)	τv_{avg} (a)
2800	67.1417	43.3914708	-1.3475044	0.007	76.5136679	41.5721049
2730	145.4416	79.7293684	-0.6134903	0.007	-359.46931	1439.55476
2720	166.5243	80.7705329	-2.1079712	0.007	176.720902	52.3607627
2585	188.1549	91.8138523	-3.0227569	0.007	110.311264	38.5762774

In both cases, the response time values are comparable to the *e* folding times derived from ELA step change experiments (Table 10). The only case where results are completely different is the 2720 m a.s.l. ELA steady state. In this case, the glacier flows over the plain and terminates in the steep section, which leaves the calculated ablation at the tongue too small, causing the response times to be exaggerated.

3.4.3 Sinus experiments

To examine the climate sensitivity of the glacier, ELA sinus experiments were conducted. The ELA was forced into sinus wave behavior with an amplitude of 200 meters, meaning that the minimum and maximum ELA values of a sinus wave are 100 meters lower or higher, respectively, than the initial ELA (ELA0). This was maintained while altering the period of the sinus wave for values of 20, 50, and 100 years. The starting glacier surface geometry was a steady state extent of the respective initial ELA. These variations were performed for four glacier types: a small glacier (ELA0 = 2800 m a.s.l., Figure 18), today's extent (ELA0 = 2730 m a.s.l., Figure 44), an extent slightly larger than the edge of the plain (ELA0 = 2720 m a.s.l., Figure 43), and a LIA extent (ELA0 = 2585 m a.s.l., Figure 19).

Today's extent and the one slightly larger than the plain were purposely chosen to be this similar to better understand the length feedback when the initial state lies within the plain versus when the initial state already exceeds the plain into the steeper section.

The sinus experiments show that a small glacier reacts a lot faster than a glacier reaching LIA extent, as expected. Also, the larger the glacier, the less length change occurs for the 20-year sinus period. The volume however always shows clear changes, even in the case of the LIA extent with a 20-year sinus period (Figure 19). This underlines the assumptions of time lag of reaction time versus response time: the volume response time which is a theoretical value (Solomina et al., 2015) occurs immediately after a shift in ELA, and is just slightly delayed. The length response on the other hand occurs with a large delay to the climate signal. Interestingly, the case of the large LIA extent shows less delay in volume response time than the theoretical calculations suggest (see Table 10, Table 11, and Table 12). This may result from the ablation value used for theoretical calculations being too low.

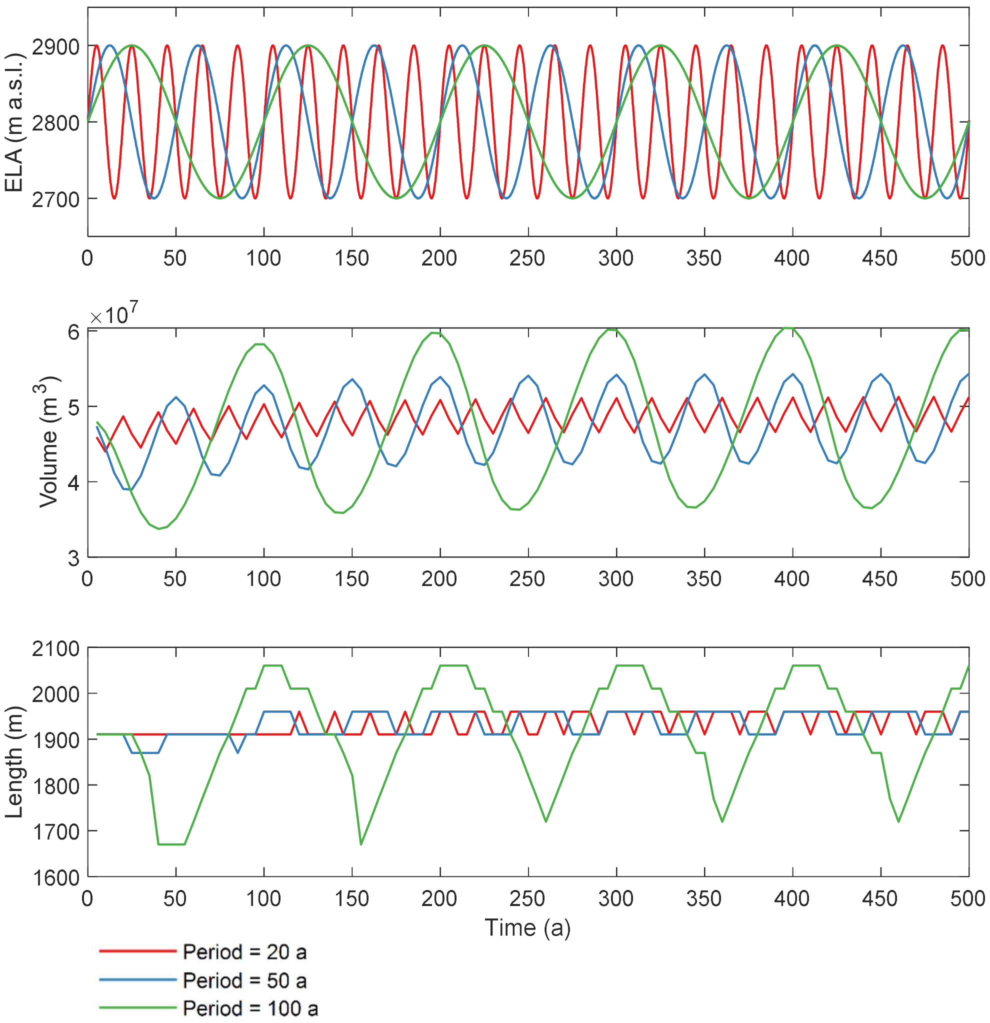

Figure 18: *Sinus ELA forcing around an ELA0 of 2800 m a.s.l., with sinus periods of 20, 50, and 100 years. Even the rapid change in climate signal resulting from the 20-year period is visible in volume and length change. Length does not lag far behind volume change.*

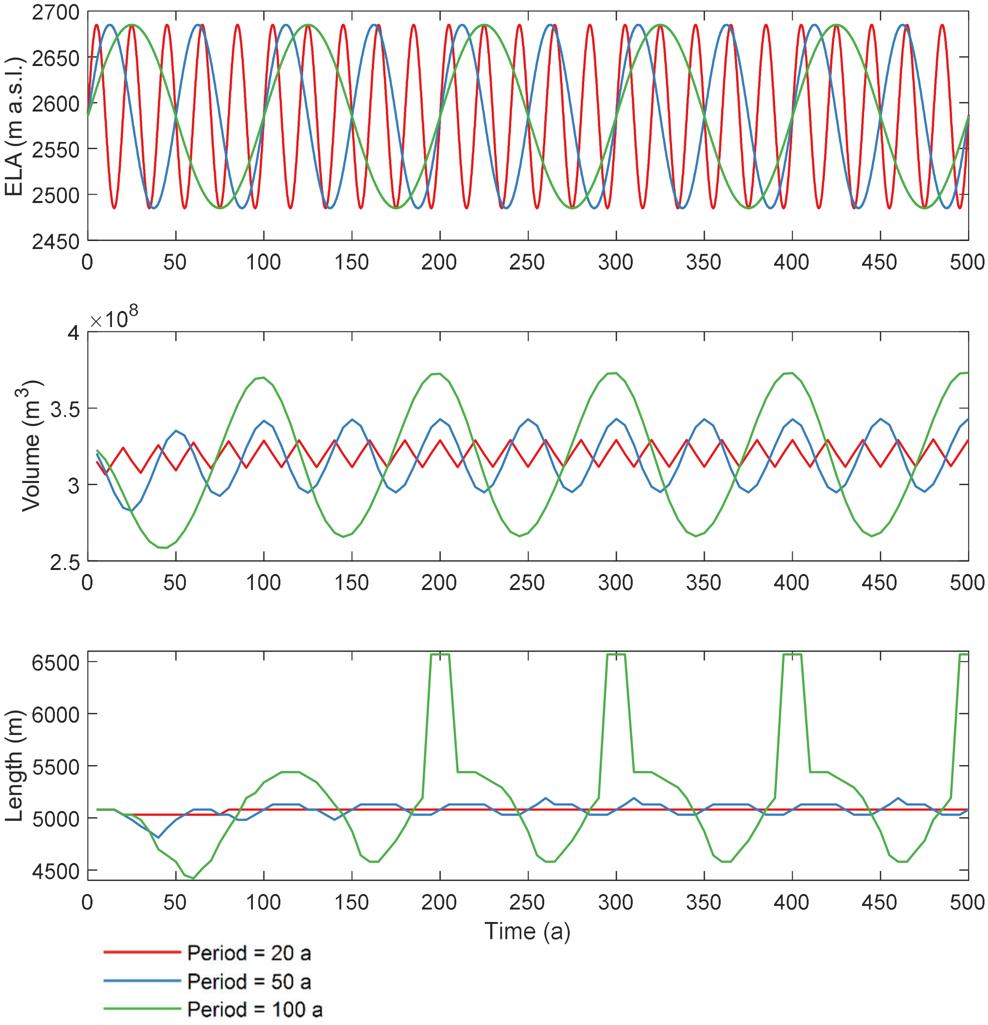

Figure 19: *Sinus ELA forcing around an ELA0 of 2585 m a.s.l., with sinus periods of 20, 50, and 100 years. The rapid change in climate signal resulting from the 20-year period is not visible in length, however it can be observed in volume change. The lag of length changes is well illustrated.*

The strong almost to vertical change in length for the 100-year period (green line in Figure 19) is caused by a tributary glacier, Tschingelfirn, which reaches the flow line of Brunnifirn and thus is counted as the front of Brunnifirn by the model (ice furthest along the flow line is counted as maximum length). Note how this influence by Tschingelfirn is only visible in the second length maximum at 200 years, indicating that ice buildup during a first ELA minimum is required for the tributary glacier to reach the valley ground (and thus the flow line of Brunnifirn) during a second advance.

The experiments with today's glacier extent and the extent just flowing over the plain yielded interesting information about how the change in bed and ice geometry due to the glacier flowing into the steep section influence volume and length change. The larger glacier

(ELA0 = 2720 m a.s.l., Figure 43) which initially flows over the plain cannot reach its initial length again with a 20-year period ELA forcing It reaches a repeating length change cycle after ca 250 years, and, with a 500 m difference between maximal and minimal length in the case of a 100-year period forcing, fluctuates strongly. The smaller glacier (ELA0 = 2730 m a.s.l., Figure 44) generally increases its volume over the 500 years for all three sinus forcing periods. In the case rapid changes in ELA (20-year sinus period) the glacier does not retreat as strongly between advances and builds up enough ice to flow over the edge of the plain after ca 250 years. In the case of the slow 100-year ELA sinus period, the tongue retreats too much during the first ELA maximum to advance over the edge of the plain in the 500 years that were modeled.

3.4.4 Sensitivity testing

The period from 1500–2020 CE was used to test the sensitivity of the reference ELA (ELA0) and the temperature-ELA conversion factor ($\mathrm{ELA_{fc}}$). The resulting ideal ELA0 and $\mathrm{ELA_{fc}}$ are then applied to all temperature-proxy-based transient modeling experiments. The period from 1500–2020 CE proved to be ideal for sensitivity testing, as it is just long enough to see the influence of the starting glacier surface geometry. Also, the length measurements by the Swiss Glacier Monitoring Network (GLAMOS, 2022) and lengths derived from mapping on aerial images (images from swisstopo, 2023) are useful constraints to evaluate if the modeled extents lie within a reasonable range. However, these constraints come with uncertainties: for the GLAMOS measurements, it is unclear where exactly the absolute length of the glacier was at a given time, as only annual length changes were observed instead of points. The details of the reference position are unknown. For example, measurements could have been taken away from the center of the glacier, i.e., the flow line, and the reference point for measurements could have changed over time. Also, as the aerial image from 1979 CE shows, a big piece of dead ice separated from the tongue before (before 1979 CE, however unknown year of separation, as the last image analyzed is from 1958 CE, where the tongue is connected). If such dead ice should be counted as part of the glacier may be a question of definition. In the case of the remote mapping in this thesis, it was counted as part of the glacier for better comparability with model outputs, as the model counts the furthest grid cell along the flow line that contains ice as the glacier length.

To test sensitivity and evaluate a fixed reference ELA (ELA0) and the temperature-ELA conversion factor $\mathrm{ELA_{fc}}$, three different starting glacier surface geometries were used to model the period from 1500–2020 CE. ELA0 and $\mathrm{ELA_{fc}}$ were the same for each run, and the results were compared to extent of the LIA moraine and the documented retreat by GLAMOS and the remote mapping (Figure 20). Three reference ELAs were tested based on steady state modeling results: 2730 (extent filling the plain), 2720 (extent flowing over the plain), and 2700 m a.s.l. (extent almost reaching the upper moraine cluster). Three ELA conversion factors were tested, accordingly: 130 m $°\mathrm{C}^{-1}$, 120 m $°\mathrm{C}^{-1}$, and 100 m $°\mathrm{C}^{-1}$. Not all factors were tested for each ELA0, as results of the combination ELA0 = 2720 m a.s.l. and 130 m $°\mathrm{C}^{-1}$ are convincing and fit the above-mentioned criteria. The following table is a short summary of the reasons for exclusion of the factor combinations displayed in the appendix (Figure 45; Figure 46; Figure 47; Figure 48; Figure 49).

Table 13: *Short summary of parameter combinations and the reasons why they were not used for further modeling. For details see Figures 45–49 in the appendix.*

ELA0 (m a.s.l.)	$\mathrm{ELA_{fc}}$ (m °$\mathrm{C^{-1}}$)	Over-/underestimations
2700	120	Glacier is too large for LIA max and during 1950–2020 retreat.
2720	120	Glacier does not reach LIA moraine.
2730	120	Glacier does not reach LIA moraine.
2730	130	Glacier is too large for LIA max and during 1950–2020 retreat.
2720	100	Glacier does not reach LIA moraine.

The retreat recorded by GLAMOS and in the aerial images could not be exactly matched with any parameter combination and the applied summer temperature forcing (Casty et al., 2005a; MeteoSwiss, 2023). However, the LIA maximum extent confined by the LIA moraine complex could be matched, and a clear first peak with a subsequent retreat and final readvance as well as a short stagnation of retreat during the 1980s could be modeled (Figure 20).

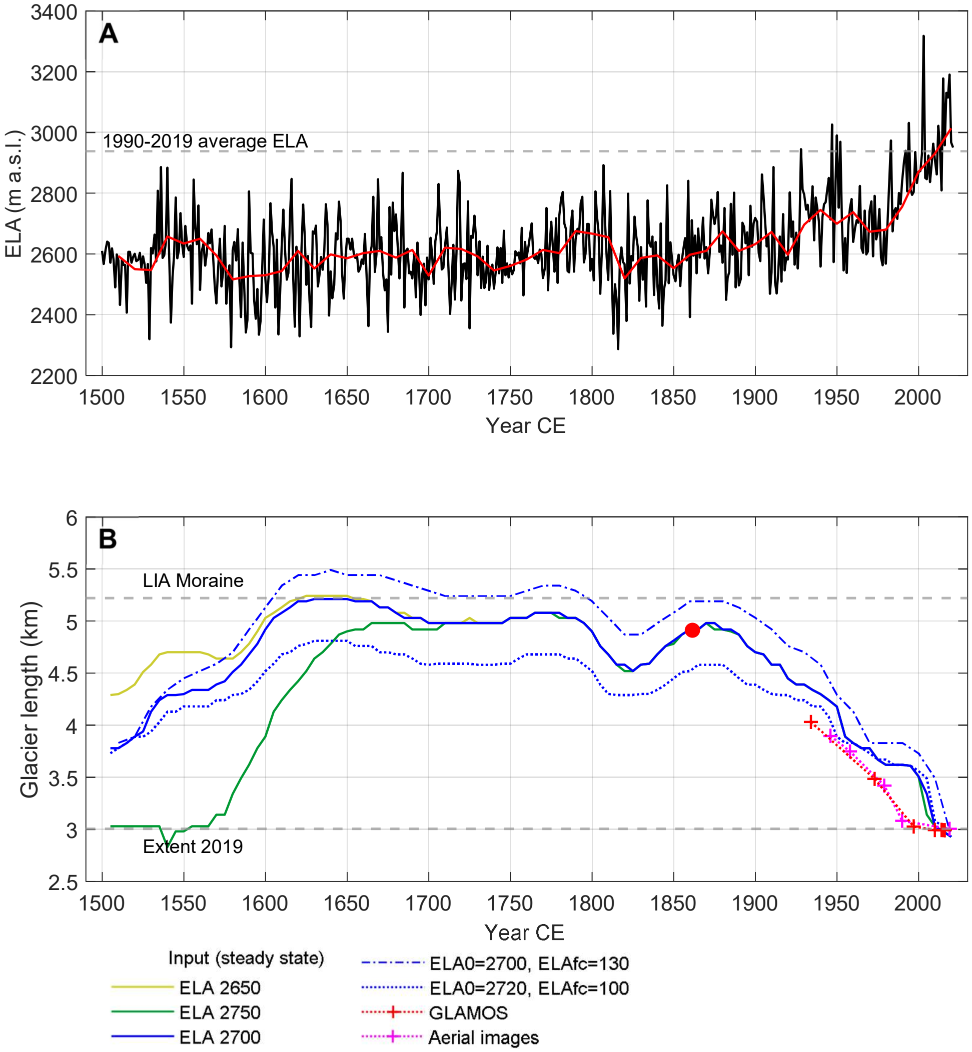

Figure 20: *A) ELA forcing for the modeling of 1500–2020 CE with 10-year means (red line), derived from the summer temperature curve* (Casty et al., 2005a; MeteoSwiss, 2023). *B) Sensitivity experiment for 1500–2020 CE length evolution of Brunnifirn, using three different starting glacier surface steady state geometries (yellow, blue, and green lines). Length measurements (GLAMOS and aerial images) are displayed for comparison, and the gray dotted lines show today's extent and the possible LIA maximum extent. The red dot marks the glacier length on the Siegfried map (data content from 1859 CE, according to swisstopo, 2023).*

After ca 1700 CE, the length curves overlap (bold lines in Figure 20), meaning that the starting glacier surface geometry signal is not visible anymore, except for some peaks. The two most deviating length evolutions resulting from other parameter combinations are displayed as blue dotted lines. The two deviating length evolutions stemming from different parameter configurations than the ones used for the main length reconstruction (blue solid line in Figure 20) either overshoot the LIA moraine or are too short which would not allow for deposition of the clear moraine found in the field. The ice extent recorded from the Siegfried map corresponds to 1859 CE (swisstopo, 2023a) and fits the modeled extent, but has to be viewed with caution, as the exact circumstances of mapping remain unclear. The retreat encountered in ca the last 80 years seems to be hard to match with the numerical model, probably because it occurs rapidly over the complex bed geometry. The result of the modeling for the year 2020 is a slight underestimation of Brunnifirn, Glatscher da Strem and especially Staldenfirn however are larger than their actual 2019 extents (Figure 24). As mentioned in chapter 3.4.1, today's glacier extent cannot be recreated in steady state either. Discrepancies may be caused by debris cover on the southern part of the plain, i.e., on the north slope of the southern ridge, or by precipitation feedback.

3.4.5 1500–2020 CE modeling

A maximum extent is reached in 1630 CE and lasts for 20 years (Figure 21, overview map: Figure 25). The model produces a slightly larger extent than the moraine ridge. The last maximum extent does not match the ca 1630 maximum but matches the extent displayed on the Siegfried map in dimension and fits for the time when measurements for that map were taken.

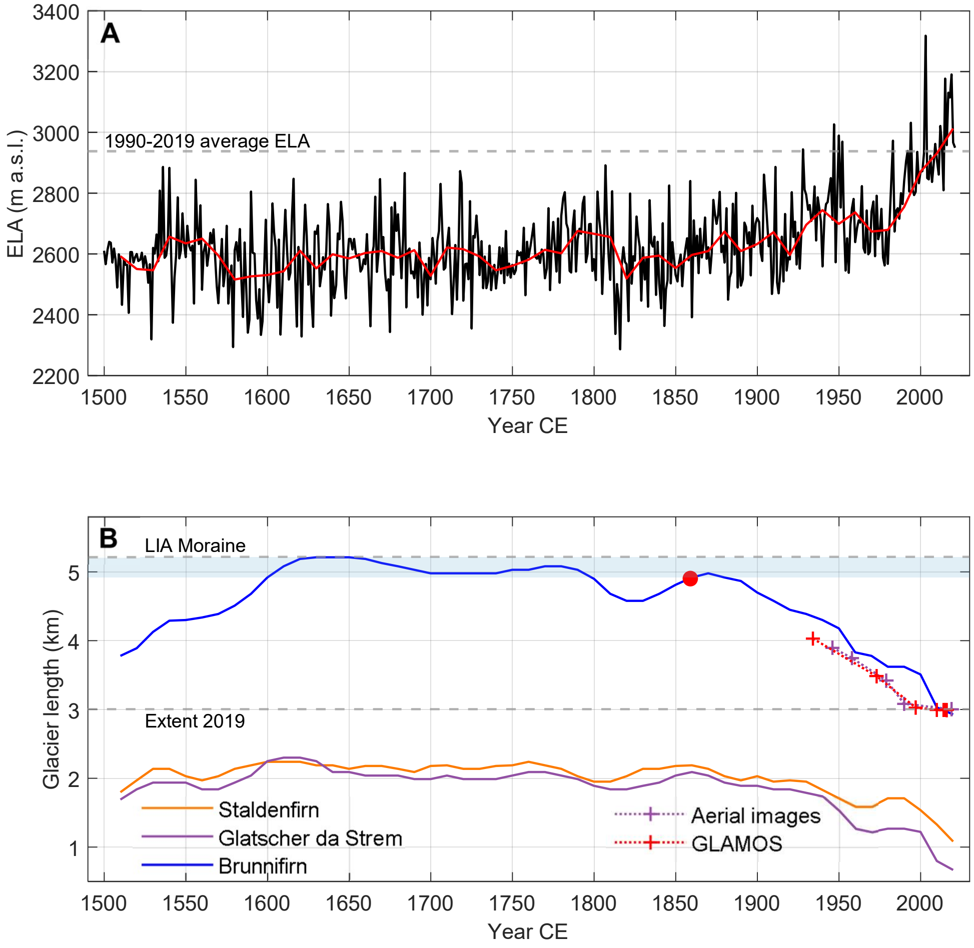

Figure 21: *A) ELA forcing for the modeling of 1500–2020 CE with 10-year means (red line), derived from the summer temperature curve* (Casty et al., 2005a; MeteoSwiss, 2023). *B) LIA fluctuations of Brunnifirn, Staldenfirn and Glatscher da Strem with the same ELA forcing (parameter configuration: ELA0 = 2720, ELA_{fc} = 130). The starting glacier surface geometry is a 2720 m a.s.l. ELA steady state. The blue box shows a range within Brunnifirn fluctuated over ca 250 years during the LIA period. The dashed gray lines show the 2019 extent of Brunnifirn and the position of the LIA moraine. The red dot marks the glacier length on the Siegfried map (data content from 1859 CE, according to swisstopo, 2023). Length measurements (GLAMOS and aerial images) are displayed for comparison.*

In comparison with the moraines, the modeling outputs seem plausible: they complete the hypothetical extent proposed by the moraines and ridges, also matching lateral moraines and supposed moraine ridges, as well as *moraine remnants* (Figure 22).

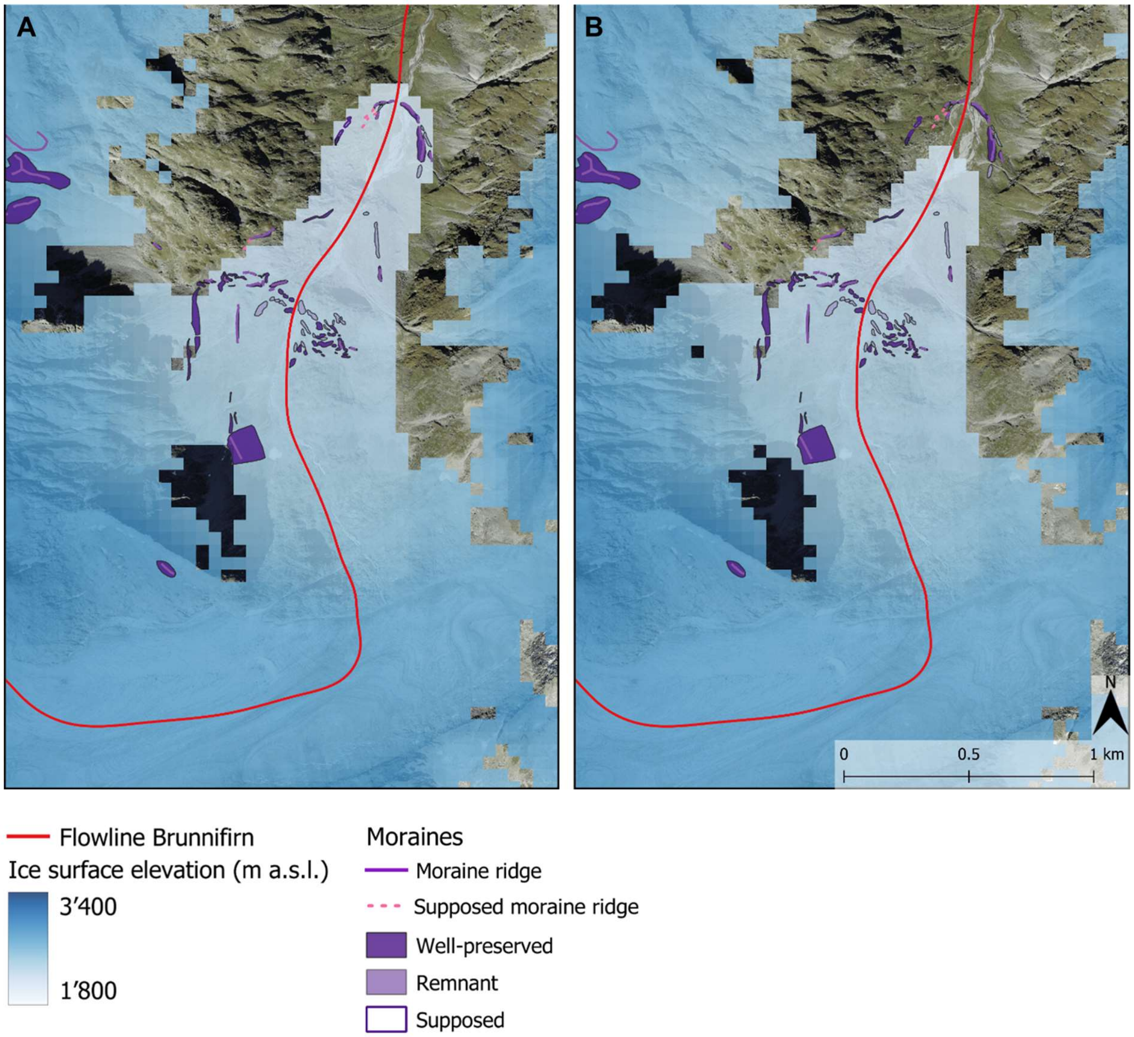

Figure 22: *A) Brunnifirn LIA maximum modeling extent maintained from 1630–1650 CE. B) Modeling output of last LIA maximum reached ca 1870. Not only the LIA maximum moraine complex is matched, but also lateral moraines fit well with the modeled glacier extent. Also, the ice margins complement the supposed moraine ridges and moraine remnants.*

Staldenfirn and Glatscher da Strem are much smaller and flow on steeper bed geometries than Brunnifirn, resulting in faster responses to climate signals. After an initial clear advance until ca 1600 CE, they maintain their sizes until a short retreat around 1800 CE, to then quickly readvance and finally retreat to the uppermost parts of Oberalpstock (Figure 21). Staldenfirn retreats well before Glatscher da Strem around 1800 CE, which points to a faster response time of the former. Both small glaciers readvance for a few years after 1980 CE, whereas Brunnifirn stagnates without readvancing before continuing to retreat.

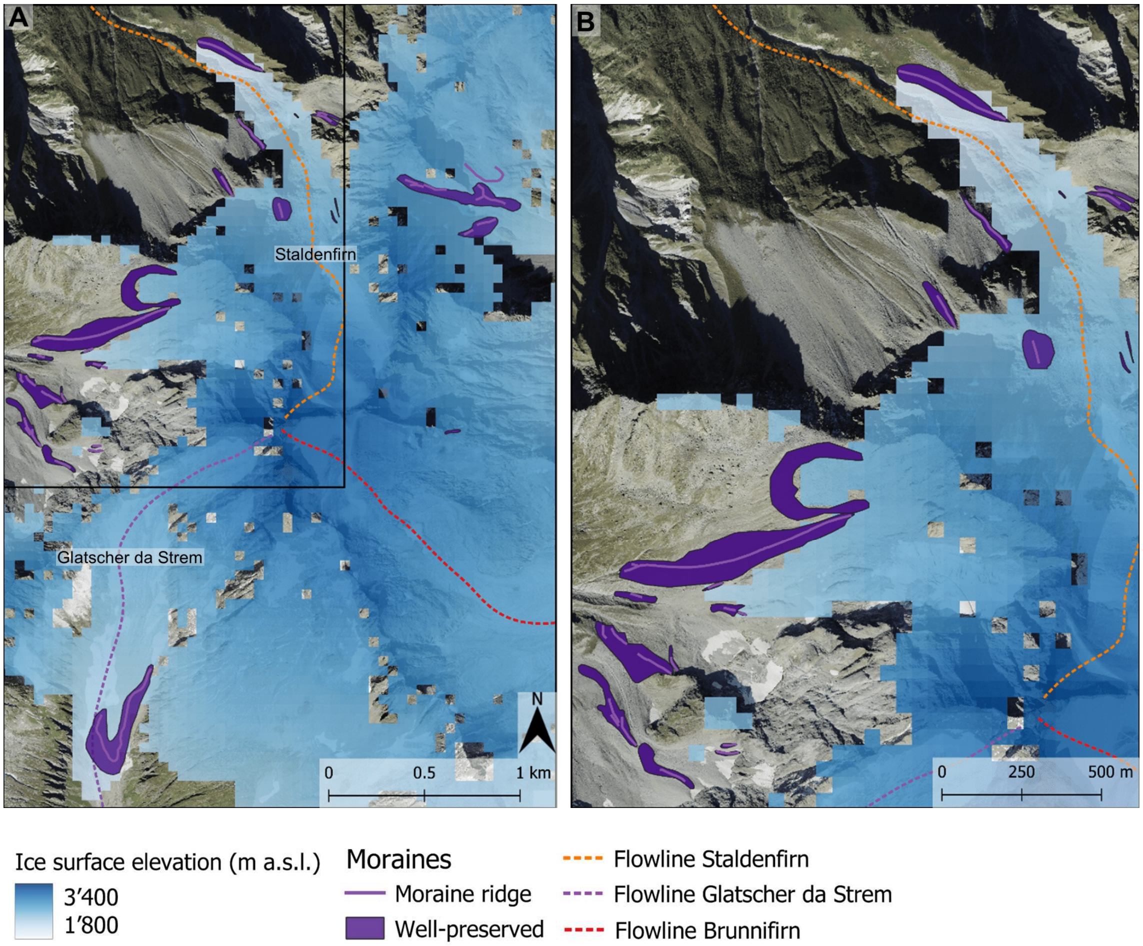

Figure 23: *A) Maximum extents of Staldenfirn and Glatscher da Strem during the modeling of 1500–2020 CE, output for 1610 CE. Bächenfirn, a glacier not quantified during modeling, flows towards the west. Note how ice extent match the mapped moraines. B) Detail inset for Staldenfirn flowing towards north and Bächenfirn flowing towards west, both ice extents matching large lateral moraines. Background map: swisstopo (2023).*

Staldenfirn and Glatscher da Strem reach their LIA maximum extents around 1610, about 20 years before Brunnifirn. Both modeled maximum extents fit well with moraines documented during the remote mapping. For another small glacier, Bächenfirn, originating below the peak of Oberalpstock at ca 2900 m a.s.l., and flowing westwards, the modeled ice surface fits between two lateral moraines and reaches a large frontal moraine. These three smaller glaciers matching large moraines which are well-conserved (i.e., not strongly weathered, indicating recent deposition) shows how the model seems to be applicable to glaciers with different bed geometries and orientations, which suggest robustness of model application (see Figure 23).

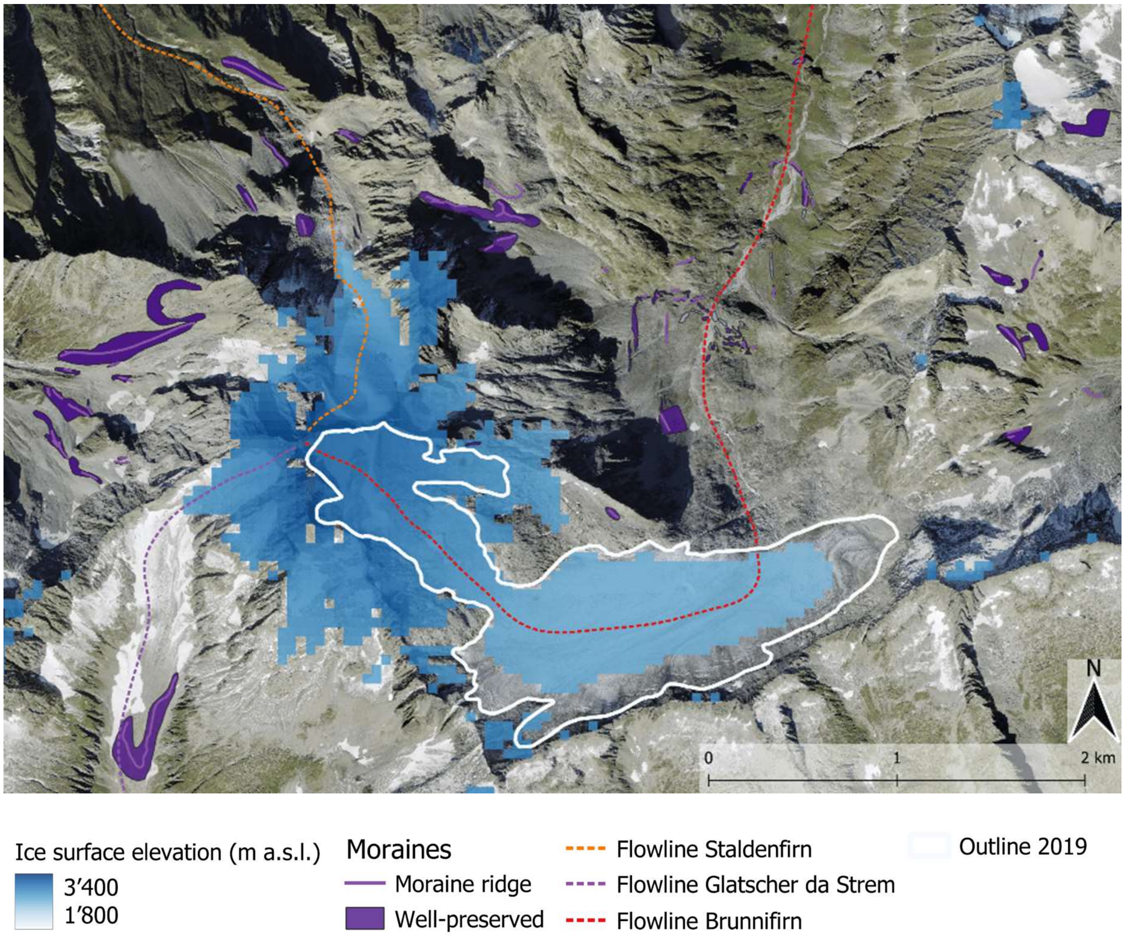

Figure 24: *Final output of the modeling for the year 2020, compared with the glacier outline 2019. Note how the south-eastern part of the plain is underrepresented by the model, where the glacier is debris-covered. Background map: swisstopo (2023).*

The final year of the 1500–2020 CE modeling period is a slight underestimation of the actual glacier extent in that year (see Figure 24). On the other hand, on the south-western flank of Oberalpstock, no ice is seen in the aerial image from 2019, however the model output shows ice.

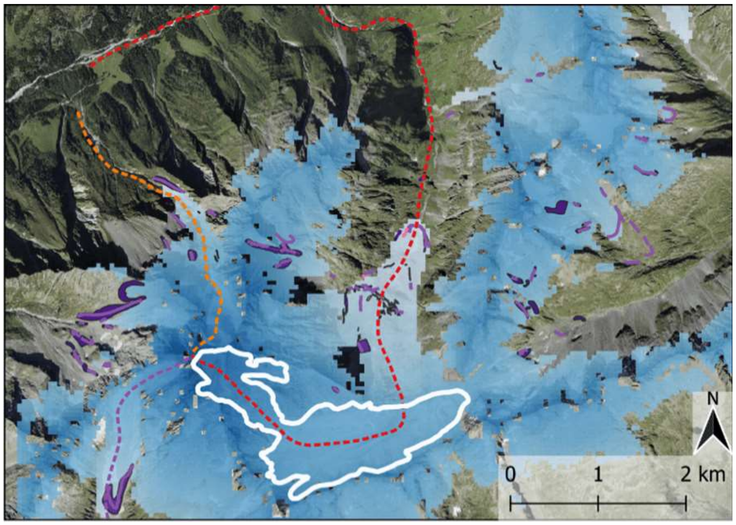

Figure 25: *LIA maximum extent of Brunnifirn based on modeling (output for 1640). Note how moraines in Val Cavardiras to the east are matched by the modeled ice extent. Background map: swisstopo (2023).*

3.4.6 Holocene modeling

In a second part of modeling past fluctuations, the focus was set on the Holocene from 9 ka until today. Based on the sensitivity experiments for the modeling of 1500–2020 CE, the same parameters were set for Holocene modeling (ELA0 = 2720 m a.s.l., ELA_{fc} = 130 m $°C^{-1}$). The temperature reconstructions from Milandre cave (Affolter et al., 2019b) and from Greenland ice cores (Alley, 2004) were used as temperature forcing to examine how the two temperature reconstructions produce different glacier length evolutions.

The 1500–2020 CE temperature reconstruction (Casty et al., 2005a; MeteoSwiss, 2023) was applied from 1500 CE onwards (Figure 28). To investigate the glacier size during the time for which the archeological artifacts are dated, the period from 9 to 7.5 ka is displayed in detail (Figure 26). The results of the Holocene modeling show that trends of both forcings are the same and cold and warm peaks are represented in both evolutions. However, the glacier extent produced by the GISP2 data is significantly smaller than the one based on the Milandre data for most of the modeled period, except for short events around 1.2 and 4.8 ka (see Figure 28).

Interpolation between temperature data points in the forcing file was set as nearest neighbor for the whole period from 9 ka onwards. To assess the influence of the interpolation method, the period from 9 to 7.5 ka was also modeled using linear interpolation between temperature data points (Figure 50). Results are similar, but length variations are smoother. However, response times to climate signals are better visible thanks to the clear peaks of linear interpolation, in contrast to the plateau-like shape of the nearest neighbor interpolation. The temperature minimum of the GISP2 reconstruction is reached shortly before 8.2 ka, producing a length maximum of the glacier shortly after 8.2 ka. The temperature minimum of the

Milandre reconstruction on the other hand is reached at ca 8.15 ka, producing a glacier length maximum after 8.1 ka. The lag of glacier length maximum behind temperature minimum in case of the Milandre temperatures is about 50 years, whereas it is less than 50 years for the case of the GISP2 temperatures. This difference in response time can be explained by the glacier size: as the GISP2 temperature minimum is warmer than the one based on the Milandre reconstruction, the glacier modeled with the former forcing is smaller and can thus react faster to climatic change.

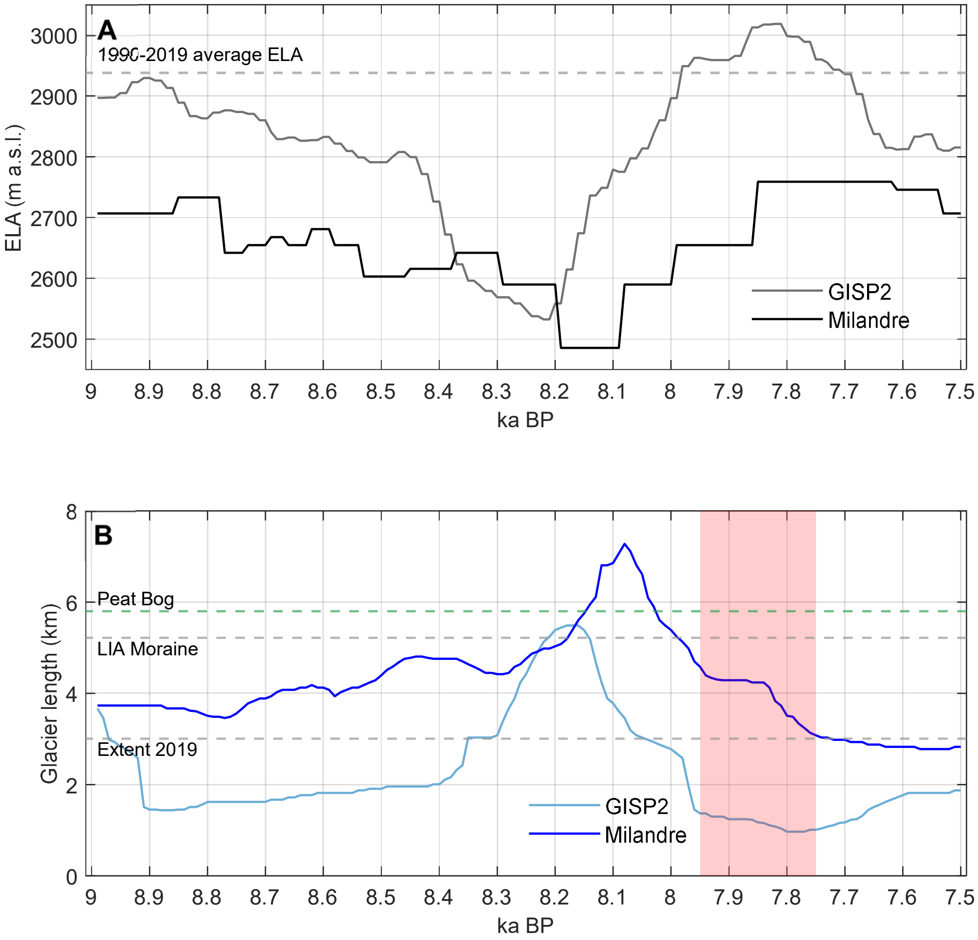

Figure 26: *Holocene modeling around the period the archeological artifacts are dated for (red box in plot B). Modeling was started before the cold interval around 8.2 ka to eliminate bias of the starting glacier surface geometry (steady state for 2700 m a.s.l. ELA). A) ELAs calculated for GISP2 and Milandre temperature reconstructions (ELA0 = 2720, ELA_{fc} = 130), with nearest neighbor interpolation between data points. B) Brunnifirn length modeled from the two different ELA calculations. The gray dotted lines show known glacier extents as reference, the green dotted line shows the position of the peat bog which was radiocarbon age dated to ca 3.8–3.5 ka BP.*

The ages assigned to the archeological artifacts come after a retreat from a large glacier extent for both temperature forcing options. In the case of the Milandre forcing however, the glacier exceeds the LIA moraine complex by ca 2 kilometers and flows together with a tributary glacier, Tschingelfirn, which reaches the main valley from an eastern slope during cold climate. In Figure 26 the issue of measured glacier length by the model versus actual glacier length (as described for Figure 19) was corrected manually, the displayed lengths therefore represent the actual glacier extent. From the moment when Brunnifirn connects with Tschingelfirn, both tongues are counted as one and the point located furthest down valley is measured as maximal length. During the retreat, from the moment when the two glaciers disconnect, the tongue of Tschingelfirn remaining in the valley is not counted to Brunnifirn anymore.

During the period which the archeological artifacts are dated for, the two glacier extents are quite different: for the case of Milandre forcing, the glacier is still on a retreat from an extent similar to the LIA maximum, and only becomes as small as it is in 2019 CE around 7.75 ka. The glacier modeled with GISP2 forcing on the other hand is smaller than today for the entire period the artifacts are dated for.

The temperature minimum recorded in both reconstructions around 8.2 ka BP is the clear minimum of the modeled period from 9 ka until today. During this glacier maximum, the peat bog with a radiocarbon age of ca 3.8 to 3.5 ka BP is overridden by the glacier produced with Milandre forcing from 8.15 ka on for ca 100 years. The GISP2 forced glacier extent does not reach the peat bog during this peak. This advance of the glacier produced with Milandre forcing is the only advance throughout the modeled period from 9 ka until today that is large enough to override the peat bog. Drilling a deeper core from the peat bog to also constrain the age of the deepest layers would allow to confirm the modeling: if the oldest layers would date back to ca 8 ka, this would confirm that the GISP2 temperatures are too warm, and that the Milandre forcing is representative for this case. This hypothesis would however require thorough testing.

The Holocene modeling includes a future evolution: the ELA of the last modeled year (2021 CE, ELA = 2949.85 m a.s.l.) was kept constant until the end of the century. This is however not a realistic approach to constrain future evolution, as at least a temperature average over 30 years is required to model the steady state for current climate. This approach and future modeling including RCP simulations is documented in more detail in chapter 3.4.7.

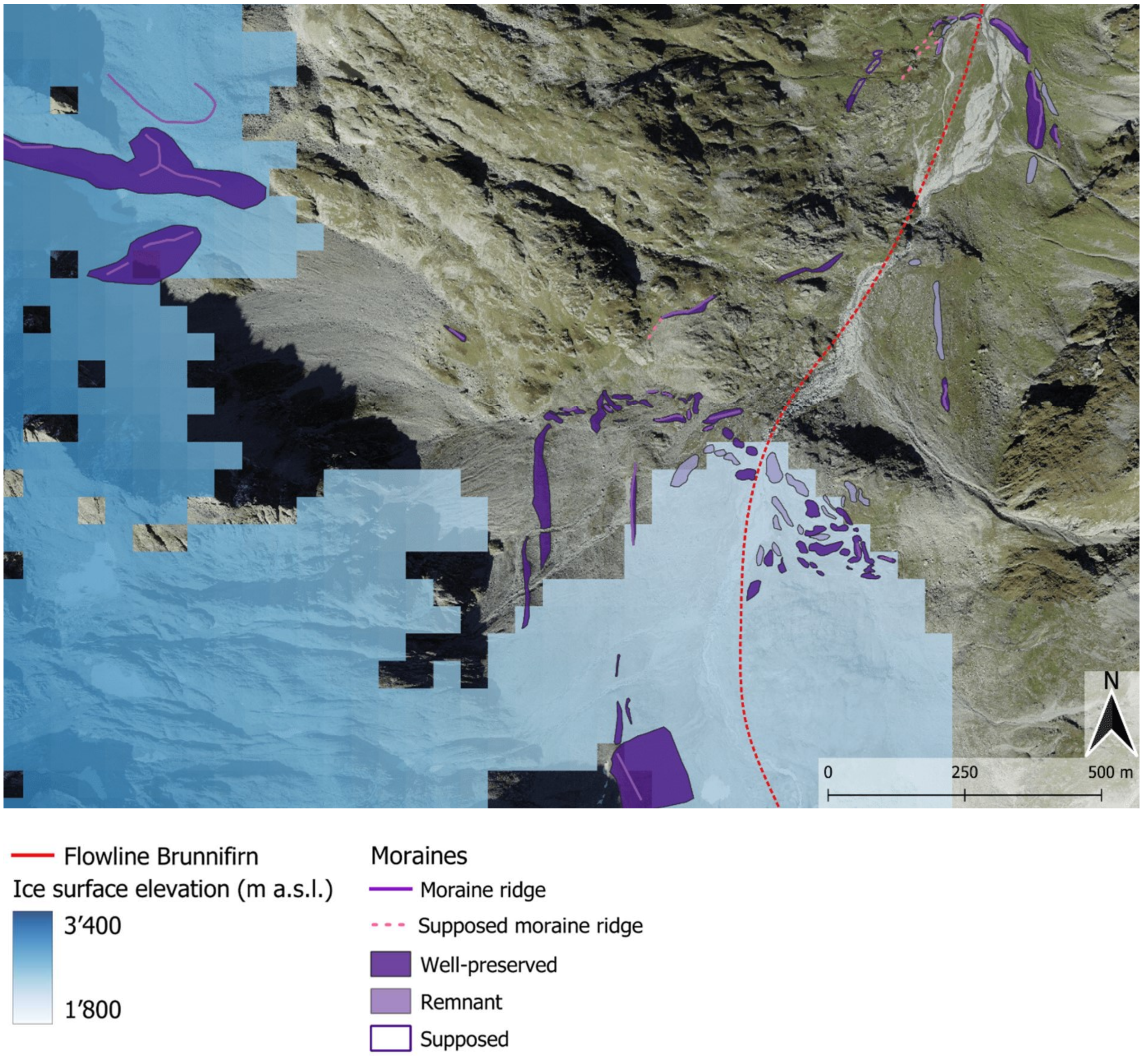

Figure 27: *Model output reaching the upper moraine cluster (steady state ELA = 2650 m a.s.l.), displayed with moraines mapped during field and remote mapping (no differentiation between mapping method for better readability). This extent is reached multiple times throughout the Holocene, especially for the Milandre-forced glacier (Figure 28).*

Throughout the Milandre-forced reconstruction, Brunnifirn often reached an extent of the upper moraine cluster (see grey dotted line in Figure 28). This may have allowed for deposition of a high volume of sediment, and thus the formation of numerous hummocky moraines. An exemplary extent is displayed in Figure 27.

The GISP2 forcing only causes the glacier to reach similar extents around 4.5 ka. Overall, the glacier modeled with the GISP2 forcing is smaller than the 2019 extent for the whole modeled period except for four advances: after 8.5 ka, shortly before 4.5 ka, just before 1 ka, and during the LIA after 0.5 ka. The glacier respectively reaches extents similar to those during the LIA, except for the advance before 4.5, where it only reaches the upper moraine cluster (Figure 28).

The Milandre forcing produces a different outcome: the glacier fluctuates around the upper moraine cluster for most of the modeled period. It strongly exceeds the LIA maximum before 8 ka, and then retreats to an extent smaller than 2019 from ca 7.5–6.5 ka. After this retreat, it advances further than the upper moraine cluster around 6 ka, to then fluctuate around that extent, clearly exceeding it three times before the LIA: around 4.5 ka, after 2.5 ka, and after 2 ka (*Figure 28*). The retreat of the last century is excluded from these statements.

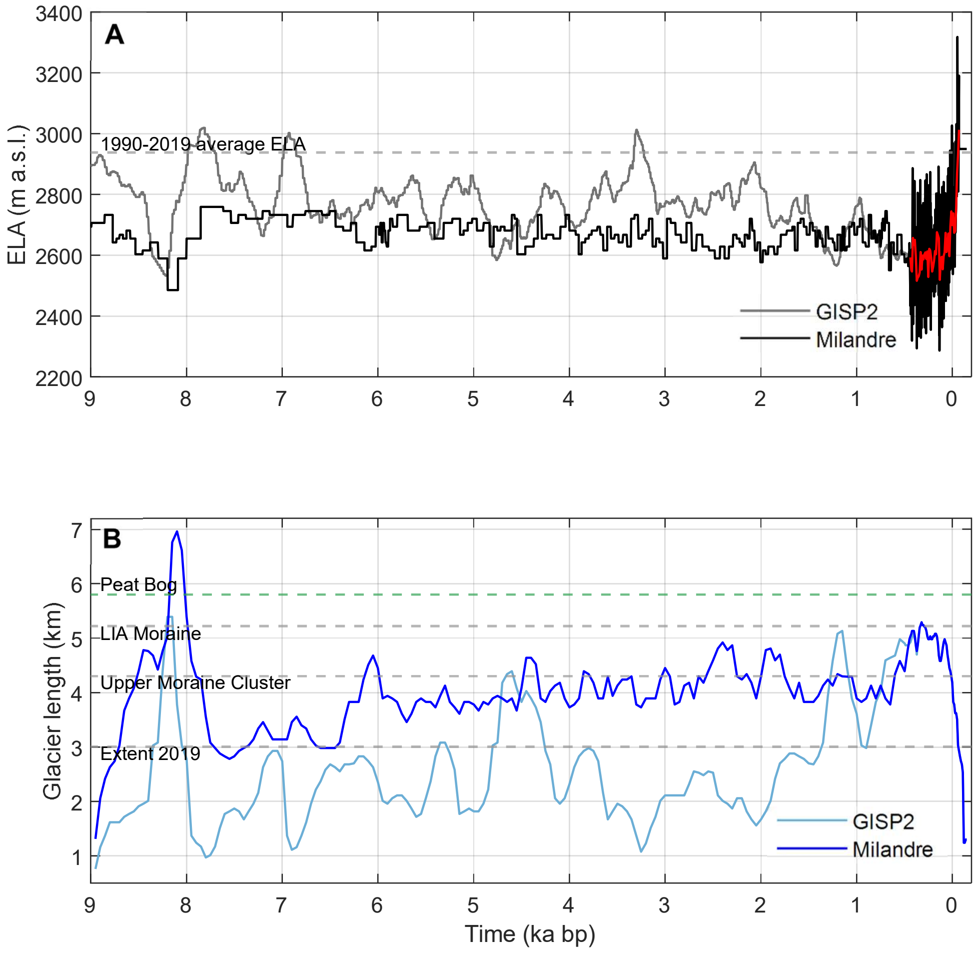

Figure 28: *Holocene modeling for the whole analyzed period from 9 ka until today, including steady ELA from the year 2021 CE onwards until 2100 CE. Starting geometry: no ice. A) ELAs calculated for GISP2 and Milandre temperature reconstructions (ELA0 = 2720,* $ELA_{fc} = 130$*), with nearest neighbor interpolation between data points. LIA temperature reconstruction (Casty et al., 2005a; MeteoSwiss, 2023) from 1500 CE onwards, with 10-year means (red line). B) Brunnifirn length modeled from the two different ELA calculations. The gray dotted lines show known glacier extents as reference, the green dotted line shows the position of the peat bog which was radiocarbon age dated to ca 3.8–3.5 ka.*

3.4.7 Future modeling

As a simple future simulation, climate was kept steady in a first step. The average temperatures from 1990–2019 (MeteoSwiss, 2023) are kept constant from 2020 onwards. The thirty years represent the current average climate, and the corresponding glacier output therefore is a steady state to this average climate (Figure 29). Compared to the Milandre Holocene modeling (Figure 28), the glacier reaches an unprecedented minimum extent. On the contrary, the GISP2 Holocene modeling extents are similarly small three times throughout the modeled period: after 8 ka, after 7 ka, and around 3.2 ka.

The almost vertical length change visible in Figure 29 after 2050 results from the disappearance of a large piece of dead ice in the plain: the current main body of Brunnifirn disconnects from the rest of the glacier between 2030 and 2040 CE, practically remaining as dead ice, as it has no more accumulation area. In ca 2060 CE, this large piece of dead ice completely disappears.

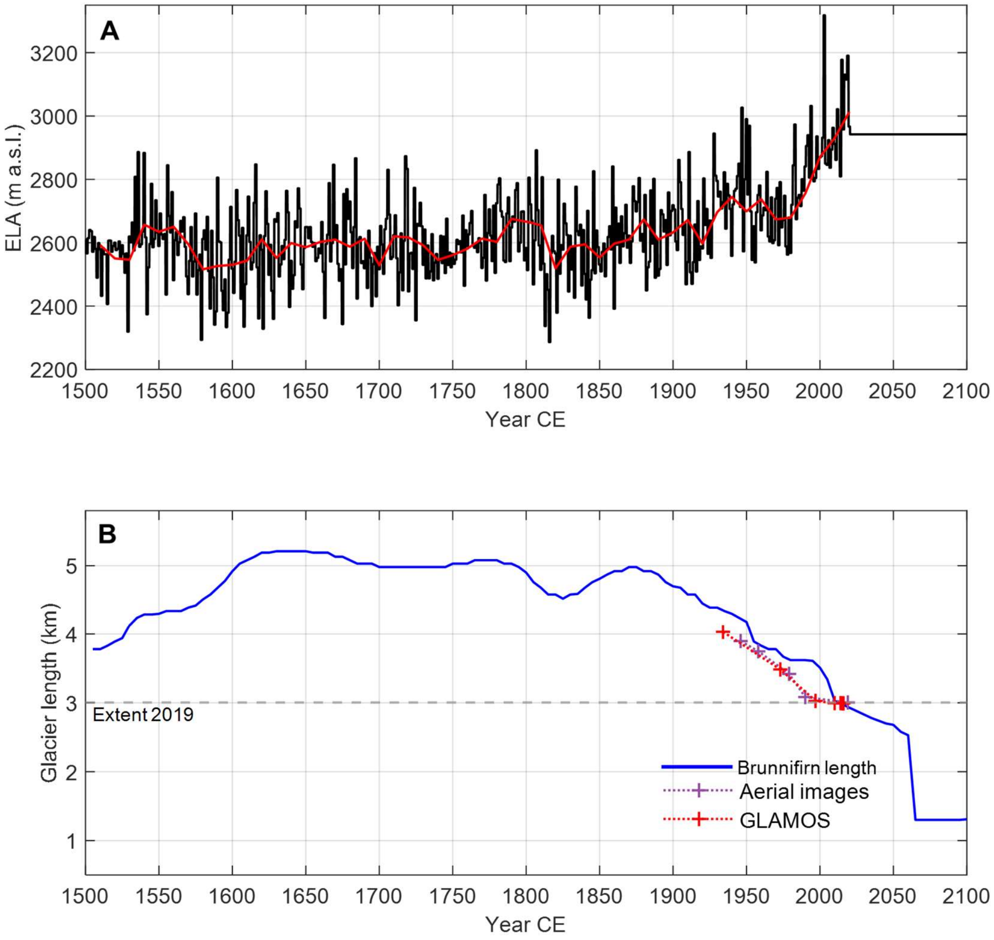

Figure 29: *Future evolution of Brunnifirn for constant climate from 2020 onwards (2942 m a.s.l. = average ELA from 1990–2019). A) ELA with 10-year means (red line). Evolution from 1500–2019 CE modeling with parameter configuration of: ELA0 = 2720,* $ELA_{fc} = 130$*. B) Length evolution compared with length measurements (GLAMOS and aerial images). The length reached after 1950 when no more change occurs represents a steady state to the average climate from 1990–2019.*

Similar results stem from the four simulations (CH2018, 2018) used for transient future evolution. For all three RCPs, impressive retreat occurs, and the part of the glacier in the plain disconnects from the steep upper section (Figure 30). This possible future evolution is supported by what can be observed today: as visible in the 2019 aerial images (Figure 14), the transition from the upper steep section to the wide flat part in the plain is already very narrow.

The four simulations used for the future modeling all produced similar results. They fit well for the transition from the modeling of 1500–2020 CE to onset of future simulation in 1981 CE and suit the GLAMOS and aerial image length measurements (see Figure 30). The fit to the modeling of 1500–2020 CE for the overlapping period shows that the chosen offset for the future temperatures works well. To exemplify extents, the results of based on the DMI-HIRHAM_ECEARTH simulation are displayed here. The results of the other simulations are displayed in the appendix.

For all three RCPs of each simulation, the glacier retreats to an extent smaller than 1 km until the end of the century, as visible in the example of the DMI-HIRHAM_ECEARTH simulation (Figure 30). For the RCP2.6, the final lengths by 2099 range from 0.5 to 0.8 km, depending on the simulation. For the RCP4.5, it disappears completely for the SMHI-RCA_ECEARTH simulation. In the other simulations it stabilizes around 0.4 km length. It disappears completely for the RCP8.5 for all four simulations.

The outcome of this future analysis is that RCP2.6 and RCP4.5 simulations allow for at least a small glacier to remain until the end of the century, depending on the simulation. For the RCP8.5 simulations Brunnifirn will completely disappear by the end of the century.

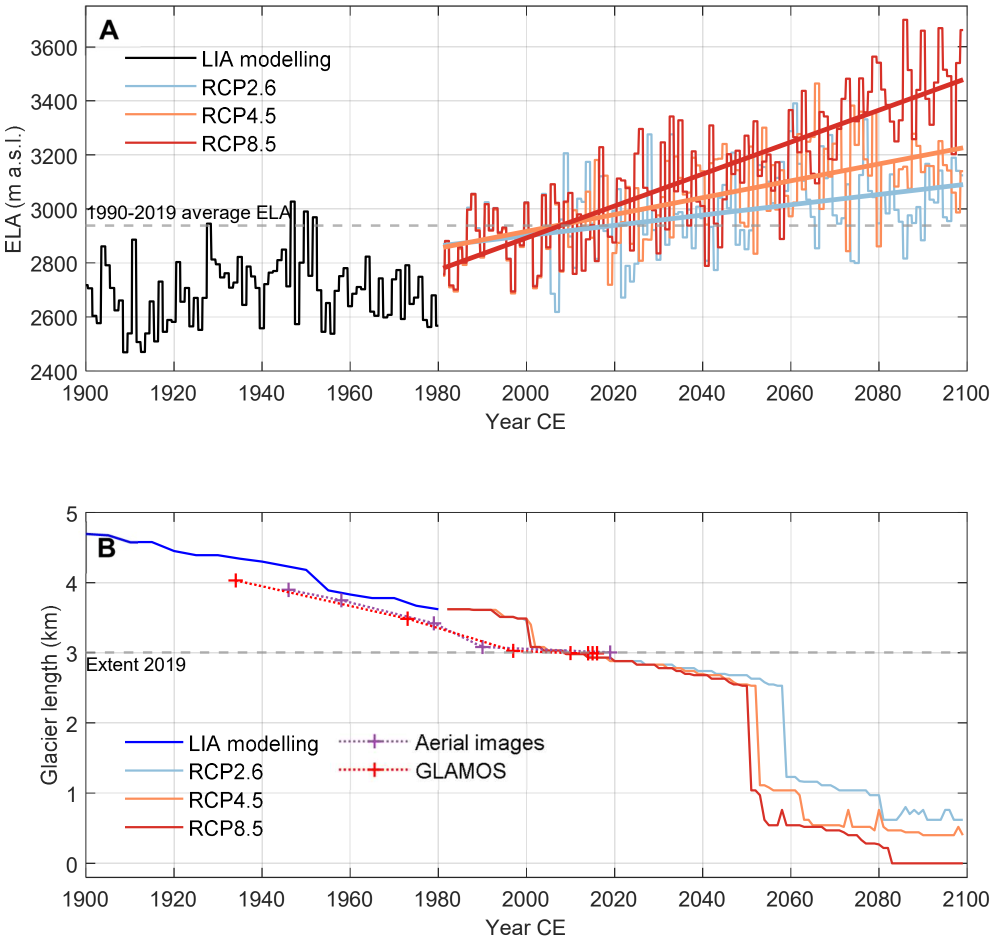

Figure 30: *Future evolution of Brunnifirn from 1981–2099 CE for three RCPs (CH2018 simulation DMI-HIRHAM_ECEARTH), with result 1980 CE result of the 1500–2020 CE modeling. A) The bold lines are trends for the three RCPs. B) The almost vertical length change before 2060 CE marks the disappearance of a large dead ice body that remains in the plain. The steep upper part of the glacier however disconnects from the part in the plain already around 2030–2040 CE.*

To illustrate what glacier extents the simulations produce, hypothetical ice extents in 2050 CE of three RCPs from the DMI-HIRHAM_ECEARTH simulation are displayed in Figure 31. The disconnected part of the glacier in the plain remains on the flow line, thus producing the vertical line in the length evolution (Figure 30). Staldenfirn and Glatscher da Strem still remain in 2050 CE for the RCP2.6, thanks to their origins just below the peak of Oberalpstock. For the RCP8.5, only the north facing Staldenfirn remains in 2050 CE. The model still overestimates some parts of the steeper sections, as there is ice in 2050 CE at places where there already today is no ice left.

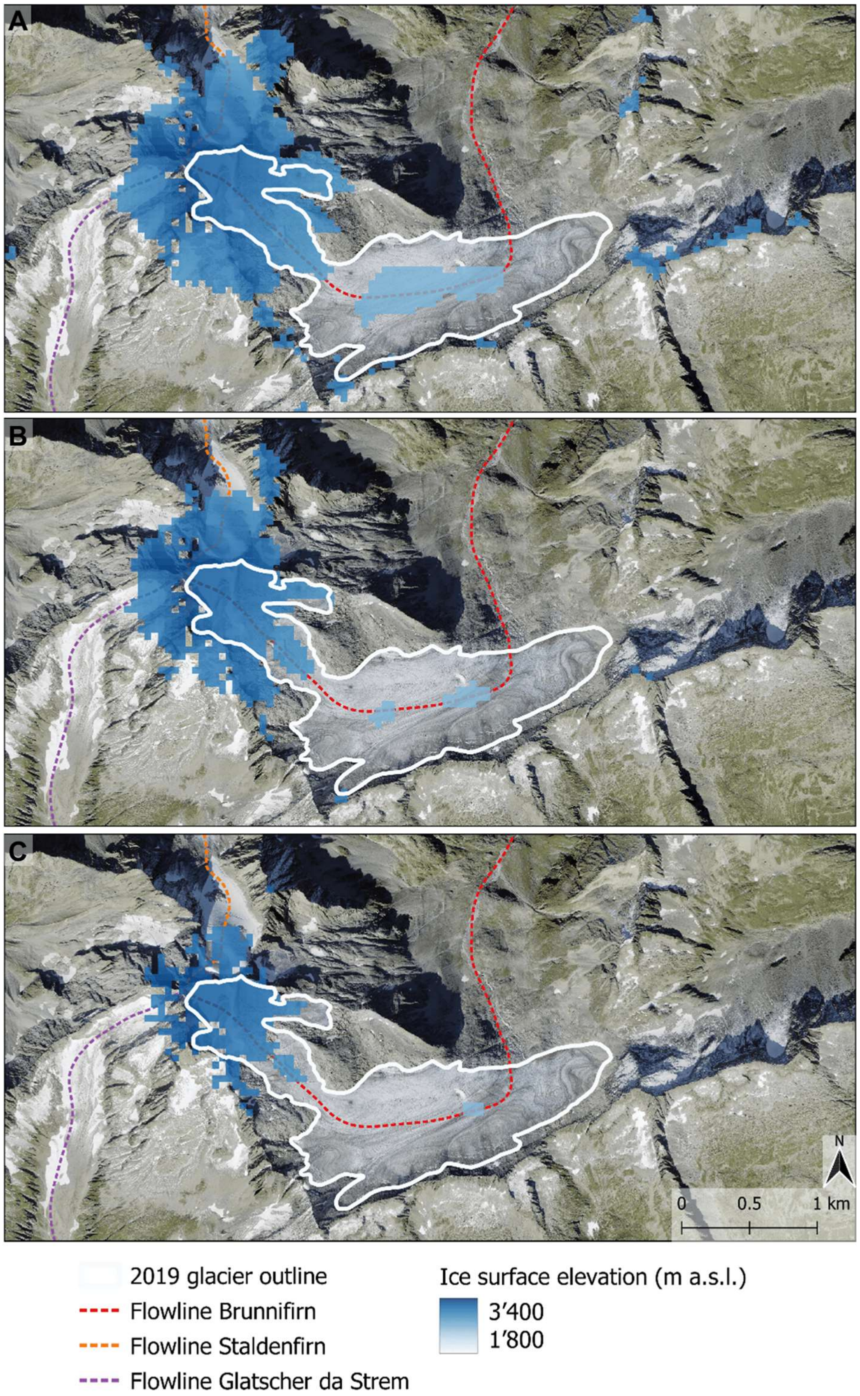

Figure 31: *Hypothetical ice surface output for 2050 CE based on the DMI-HIRHAM_ECEARTH simulation. A) RCP2.6. B) RCP4.5. C) RCP8.5. Note the ice disconnected from the steep section in the center of the plain, which is counted as maximal glacier length as it is located on the flow line, causing a false length measurement. Background map: swisstopo (2023).*

4 Discussion

The results of the geomorphological mapping and numerical modeling listed in the previous chapter need to be evaluated and contextualized. To improve readability and at the same time synthesize and integrate results, the discussion is structured according to the research questions. Chapter 4.1 treats research questions 1a) and 1b), focusing on the landforms found in the forefield of Brunnifirn and what glacier extents can be identified based on these landforms. The landforms indicating past glacier extents, and the corresponding fluctuation are discussed in the context of modeling, radiocarbon dating, and the historical map. Research questions 1c) and 2a) are considered in chapter 4.2, in which the inferred ELAs from mapping are related to the modeled steady state ELAs. In chapter 4.3 research question 2b) is answered, where the transient glacier response to a fluctuating climate is discussed. Modeling parameters, sinus and step change experiments, response time and ELA sensitivity are also integrated in this synthesis. Finally, chapter 4.4 revisits research questions 2c) and 2d), assessing glacier fluctuations modeled with the different climate reconstructions of the past and the future projections. The influence of the climate data on modeling is considered as well. The research questions are listed at the beginning of the corresponding chapter.

4.1 Mapped landforms and inferred extents of Brunnifirn

Research questions:

- 1a) What landforms can be found in the forefield of Brunnifirn?
- 1b) What glacier extents can be identified based on the mapped landforms?

Landforms and their relevance

The iterative process of field and remote mapping allowed for a continuous reanalysis of landforms which were found in either of the approaches. Areas which were overlooked with one method were highlighted by the other, and vice versa. Integrating the mapping results from the different methods thus increased the level of detail and quantity of mapped landforms. Especially landforms mapped with both methods independently increase the robustness of the approach (Figure 15).

Nevertheless, both approaches delivered specific insights, highlighting the relevance of a combination of methods. The map based on field mapping (Figure 10) contains all landforms, except for rock glaciers, supposed moraine ridges, and borders of vegetation changes, which were documented by remote mapping (i.e., with aerial images and shaded relief; Figure 12). Specific forms like double ridges in moraines (e.g., in the LIA moraine) or the transition zones from rounded to sharp rock debris on the surface would have not been discernible without a field campaign, as these subtle forms are not visible on aerial images. Distinguishing between moraine types (latero-frontal and hummocky, see Figure 13) was also only possible thanks to the field campaign, as this allowed for close inspection of surface characteristics and material. The aerial images conversely shed light on *remnant* and *supposed moraines* which would have not been possible to be mapped purely in the field due to their number and because, in the case of *remnant moraines*, they are only visible from a distance. Finally, the remote mapping strongly increased the quantity of mapped moraines, as it allowed for coverage of not only Brunnital, but the neighboring valleys as well.

The resolution of topographic background maps and aerial images and shaded reliefs used during the field mapping can affect the landforms that can be documented due to their size (Chandler et al., 2018). With a resolution of 0.25 m in the aerial images (aerial images from 2018/2019; swissALTI3D; both from swisstopo, 2023a), the mapping of moraines was not restricted, as these landforms are far larger than the image resolution. However, the scale of the topographic maps used for field mapping is 1:10,000 (maps from swisstopo, 2023a), rendering mapping by hand difficult in the case of smaller moraines. Also, correctly representing the size and position of moraines proved to be a challenge. However, by comparing the field mapping results to aerial images, these complexities could be addressed and corrected where needed.

The fluvial and gravitational processes had little interaction with the glacial landforms. Most of these mapped features have probably only been active since after the deposition of the moraines. Thus, unlike in other studies (e.g., Chandler et al., 2018), they did not provide clear insight into the chronology of moraine deposition. Nevertheless, the outermost *moraine remnants* in the LIA complex on the orographic right (Figure 10) appear to be covered by debris, whereas the inner moraines are not covered and therefore classified as *well-preserved* moraines. This suggests that the outer moraines of the complex are significantly older than the inner ones, as a gravitational event (e.g., rock fall) covering the outer moraines would have likely also reached the inner moraines. Therefore, the inner moraines may not have been deposited yet when the outer moraines were covered by a supposed rock fall event.

When relating the upper moraine cluster (Figure 27) to Holocene fluctuations of Brunnifirn (see Figure 28), the abundance of glacially derived material and landforms can be explained. The glacier extents forced with the ELA derived from the Milandre temperature reconstruction (Affolter et al., 2019b) repeatedly reached extents of this moraine cluster. This is a possible explanation for the high number of moraines, as the glacier could have provided enough sediment to allow for the formation of these moraines by reaching similar extents multiple times. In the case of the ELA forcing derived from the GISP2 temperatures (Alley, 2004), the glacier only reached the moraine cluster three times throughout the Holocene (see Figure 28). It remains unclear if these advances would have provided enough sediment for the formation of the high number of moraines, as this process is not only controlled by the presence of a glacier, but also by other factors such as material supply and hence erosion rates (Benn and Evans, 2010).

Overall, two clear extents could be identified based on the landforms mapped in the field and remotely: a first extent reaches the upper moraine cluster (Figure 27). The observed abundance of sediment and hummocky moraines could be explained by multiple advances to this extent. A second extent reaches the LIA moraine complex (see Figure 22), which consists of two separate ridges (see latero-frontal moraine on orographic right in Figure 10), which were likely deposited by two or more advances of similar size. In these supposed advances of similar length, the glacier may have pushed a second moraine onto an older ridge. On the one hand, both could have been ridges deposited during the LIA, which is supported by how the modeled high stands between ca 1600–1800 CE (see Figure 21) fit the mapped LIA moraine complex. A first advance clearly reaches the moraine around 1630 CE, and a second one around 1780 CE peaks at just ca 200 meters shorter. On the other hand, the first ridge could have been deposited around 8 ka, when the GISP2-forced reconstruction fits the LIA moraine, and the second ridge could have been deposited much later, during the LIA (Figure 28). Before 8.2 ka, the extent of the glacier modeled based on the Milandre temperature reconstruction is much larger than the LIA moraine, and thus cannot be responsible for the deposition of the older moraine. As no evidence of moraines further down valley than the LIA moraine complex was found, the glacier may have only fluctuated up to the LIA moraines throughout the modeled period from 9 ka until the LIA. One supposed moraine beyond the LIA moraine complex (see Figure 10) may be a result of a larger extent.

In conclusion of the assessment of the mapped landforms, numerous moraines indicate glacier fluctuations within the LIA moraine complex. However, little evidence was found for glacial extents beyond the LIA moraine complex. Only a *supposed moraine* above the peat bog (see Figure 10) and a lateral moraine likely deposited by Tschingelfirn (see Figure 12) were mapped further down valley. The boulders on the Hinterbalm slope (see Figure 3) can likely be attributed to Lateglacial advances. Therefore, from 9 ka onwards Brunnifirn likely fluctuated between the LIA and minimal extents similar to today (but more in balance with climate).

Temporal constraints by mapped landforms

With a radiocarbon age of ca 12.7–12.5 ka cal BP, the soil found within the outer ridge is significantly older than the modeled period. A possible explanation is that an old soil was eroded during an advance and deposited within the outer part of the frontal moraine, meaning that the age assigned to the soil cannot be transferred to the moraine itself. This would fit the idea of both ridges being deposited between 1600–1800 CE. A second possibility is based on the soil starting to form after moraine deposition and therefore showing the age of the moraine itself, which would contradict the fluctuations modeled based on the Milandre temperatures. As the model surface output shows, the Milandre temperatures cause the glacier to reach further down the valley before 8 ka (see Figure 21), reaching a width which would have probably eroded the older latero-frontal moraine. Therefore, the glacier could have never exceeded its LIA maximum throughout the Holocene by much. Similar findings have been made at other sites in the alps, e.g., in Lauterbrunnental. There, a ca 10.4 ka old peat bog has been documented outside of the LIA moraines, showing that the glacier did not exceed its LIA maximum around 8 ka (Egli et al., 2001; Wipf, 2001). Finally, contamination of the soil sample falsely resulting in an older age must be considered. By dating a second sample, the assigned age could be confirmed and credibility in correct age dating could be increased (Hajdas, 2008).

The historical Siegfried map provides a temporal constraint as it shows the glacier tongue almost reaching the moraine in 1859 CE (swisstopo, 2023a). The map fits the modeled fluctuations (see Figure 21), thus confirming that the glacier reached the moraine during the second half of the 19th century CE and showing that the temperatures used for the modeling of the last 500 years force a glacier of reasonable extent. The exact circumstances and the precise date of mapping however are unclear, as only the map available online (swisstopo, 2023b) could be used within the scope of this thesis, and the original template (Messtischblatt) was not considered. Moreover, field mapping was more precise than the historical map, as there is just one continuous moraine ridge without detailed separation of ridges marked on the historical map.

Further insight by boulder samples for beryllium-10 age dating

The processing of the boulder samples should follow shortly after conclusion of this thesis and will provide further understanding of the Holocene evolution of Brunnifirn. As steady state modeling showed, ELAs lower than the values derived from the temperature reconstructions considered in this thesis are required for the glacier to reach extents close to the locations of the boulder. This implies that the boulders were deposited during Lateglacial or Younger Dryas advances as found at other sites, e.g., Meiental or Göschenertal (Boxleitner et al., 2019a, 2019b).

Destruction and preservation of moraines

The mapping results showed that not all moraines were in the same condition (see Figure 10), as some were *well-preserved*, whereas others were classified as *supposed moraines*. Due to the active nature of the periglacial process area, movements like rock fall or slope creep can be reasons for the degradation of moraines (Ivy-Ochs et al., 2007). The hydrological processes should also be considered, as meltwater streams can destroy moraines (Mackintosh et al., 2017). In the case of the LIA moraine complex, several moraines appear to be covered by debris possibly originating from rock fall, which is known to erase traces of moraines (Barr and Lovell, 2014). The stream cuts through the main complex and probably eroded multiple moraines, and further moraines might be buried under the peat bog which may have formed from an outwash plain. Such fluvial processes often prevent moraines from being preserved (Barr and Lovell, 2014). The upper moraine complex is probably also affected by rock fall, as the mapped rock fall cones reach the moraines (see Figure 10), and by the stream which again cuts through the moraines. It is likely that these processes destroyed numerous moraines.

The bed of Brunnifirn changes from a steep upper section, to a flat overdeepening plain, to a second steep section, into a narrow but flat valley (plot B in Figure 17). Generally, if bed topography is steep, a change in ELA does not strongly affect the ratio of ablation versus accumulation area, resulting in less fluctuation in length. This relationship influences moraine deposition, as less fluctuation in length leads to fewer deposited moraines (Barr and Lovell, 2014). Owing to the steady state experiments the length change sensitivity of Brunnifirn could be assessed: if the ELA was varied through elevations of the middle section where the glacier is quite flat, strong changes in length occurred (i.e., ELA = 2730 m a.s.l. and below, see Figure 16). However, further down the valley than the LIA moraine no other moraines were found. Large extents exceeding the LIA moraines were modeled when forcing the glacier with the temperature reconstructions from the Milandre data (Affolter et al., 2019b), which raises the question of why there are no traces from such large extents. However, these suggested large extents were reached before 8.2 ka (Figure 28), and traces might have been eroded or buried by the above mentioned factors of degradation, which increasingly influence moraines with time (Barr and Lovell, 2014).

The double ridge found in the LIA moraine complex might be the result of a restricted second advance. When an ice advance reaches an already existing moraine, the older moraine hinders the glacier to reach its actual length (Barr and Lovell, 2014). However, as Brunnital is steep and geomorphological activity is high, moraines are expected to be small (Barr and Lovell, 2014), and therefore probably did not prevent the tongue from overriding the existing ride. The second ridge therefore likely stems from a second advance of smaller extent.

Finally, given the proximity of the mapped moraines in the LIA complex, and in the upper cluster, respectively, two potential error sources must be considered when correlating closely located moraines. They can either be wrongly related to one glacial advance instead of several, or falsely assumed to belong to separate advances instead of just one (Kirkbride and Winkler, 2012). This issue of correlating proximity of moraines to equal deposition time is also highlighted by Barr and Lovell (2014). In this thesis, neither climate nor glacial fluctuations were directly inferred from moraines. Steady states were modeled to match moraines, and possible steady state glacier ELAs were calculated from moraine positions, but fluctuations were modeled based on climate reconstructions and subsequently compared to moraine positions. Thus, these uncertainties cannot distort the results of this work.

4.2 ELAs inferred from mapping and steady state modeling

Research questions:

- 1c) What ELAs can be inferred from the reconstructed extents?
- 2a) What steady states match the mapped extents?

Based on the mapped moraines, ELAs were calculated for three extents: the current extent, an extent reaching the upper moraine cluster (Figure 27), and an extent reaching the LIA moraine complex. The conventional methods of mean elevation and AAR were applied to be compared with steady state modeling outputs. For the AAR a standard value of 0.66 was selected, which should produce similar results as the ELA values found by steady state modeling (Hubbard and Glasser, 2005; Mackintosh et al., 2017). As steady states are a theoretical concept, values must be compared with caution. Nevertheless, conventional methods allow for first estimations of ELAs (Leonard and Fountain, 2003)

The mapped moraines could be matched with steady state modeling, whereas today's extent was harder to reproduce exactly with modeling. A reason for this could be that today's extent is the result of a rapidly retreating glacier, whereas steady state modeling was conducted in a gradual approximation, usually lowering the ELA by 50 m increments and, if needed. Also, parts of the glacier were debris-covered, which strongly influences mass balance (Benn and Evans, 2010). The mean elevation method was also more complex to apply to today's extent than to the other two stages, as there is no clear front of the glacier (Figure 14). The AAR method was difficult to apply to the LIA and upper moraine cluster extent, as the larger glaciers of these stages had no clear ice margin to the north and west (Figure 22).

However, even if uncertainties of the theoretical ELA estimations based on the geometry of the glacier are high, the resulting values should be comparable to steady state modeling (Mackintosh et al., 2017). Indeed, the AAR and steady state modeling resulted in similar values (**Table *9***), with deviations of 15–50 m whereas the values calculated with the mean elevation method differed by 75–170 m. The surface and bed geometry of Brunnifirn are rather complex, which became evident in ground-penetrating radar ice thickness measurements (Grab et al., 2021). This is assumably the main reason for the differences in ELA values. Finally, specific glacier extents can be reached under different mass balance configurations (Mackintosh et al., 2017). Thus, inferences of climate from ELA reconstructions must be viewed critically. However, as mentioned in the chapter above, no conclusions of paleoclimate were made based on mapped moraines.

4.3 Transient modeling for fluctuating climate

Research question:

- 2b) How does the glacier vary with changing climate?

Transient modeling provides insights where conventional glacial reconstructions are limited: by forcing a glacier model with proxy reconstructions, the influence of fluctuating climate can be analyzed and compared to moraines (Mackintosh et al., 2017). To improve the modeled continuous glacier fluctuations, parameters and the resulting variations of the glacier output were assessed.

Influence of modeling parameters

Owing to the sensitivity experiments (Figure 20), the temperature-ELA conversion factor (ELA_{fc}) and the reference ELA (ELA0) could be adjusted to produce fluctuations which match the LIA moraine complex. Based on the outcome of sensitivity testing of the last 500 years, the last 9 ka were modeled. As different temperature reconstructions were used for the sensitivity testing period of the last 500 years than for the whole Holocene, it remains uncertain if the configuration of ELA_{fc} and ELA0 also fits the other two temperature reconstructions. The transition between the Holocene modeling and the onset of the modeling of 1500–2020 CE however is quite smooth (Figure 32), which indicates that the configuration is suitable for the Holocene temperature reconstructions. The only difference is a peak just before 1550 CE, followed by a retreat to then transition into the LIA maximum around 1630 CE. The sensitivity experiments showed that the starting glacier surface geometry influenced fluctuations for about 200 years, which explains the peak at 1550 CE only 50 years after the switch in temperature reconstructions.

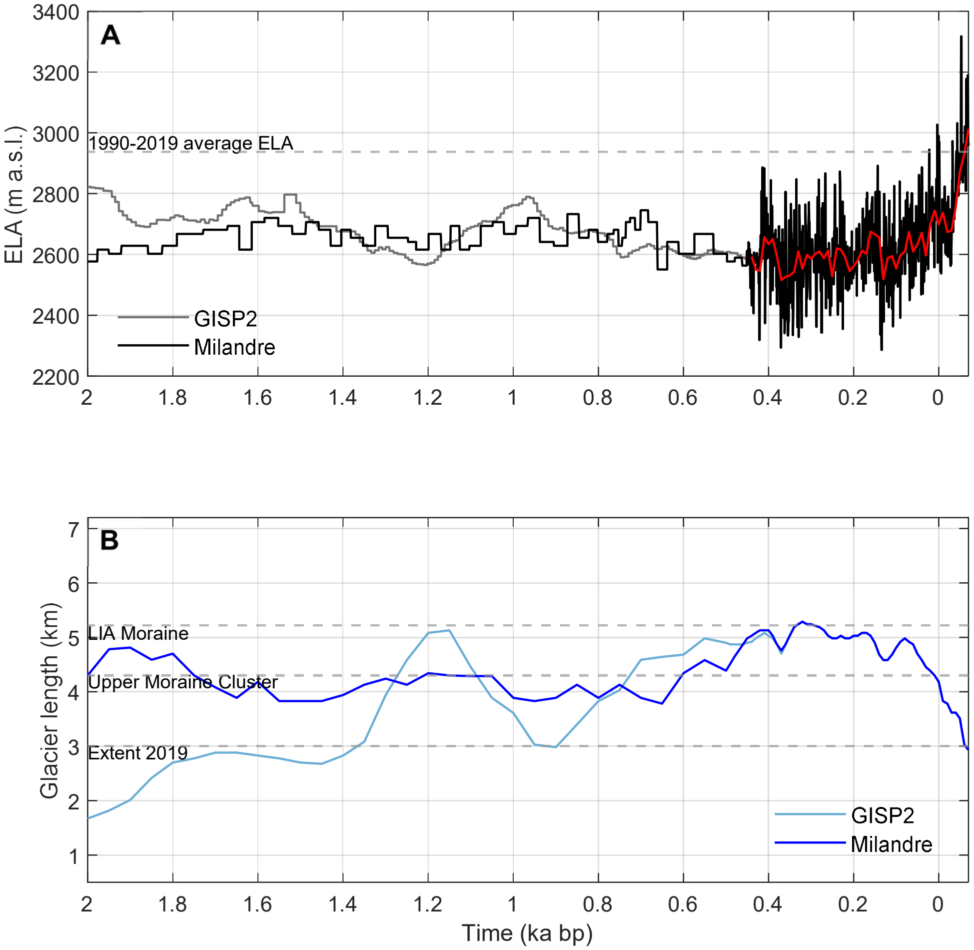

Figure 32: *Transition from Milandre and GISP2 modeling to the last 500 years. A) ELA forcing derived from the GISP2 and Milandre temperature reconstructions until 0.45 ka, from then on, the forcing of the last 500 years is applied (with 10-year means as red line). B) Fluctuations based on the forcings. Note how temperatures of the GISP2 and Milandre record are already cooling before 1500 CE (i.e., 0.45 ka BP) but the result of the last 500 years similar: after an initial advance just before 1550 CE, the maximum is reached around 1630 CE. After a smaller third maximum, a period of retreat follows. Finally, there is a last readvance, transitioning into a strong retreat until today.*

As explained in chapter 172.3.1, parameters like the mass balance gradient or the ice softness had to be selected based on assumptions. Different parameters would strongly change the model outcome. However, as the aim of this thesis was to model fluctuations over long time periods, it is more effective to apply a 2-D SIA flow model that uses linear equations to calculate ice extent from temperatures instead of a climate model-driven Stokes model (Mackintosh et al., 2017). The ELA-temperature conversion deviates from values applied in other studies (e.g., Lüthi, 2014; Oerlemans, 2010; Six and Vincent, 2014; Thibert et al., 2013; Vincent, 2002). Sensitivity testing showed that a value of 130 m °C^{-1} is necessary to fit the mapped moraines.

As pointed out by Mackintosh et al. (2017), comparisons to mapped landforms increase confidence in modeling outputs.

The mass balance gradient of 1.6 was approximated with an ablation and an accumulation area gradient ratio which corresponds to an AAR of 2:1. This ratio is however based on steady state conditions which do not apply when modeling with fluctuating climate. A study with a similar aim applied a ratio of 1.7 (Rea et al., 2020), however this study focused on glaciers all over Europe, incorporating cirque glaciers, valley glaciers, and icefields, and therefore cannot be compared to the application of the model in this thesis. Nevertheless, testing the influence of different ratios should be conducted in future applications of the model used here.

Finally, confirmation of an appropriate model calibration and parameter choice was found when looking at the fit of other smaller glaciers in the modeled area. Tschingelfirn, a small glacier consisting of several tributaries on the north-eastern end of Brunnital, reached two moraines during its possible LIA maximum and 8.2 ka maximum (Figure 33). The length of this glacier was not documented during the modeling, but it culminated at the same time as Staldenfirn and Glatscher da Strem, which seemingly have similar response times due to their small size. That the modeled ice surface not exclusively fits for the main glaciers analyzed in this thesis reinforces the accuracy of modeling outputs.

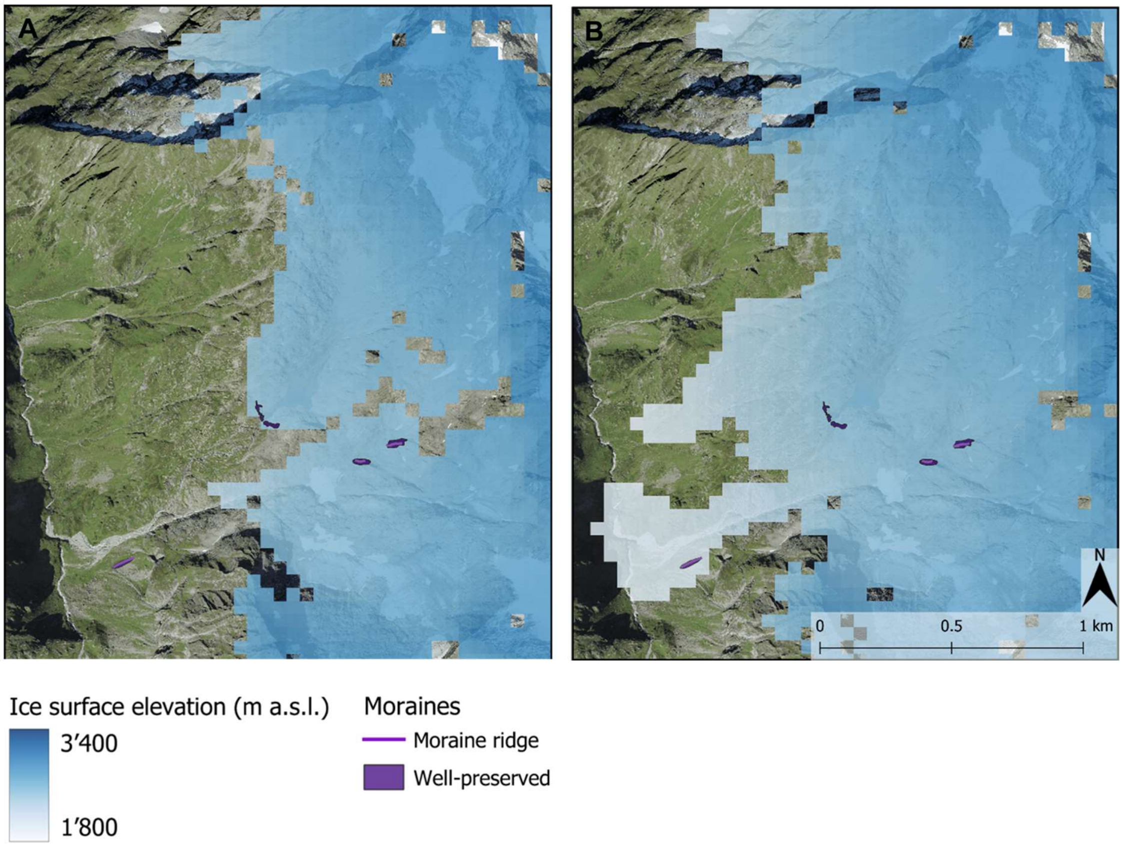

Figure 33: *A) Possible LIA maximum of Tschingelfirn. B) Possible Holocene maximum as reaction to the 8.2 ka cooling recorded in the Milandre-derived ELA forcing. Both are just possible maxima, as the length of Tschingelfirn was not recorded. Maxima of Staldenfirn and Glatscher da Strem were used as indicators. Note how the central moraine ridge in A) and the lateral moraine in B) fit the modeled ice extent. Background map: swisstopo (2023).*

Sinus and step change experiments

The conducted ELA sinus experiments gave insight into the behavior of the glacier when climate is transient. To not only see variations in behavior to different sinus periods, these experiments were also conducted for four different initial glacier stages (see Figure 18; Figure 19; and Figure 43; Figure 44 in the appendix). The stage of the glacier for which the sinus forcing is run determined length variations. A small glacier showed length responses to every sinus period, whereas a large glacier showed no response to 20 ELA sinus periods. This occurs due to the lag in response of length changes given by the physics of glaciers, as the mass needs to be redistributed to an extent until first changes in length are visible (as described by e.g., Leysinger Vieli and Gudmundsson, 2004). The volume however showed an immediate response to a shift in ELA. Such behavior became evident when comparing the volume response of a small and a large glacier to different ELA sinus periods, as they look alike in shape. Short climate signals which were lost in the length fluctuations of a large glacier were clearly visible when looking at the volume.

The step change experiments highlighted the ELA limit below which changes lead to immense length changes. Moreover, a hysteresis level was found, likely cause by microclimate differences between advance and retreat, and supported by the bed geometry of an overdeepening (see Figure 17). With the measured volume change of step change experiments, response times were calculated.

Response time

The response times, i.e., *e* folding times, calculated from the volume change of step change experiments and the theoretical calculations based on ablation and mass balance gradient (method A: Jóhannesson et al., 1989; method B: Harrison et al., 2003) were similar, only diverging within a range of ca 10 years. Here, the focus was on the stages which were explored in all three approaches: (1) a small glacier not filling the plateau, (2) a glacier reaching the edge of the plateau, (3) a glacier flowing over the edge, and (4) an extent reaching the LIA moraines. All values are compiled in Table 10, Table 11, and Table 12.

(1) The range calculated for the *e* folding time (50–70 years) agreed with the theoretical calculations. The results of method A agreed with the minimum of the range (ca 50 years), whereas the results of method B varied strongly when average or maximum ice thickness are used (ca 42 and 77 years, respectively). Due to ca 14 m difference between maximal and average ice thickness, a range instead of a fixed value seems more sensible.

(2) This case needs to be differentiated: for the theoretical calculations, steady states for ELA0 = 2730 and 2720 m a.s.l. were used, whereas step changes had to be conducted with 50-meter increments, resulting in values for the step changes from 2800 to 2750 and 2750 to 2700 m a.s.l. ELAs. The respective smaller glacier did however not flow over the edge, whereas the respective large glacier reached the steep section. Therefore, the two situations of higher and lower ELA are compared with each other, respectively.

A range of 80–100 years resulted from the *e* folding time calculation, whereas method A derived ca 137 years, and method B yielded ca -359 (maximum thickness) and 1440 (average thickness) years. The negative value stemmed from the low ablation value which leads to the denominator turning negative. As the value for ablation at the tongue is too small (ca -0.61 m a^{-1}), these results seem erroneous. Ablation rates below 1 m a^{-1} are seen in glaciers of high-polar climate, leading to response times of 150–600 years (Cuffey and Paterson, 2010). The response time of over 1000 years seems unlikely, as this too would not be expected from a valley glacier in the Alps. Response times over 1000 years can be observed in ice caps or ice sheets (Cuffey and Paterson, 2010). Therefore, the range from 80–100 years or the value of ca 137 years from method A seem more plausible.

(3) For a glacier terminating in the steep section after the plateau, the longest response times were calculated. The *e* folding time ranged from 160–180 years, method A resulted in ca 166.5 years, and method B yielded ca 52 (average thickness) and ca 177 (maximal thickness) years. The *e* folding range and result of method A agree, as well as the maximal thickness value of method B. The average thickness showed a much smaller response time, however, when considering the bed geometry, calculating an average of the ice thickness is questionable. The large overdeepening where maximal ice thickness is found and the main part of the total mass accumulates is evened out in an average thickness, which leads to an underestimation of response time.

(4) For the glacier reaching the LIA moraine, the *e* folding time of a step change from 2650 to 2600 m a.s.l. is compared to the theoretical response times of the steady state with ELA0 = 2585 m a.s.l. The *e* folding time values range from 40–50 years, whereas method A yielded 62 years, and method B resulted in ca 39 (average thickness) and ca 110 (maximal thickness) years. Here, the opposite to case (3) seems to apply: the maximal thickness probably is not representative of the general thickness. This may result from the ELA now being below the edge of the plain, which means that the accumulation area extends over the plain, removing influence from the area of overdeepening.

The theoretical calculations were compared to the modeling results and are thus evaluated based on their accuracy in comparison to the *e* folding time. Given the simplicity of the approach, method 1 (Jóhannesson et al., 1989) yields reliable results, except for when ice thickness is not uniform or when the ablation at the tongue is underestimated.

The difference in results when using maximal versus average ice thickness in method B (Harrison et al., 2003) highlights the importance of considering the bed geometry. Using average thickness results in smaller response times than using maximal thickness. If the thickness applied in the calculation is not representative of the overall ice thickness, response time values may be erroneous. When selecting a value of ablation at the tongue, this should agree to values generally expected from similar glaciers. In this thesis, the ablation value furthest at the front was used. As discussed, further analysis is recommended when ablation values do not agree with expected ablation.

Transient volume and length sensitivity

The temperature curve-based modeling applies fluctuating climate, resulting in a more realistic depiction of volume and length reactions. Comparing these transient results to steady state modeling highlights the difference in reactions of the glacier to natural climate fluctuations. The results of the last 500 years modeling period are displayed with the steady state results (Figure 34; Figure 35; Figure 36).

Throughout most of the modeling period, glacier length and ELA (i.e., climate) fluctuated within the lower right part of the plot (Figure 34). This reflects the length plot of the period, showing that the glacier was large during most of the modeled period (Figure 21). Outliers in ELA do not necessarily correspond to length: warm years at the beginning of the modeled period do not cause the glacier to retreat strongly, neither do cold years towards the end of the modeled period cause the glacier to advance strongly. This relationship agrees with the concept of delayed length response of glaciers. The volume plot on the other hand displays direct variations (Figure 35), resulting from the immediate response of glacier volume when the ELA changes. Both components show the same trend at the end of the modeled period, namely an unprecedented retreat. The rapid reaction of the volume provides a scale for imminent length declines.

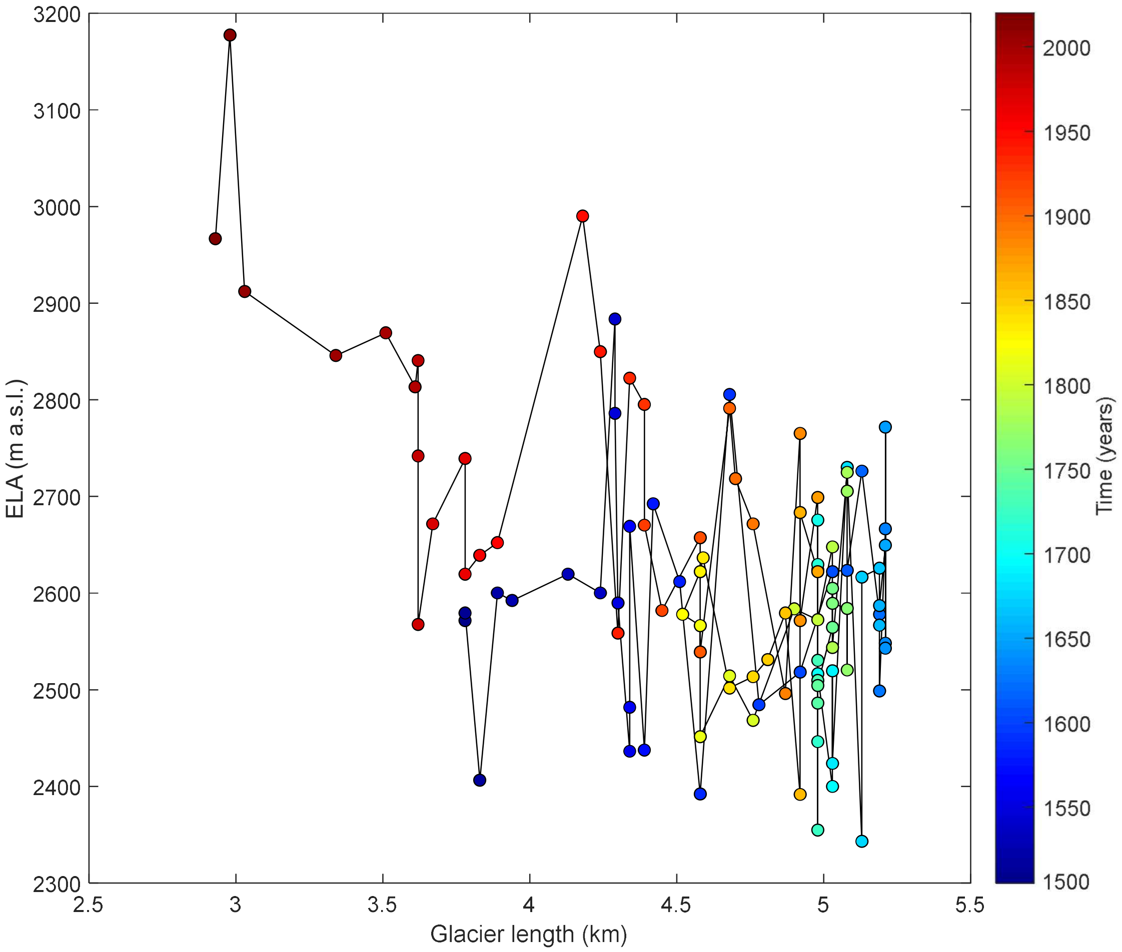

Figure 34: *ELA and corresponding glacier lengths extracted from the results of the last 500 years modeling period (one value per year). The time scale corresponds to the modeled period from 1500–2020 CE.*

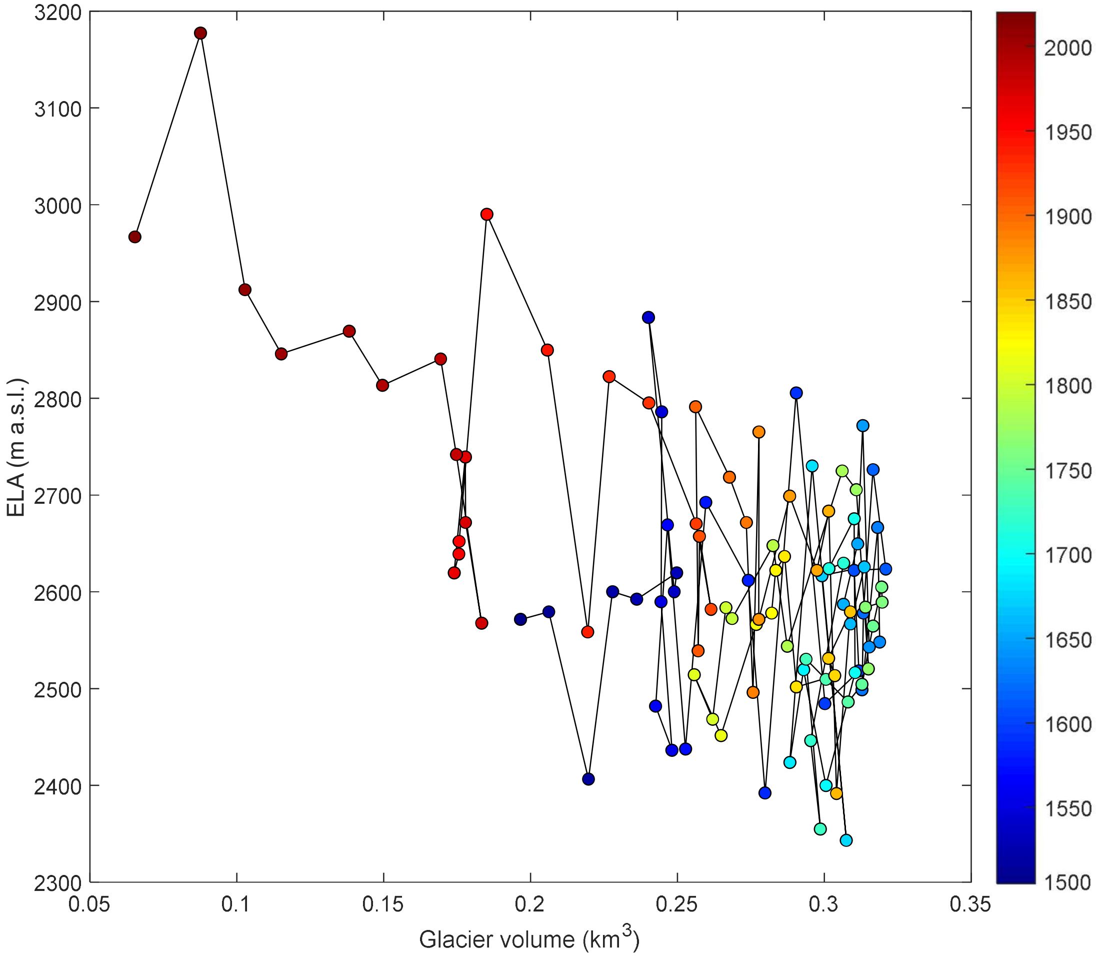

Figure 35: *ELA and corresponding glacier volumes extracted from the results of the last 500 years modeling period (one value per year). The time scale corresponds to the modeled period from 1500–2020 CE.*

Finally, comparing the length results of steady state modeling to the transient length-ELA relation sheds light on the imbalance of the glacier with climate. As glaciers react with a delay to changes in climate, values of transient modeling deviate from the steady state results. Transient modeling data points which lie close to the steady state ELA-length line imply that the glacier length resembles steady state extents of similar climate. However, this points out that the currently observed length is not representative for the current climate. Even if the ongoing climate change stopped, the glacier would still strongly retreat to reach steady state.

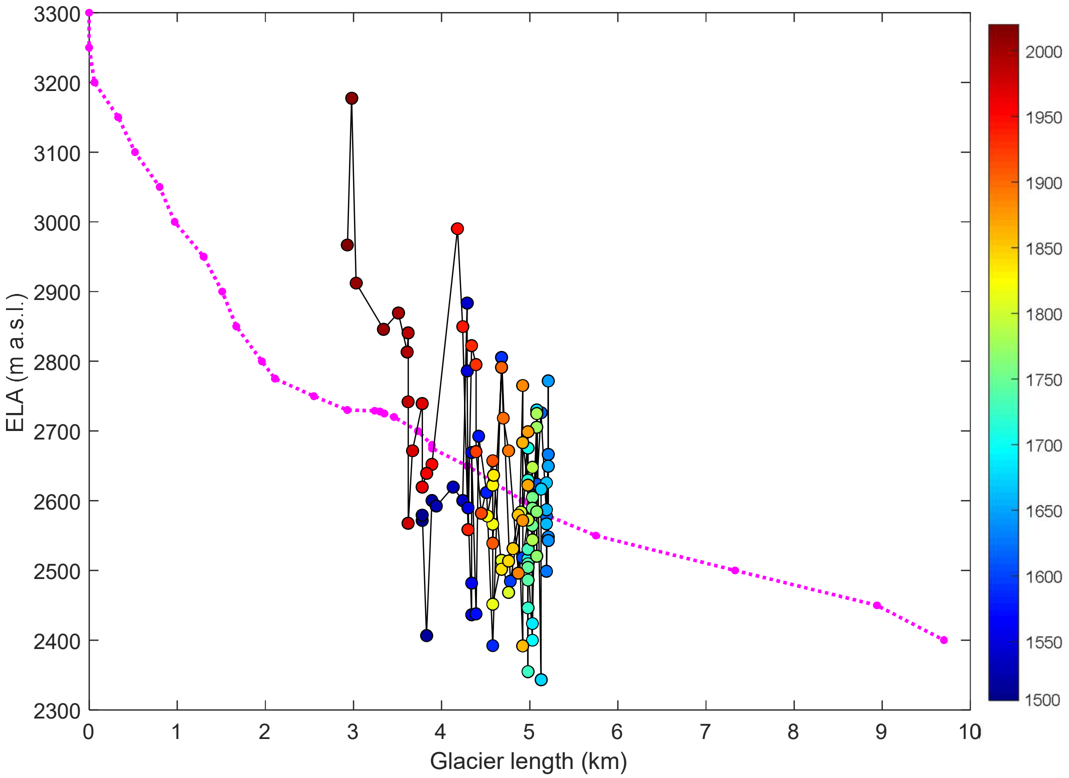

Figure 36: *ELA and corresponding glacier lengths extracted from the results of the last 500 years modeling period (one value per year), with the steady state modeling length results in the background (magenta). The time scale corresponds to the modeled period from 1500–2020 CE.*

4.4 Assessing reconstructed fluctuations

Research question:

- 2c) How did glacier extents fluctuate given the Holocene climate variations and how do fluctuations compare to the geomorphological constraints?

The last 500 years

The modeled period of 1500–2020 CE showed a high stand beyond all other Holocene advances after 9 ka (except for the advance before 8.2 ka; see Figure 28). Due to the divergence of the Milandre and GISP2 temperature reconstructions before 1500 CE (0.45 ka), the focus lies on culminations after 1500 CE, for which only one temperature reconstruction was used (combination of Casty et al., 2005a; and MeteoSwiss, 2023). Four culminations were found within the advanced position between ca 1500–1900 CE (Figure 32). The double ridge in the main moraine complex mapped in the field agrees with the concept of two or more advances to similar extent. Other studies found comparable advances in the Alps during the LIA. Grosser Aletschgletscher and Gornergletscher, for example, each reached three similar maximal extents between 1300–1900 CE (Holzhauser et al., 2005).

The long-term temperature forcings (Affolter et al., 2019b; Alley, 2004) produced a clearly visible first culmination (at ca 1540 CE). In the fluctuations based on the yearly high-resolution forcing (Casty et al., 2005a; MeteoSwiss, 2023), this maximum rather seemed like a plateau during an advance (at ca 1550 CE). However, as the sensitivity experiments have shown (Figure 20), if there is more ice at the start of the modeling period (1500 CE), this maximum is better distinguished. Therefore, this first maximum at ca 1540–1550 CE was reproduced with all temperature forcings.

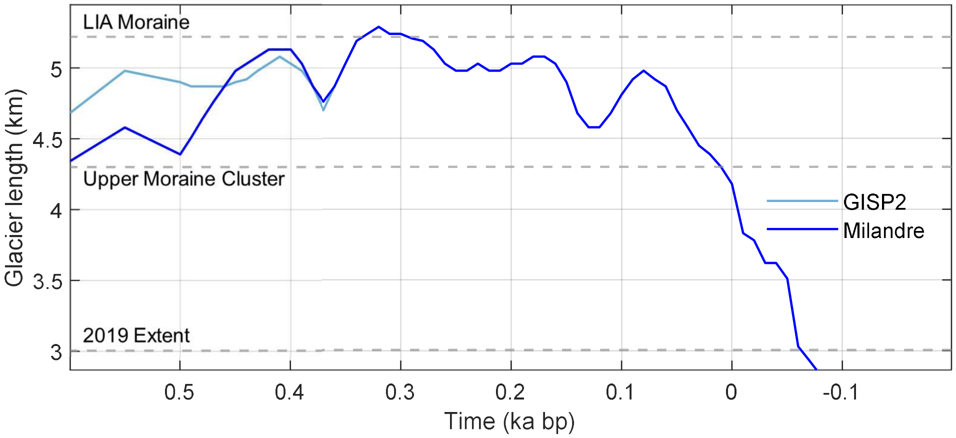

Figure 37: *Culminations during the modeling of 1500–2020 CE. Note that until 1499 CE (0.451 ka), the long-term temperature data is used (Affolter et al., 2019b; Alley, 2004). From then onwards, the high-resolution temperature data is applied (Casty et al., 2005a; MeteoSwiss, 2023). The first culmination is thus more distinct than in the modeling from only 1500 CE on (see Figure 21), as the long-term data force the advance already before 1500 CE. Nevertheless, the first maximum at ca 1540–1550 CE (0.41–0.4 ka) is reproduced with all temperature forcing curves.*

Out of the modeled culminations for the period from 1500 CE onwards, the first (ca 1540 CE) did not reach the moraines by ca 100, with the gap between the tongue and the moraines varying by 50 m depending on the temperature forcing. These differences are negligible, due to the model grid size being set to 50 m. The second and largest modeled LIA advance (culminating ca 1630 CE) exceeded the position of the moraines. Following a short retreat, the glacier reached a third maximum (ca 1770 CE), with a length comparable to that of the first maximum. After a retreat period of about 50 years, the glacier readvanced to its last LIA maximum (ca 1870 CE). This fourth smaller culmination does not match the lengths of the other three advances before. All LIA advances are visible in Figure 37.

The culminations of Grosser Aletschgletscher and Gornergletscher occurred ca 1370–1390 CE, 1670 CE, and 1860–1865 CE (rounded values from Holzhauser et al., 2005). The first maxima of Grosser Aletschgletscher and Gornergletscher at ca 1370–1390 CE was also reproduced for Brunnifirn with both long-term temperature reconstructions (Affolter et al., 2019b; Alley, 2004), however the extents caused by the two different forcings diverge strongly.

The first modeled maximum of Brunnifirn at ca 1540 CE was not documented for these larger glaciers, which may be a result of longer response times. Brunnifirn retreated for ca 50 years before the next readvance, whereas the larger glaciers might just not have noticeably reacted to this climate signal. However, considering the calculated response times of ca 40–60 years (see

Table 10, Table 11, and Table 12), the climate signal must have been quite strong if it caused Brunnifirn to retreat. Therefore, this might point to insecurities in the temperature data.

The modeled second (ca 1630 CE) culmination of Brunnifirn fits the maxima of Grosser Aletschgletscher and Gornergletscher at ca 1670 CE, considering the supposed longer response times. The response times may also be responsible for Grosser Aletschgletscher and Gornergletscher not showing a maximum at the same time as the third modeled maximum of Brunnifirn (ca 1770 CE). Finally, the fourth maximum (ca 1870 CE) of Brunnifirn fits the maxima of the other glaciers (ca 1860–1865). Thus, the exact timing of maxima remains questionable, as the concept of longer response time for the larger glacier does is not applicable anymore for this last maximum.

The fluctuations of Unterer Grindelwaldgletscher (Nussbaumer et al., 2011), a glacier with a shorter response time than Grosser Aletschgletscher and Gornergletscher, highlight the differences in timing (Figure 38). The second and fourth maxima of Brunnifirn occur before maxima of Unterer Grindelwaldgletscher, whereas the third advance of Brunnifirn culminates at the same time as the respective advance of Unterer Grindelwaldgletscher. Further examples for comparable glacier response were found in the Austrian Alps (Nicolussi and Patzelt, 2000) and in the Italian and Western Alps with LIA maxima around 1820 CE and shorter last LIA maxima around 1850 CE (Solomina et al., 2015).

In conclusion, other glaciers in the Alps show similar patterns as the modeled fluctuations of Brunnifirn. The exact timing of extents however remains unclear. The geomorphological landforms confirm two or more extents to similar size but cannot constrain the exact timing of maximal extents. The intact outer ridge shows that the last advance was surely not the largest one, as the inner ridge is pushed onto the outer one.

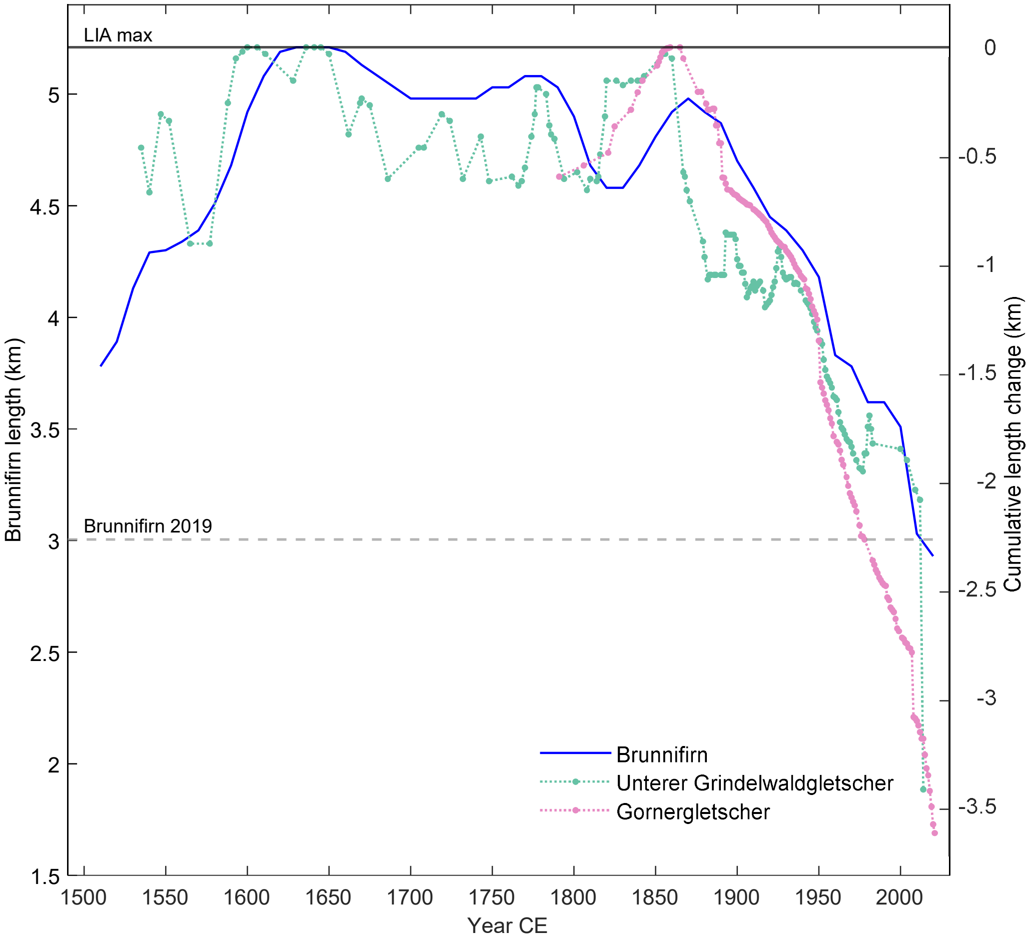

Figure 38: *The modeled fluctuations of Brunnifirn (forced with the high-resolution data by Casty et al., (2005) and MeteoSwiss (2023)) in comparison to cumulative length changes from the LIA maximum of Unterer Grindelwaldgletscher and Gornergletscher (data from Nussbaumer et al., 2011). The LIA moraine of Brunnifirn corresponds to the LIA maximum. The patterns of culminations are similar, the timing however is different.*

Following the last LIA maximum, the modeling produced a constant retreat with a short period of stagnation from ca 1980–1990 CE (see Figure 38). This reaction is consistent with other glaciers, e.g., Unterer Grindelwaldgletscher (Nussbaumer et al., 2011), or Steingletscher (Schimmelpfennig et al., 2022). As for the LIA culminations, the timing and extent of this reaction differed, and can be explained by response times. The length measurements (GLAMOS, 2022) and the mapped aerial images showed that the model overestimated the size of the glacier until ca 2010 CE (Figure 21). As the model was calibrated to the LIA moraines, the rapid retreat since 1990 CE could not be reproduced exactly. In 2019 CE, the model slightly underestimated the glacier size found on the aerial image of that year (Figure 24). Both representations of lower accuracy indicate that the applied calibration of the model fits best for LIA extents.

The Holocene after 9 ka

Assessing all modeled advance and retreat periods from 9 ka onward would exceed the scope of this thesis. Therefore, only general trends, prominent maxima, or contradictions are discussed in the following section.

Throughout the modeled period based on the long-term temperature reconstructions (Affolter et al., 2019b; Alley, 2004) from 9 ka onwards, the extents of Brunnifirn varied strongly. The temperatures reconstructed from the GISP2 ice core are much warmer than those based on the Milandre speleothem record. Trends however are similar, with the GISP2-forced fluctuations always culminating slightly before the Milandre-forced fluctuations (Figure 40). This similarity increases the probability that modeled advances occurred in reality, but when the ratio between a maximum and a subsequent minimum is different in one modeling curve compared to the other, this highlights the necessity of further analysis.

The advance just before 8.2 ka was documented at other sites, e.g., at Mont Miné (Nicolussi and Schlüchter, 2012). As a reaction to a climatic cooling event (Alley and Ágústsdóttir, 2005), it seems likely that Brunnifirn advanced strongly. As both temperature reconstructions forced an advance, likelihood increases, but the extent the glacier reached remains unsure. Compared to fluctuations of Rhonegletscher, the advance beyond the modeled maximum forced by the Milandre temperatures seems unlikely, as Rhonegletscher was probably smaller than during the LIA and 2011 CE at that time (Goehring et al., 2011). A second and more thorough sampling campaign from the peat bog in Brunnital could provide a constraint, if lower layers could be age dated.

After the high stand of ca 8.2 ka, both climate reconstructions caused a significant retreat (Figure 39). At the onset of the period for which the archeological finds are dated (7.95–7.75 ka), modeling showed a retreat to either the upper moraine cluster (Milandre forcing), or far beneath the 2019 CE extent (GISP2 forcing). In the scenario forced by the Milandre temperature reconstruction, the glacier retreated further until it reached its 2019 CE extent above the edge of the plain by 7.75 ka. The modeling based on the GISP2 forcing produced a readvance beginning before 7.75 ka. Throughout the period from 7.95–7.75 ka, the trend therefore is the same.

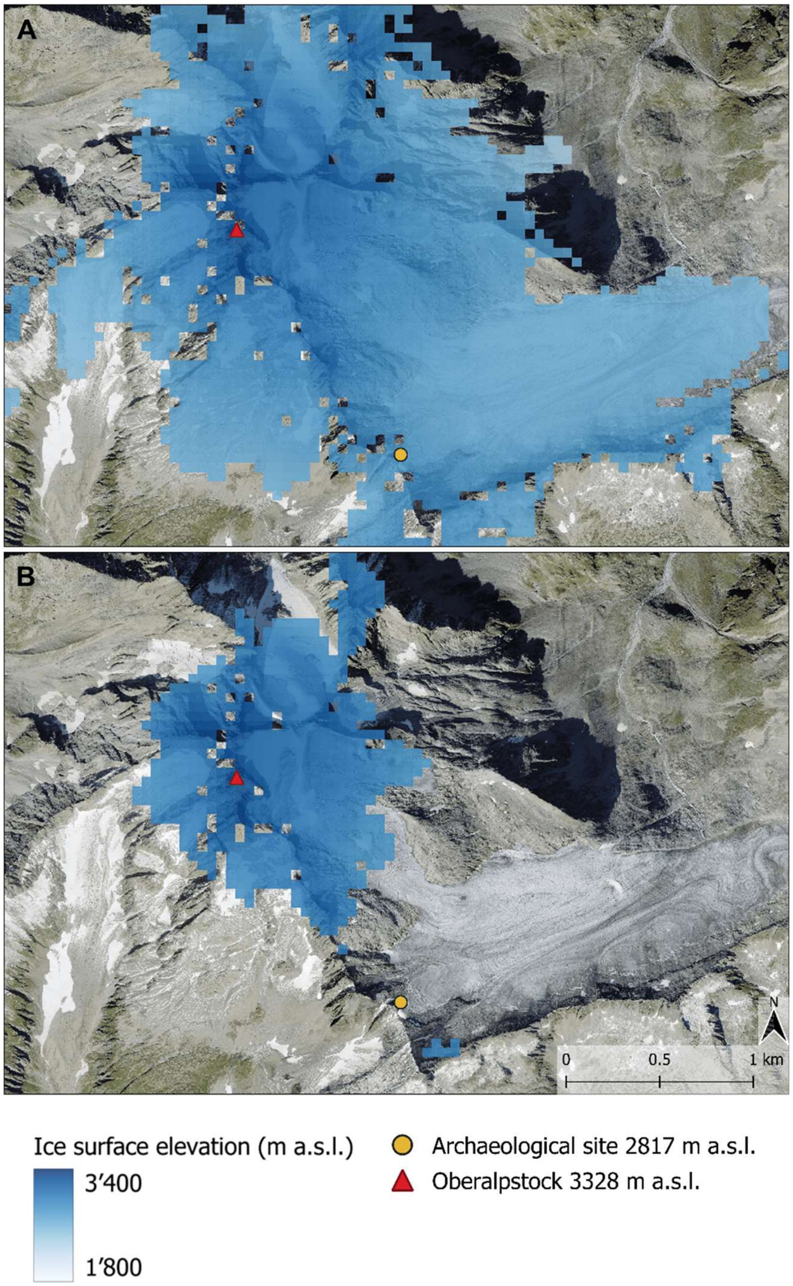

Figure 39: *Possible minimal extents of Brunnifirn during the period to which the artifacts were dated, based on the two different climate forcings (extract of 7.75 ka). A) Milandre temperature forcing. B) GISP2 forcing. Background map: swisstopo (2023).*

During the 200-year period for which the artifacts for dated, the modeling suggests that Brunnifirn fluctuated strongly (Figure 26). The minimal extents (at 7.75 ka) produced by both temperature forcings are displayed in Figure 39, indicating that the possible extents at that time varied strongly. As there are no landforms to constrain the extent, it remains unclear, which of the temperature forcings produced the more reliable reconstruction. However, as the minimal extents at the end of the 200-year period were either similar to or smaller than today, the cave may have been ice-free at that time.

Throughout the rest of the modeled period until 1500 CE, Brunnifirn either mostly fluctuated between its 2019 extent and the upper moraine cluster (Milandre temperature forcing) or was mostly smaller than in 2019 CE (GISP2 temperature forcing). Findings from other sites indicate that glaciers during this period were smaller than during the LIA, some even smaller than their early 21st century extents. Rhonegletscher was mostly smaller than in 2011 CE during the same period (Goehring et al., 2011). Similarly, Steingletscher was smaller than in 2000 CE for a total of ca 7 ka from 10 ka onwards (Schimmelpfennig et al., 2022). Results of smaller glaciers throughout the Mid-Holocene than in the LIA were also found in the Austrian Alps (Braumann et al., 2020) and the Italian Alps (Badino et al., 2018).

The modeled reconstruction showed an advance before ca 4.2 ka which is consistent with an advance in the Ecrins-Pelvoux massif, Western Alps (Le Roy et al., 2017). The extent of the advance however seems unclear, as neither of the temperature forcings applied caused an advance similar to the LIA maximum, whereas glaciers in the Ecrins-Pelvoux massif slightly exceeded their LIA maximal extents (Le Roy et al., 2017).

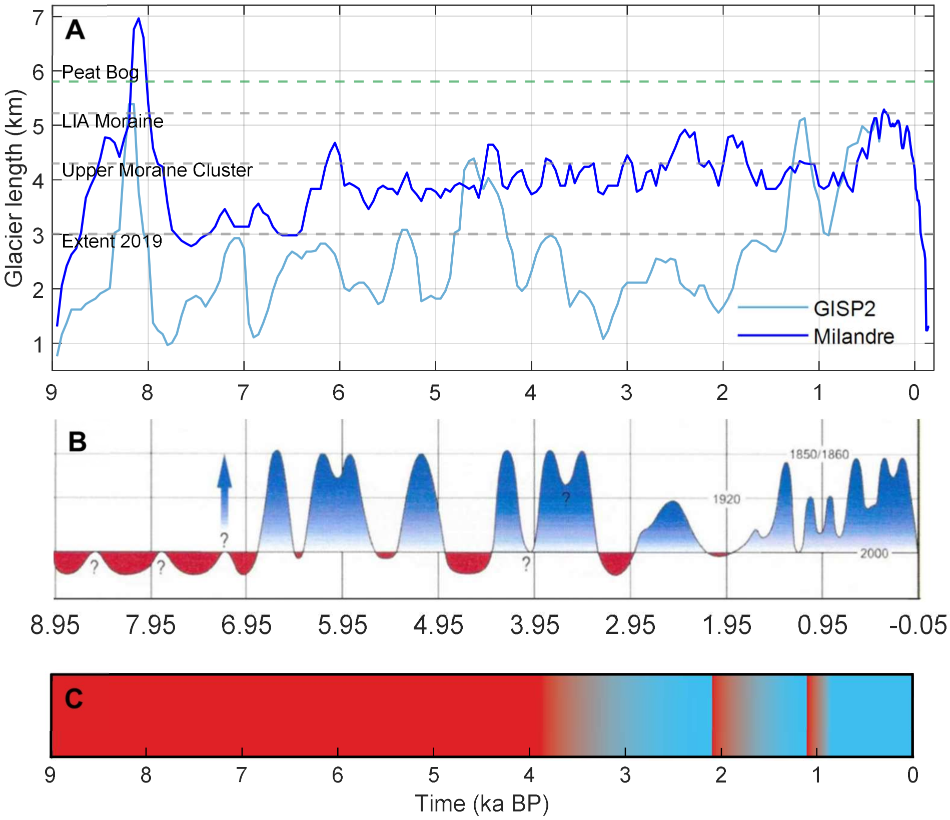

Figure 40: *A) Modeled fluctuations of Brunnifirn based on the different temperature reconstructions (Affolter et al., 2019b; Alley, 2004; Casty et al., 2005a; MeteoSwiss, 2023). B) glacier fluctuations throughout the Holocene in the Swiss and Western Alps, modified excerpt from Holzhauser (2010). Blue fluctuations stand for advances over the extent of glaciers in the year 2000 CE, retreats beneath that level are marked in red. Question marks and the arrow stand for unknown duration or extent of fluctuations. C) Fluctuation scenario of Rhonegletscher, modified except from Goehring et al. (2011), where red areas stand for an extent smaller than in 2011 CE, and blue areas stand for an extent larger than in 2011 CE. Shaded parts show transitional periods.*

The modeling of the period from 9 ka onwards provided compelling indications of the fluctuations of Brunnifirn. Rarely any evidence for this period was found with geomorphological mapping. Except for the peat bog, a supposed moraine, and the lateral moraine supposedly deposited by Tschingelfirn (as described in section 4.1), no mapped landforms marked possible fluctuations beyond the LIA moraine complex. Considering the archeological artifacts, it seems likely that after 8.2 ka, Brunnifirn was fluctuating within its LIA maximum extent, sometimes smaller than today. Retreats were likely more in balance with climate than today.

Future

The four temperature scenarios applied to model a possible future evolution of Brunnifirn showed a retreat unprecedented in the whole modeling period from 9 ka until today (Figure 30). Brunnifirn will likely retreat to the highest flanks of Oberalpstock, independent of the RCP scenario, which is consistent with other future simulations of glaciers in the Alps (e.g., Zekollari et al., 2019). By 2099 CE, the DMI-HIRHAM_ECEARTH simulation forced the glacier to retreat above 2900 m a.s.l. in the RCP2.6 scenario, above 3100 m a.s.l. for the RCP4.5 scenario, and let it completely disappear in the RCP8.5 scenario. The other simulations produced similar results (Figure 54; Figure 55; Figure 56). The plain may likely soon disconnect from the upper steep section of the glacier, as the connection is already narrow today (e.g., background map in Figure 14) and the ice is thin (Grab et al., 2021). Similar evolutions were modeled for other glaciers, displaying immense retreats (e.g., Huss et al., 2007; Linsbauer et al., 2012). Both climate forcings (GISP2 and Milandre) suggest that Brunnifirn has filled the plain for ca the last 1.5 ka (Figure 40). The landscape of the large plain will thus be altered significantly by the end of the century, as it is the case for other sites in the Alps (e.g., Zumbühl et al., 2021).

Climate data

As the version of the model applied in this thesis is forced by an ELA history and ELAs were calculated based on temperatures, the modeled fluctuations are governed by the temperature reconstructions. As pointed out by Mackintosh et al. (2017), a glacier extent can be forced by multiple factors due to the principle of equifinality. Adding precipitation to the model might improve modeling quality and constrain extents. However, temperature is the primary controlling mechanism of temperate glaciers (Mackintosh et al., 2017), thus the approach chosen for this thesis seems reasonable.

Due to low spatial resolution of climate models, it is common to apply lapse rates to temperatures to adjust them to the local climate of glaciers (Mackintosh et al., 2017). In this case, temperatures were fitted by comparing averages to the high-alpine temperature record (MeteoSwiss, 2023), as explained in sections 2.3.5 and 2.3.6. Lapse rate calculations were exemplarily conducted (with a dry adiabatic lapse rate of -9.8° km^{-1}) but the resulting temperatures were too cold and would have not forced the model to reach the desired LIA moraine position. Relating modeled reconstructions of fluctuations to geomorphological landforms can explain disagreements caused by different temperature records (Mackintosh et al., 2017), thus the chosen approach is a practical combination to assess both reconstruction methods.

Regarding the location of the proxy sources for the applied temperature reconstructions, the Milandre reconstruction (Affolter et al., 2019b) is likely to be more reliable. However, it also had to be shifted to fit the high-alpine temperature record (MeteoSwiss, 2023), and does therefore also not represent the local climate of Brunnifirn. Both temperature reconstructions applied for modeling from 9–0.451 ka in this thesis show the same trends and provide insight into varying climate. The different fluctuations modeled with the reconstructions highlight uncertainties. Thus, seems crucial to apply multiple temperature reconstructions.

4.5 Outlook

Based on the findings in this thesis, the following approaches could further constrain the possible Holocene fluctuations of Brunnifirn:

- Landform age dating. Sampling from the bottom of the peat bog could constrain the extent of the advance before 8.2 ka. The large, polished bedrocks in proximity of the peat bog could possibly be exposure dated, which would also constrain fluctuations exceeding the LIA maximum.
- Modeling with other temperature proxy reconstructions. The more temperature forcings and resulting fluctuations are compared, the better could diverging results be explained.
- Glaciological survey. Conducting ablation measurements on Brunnifirn and including these values into the numerical model could improve the quality of modeled fluctuations.

5 Conclusion

The aim of this thesis was to reconstruct Holocene fluctuations of Brunnifirn, Central Swiss Alps. Geomorphological mapping was combined with numerical ice-flow modeling to produce a fully dynamic time transient reconstruction of glacier fluctuations. Reconstructions were constrained by landforms mapped in the field and remotely. A time-dependent 2-D ice-flow model (as applied by Brown et al., 2013; Evans et al., 2012) was forced with an ELA history derived from different proxy temperature reconstructions: the GISP2 ice core record (Alley, 2004) and the Milandre speleothem cave record (Affolter et al., 2019b) for the period from 9 ka until 1500 CE; and reconstructed yearly summer temperatures (Casty et al., 2005b) and measured temperatures (MeteoSwiss, 2023) for the period from 1500 CE until 2020 CE.

Around the LIA moraine already mapped in the geological layer by swisstopo (2023), numerous further latero-frontal moraines were found, presenting a double ridge and possibly older moraines. The glacier may therefore have reached similar extents at least twice. Moreover, an abundance of hummocky moraines was found further up the valley, proposing an extent reached multiple times. A radiocarbon dated peat bog showed that the glacier did not override its position for the last 3.8–3.5 ka cal BP.

Besides the peat bog, no compelling evidence of extents older than the LIA was found with geomorphological mapping. However, modeling suggests that Brunnifirn likely advanced shortly before 8.2 ka to an extent of the LIA moraine complex or further. Between 7.95–7.75 ka, Brunnifirn may have been similar to its 2019 extent, possibly enabling the deposition of archeological artifacts found above the ice surface (Reitmaier et al., 2016). Thereafter, the glacier likely fluctuated within its LIA maximum and 2019 extent. After 0.45 ka, modeling resulted in three similar advances to about the LIA moraine complex, with the first advance at ca 1630 CE being the largest, and the last maximum occurring at ca 1870 CE. These modeled fluctuations agree with findings from other studies; however, periods of contradicting results were found.

The results of dynamic and time-transient modeling stressed the relevance of response time when assessing past glacier fluctuations. Temperatures below the average of the last 30 years forced the glacier to retreat to extents smaller than today. Modeling indicated that the glacier is currently far from its steady state, and future temperature projections demonstrated a minimum extent unprecedented throughout the last 9 ka, independent of the RCP scenario.

References

Affolter, S., Häuselmann, A., Fleitmann, D., Lawrence Edwards, R., Cheng, H., Leuenberger, M., 2019a. Central Europe temperature constrained by speleothem fluid inclusion water isotopes over the past 14,000 years. Sci. Adv. 5, 1–10.

Affolter, S., Häuselmann, A.D., Fleitmann, D., Edwards, R.L., Cheng, H., Leuenberger, M.C., 2019b. Inferred temperatures from Milandre Cave, Switzerland. PANGAEA.

Alley, R.B., 2004. GISP2 Ice Core Temperature and Accumulation Data. IGBP Pages/ World Data Cent. Paleoclimatology 2004–013.

Alley, R.B., 2000a. The Younger Dryas cold interval as viewed from central Greenland. Quat. Sci. Rev. 19, 213–226.

Alley, R.B., 2000b. Ice-core evidence of abrupt climate changes. Proc. Natl. Acad. Sci. U. S. A. 97, 1331–1334.

Alley, R.B., Ágústsdóttir, A.M., 2005. The 8k event: Cause and consequences of a major Holocene abrupt climate change. Quat. Sci. Rev. 24, 1123–1149.

Badino, F., Ravazzi, C., Vallè, F., Pini, R., Aceti, A., Brunetti, M., Champvillair, E., Maggi, V., Maspero, F., Perego, R., Orombelli, G., 2018. 8800 years of high-altitude vegetation and climate history at the Rutor Glacier forefield, Italian Alps. Evidence of middle Holocene timberline rise and glacier contraction. Quat. Sci. Rev. 185, 41–68.

Barr, I.D., Lovell, H., 2014. A review of topographic controls on moraine distribution. Geomorphology 226, 44–64.

Begert, M., Frei, C., 2018. Long-term area-mean temperature series for Switzerland—Combining homogenized station data and high resolution grid data. Int. J. Climatol. 38, 2792–2807.

Benn, D.I., Evans, D.J.A., 2010. Glaciers & Glaciation, 2nd ed. Hodder Education, London.

Bohleber, P., Schwikowski, M., Stocker-Waldhuber, M., Fang, L., Fischer, A., 2020. New glacier evidence for ice-free summits during the life of the Tyrolean Iceman. Sci. Rep. 10, 1–10.

Bonani, G., Ivy, S.D., Hajdas, I., Niklaus, T.R., Suter, M., 1994. AMS 14C age determinations of tissue, bone and grass samples from the Ötztal Ice Man. Radiocarbon 36, 247–250.

Boxleitner, M., Ivy-Ochs, S., Egli, M., Brandova, D., Christl, M., Dahms, D., Maisch, M., 2019a. The 10Be deglaciation chronology of the Göschenertal, central Swiss Alps, and new insights into the Göschenen Cold Phases. Boreas 48, 867–878.

Boxleitner, M., Ivy-Ochs, S., Egli, M., Brandova, D., Christl, M., Maisch, M., 2019b. Lateglacial and Early Holocene glacier stages - New dating evidence from the Meiental in central Switzerland. Geomorphology 340, 15–31.

Braumann, S.M., Schaefer, J.M., Neuhuber, S.M., Lüthgens, C., Hidy, A.J., Fiebig, M., 2021. Early Holocene cold snaps and their expression in the moraine record of the eastern European Alps. Clim. Past 17, 2451–2479.

Braumann, S.M., Schaefer, J.M., Neuhuber, S.M., Reitner, J.M., Lüthgens, C., Fiebig, M., 2020. Holocene glacier change in the Silvretta Massif (Austrian Alps) constrained by a new 10Be chronology, historical records and modern observations. Quat. Sci. Rev. 245, 106493.

Bronk Ramsey, C., 2009. Bayesian analysis of radiocarbon dates. Radiocarbon 51, 337–360.

Bronk Ramsey, C., 2001. Development of the radiocarbon calibration program. Radiocarbon 43, 355–363.

Brönnimann, S., Franke, J., Nussbaumer, S.U., Zumbühl, H.J., Steiner, D., Trachsel, M., Hegerl, G.C., Schurer, A., Worni, M., Malik, A., Flückiger, J., Raible, C.C., 2019. Last phase of the Little Ice Age forced by volcanic eruptions. Nat. Geosci. 12, 650–656.

Brown, V.H., Evans, D.J.A., Vieli, A., Evans, I.S., 2013. The Younger Dryas in the English Lake District: Reconciling geomorphological evidence with numerical model outputs. Boreas 42, 1022–1042.

Calitri, F., Sommer, M., Norton, K., Temme, A., Brandová, D., Portes, R., Christl, M., Ketterer, M.E., Egli, M., 2019. Tracing the temporal evolution of soil redistribution rates in an agricultural landscape using 239+240Pu and 10Be. Earth Surf. Process. Landforms 44, 1783–1798.

Calitri, F., Sommer, M., van der Meij, W.M., Tikhomirov, D., Christl, M., Egli, M., 2021. 10Be and 14C data provide insight on soil mass redistribution along gentle slopes and reveal ancient human impact. J. Soils Sediments 21, 3770–3788.

Casty, C., Wanner, H., Luterbacher, J., Esper, J., Böhm, R., 2005a. European Alps Temperature and Precipitation Reconstructions. IGBP Pages/ World Data Cent. Paleoclimatology 2005–070.

Casty, C., Wanner, H., Luterbacher, J., Esper, J., Böhm, R., 2005b. Temperature and precipitation variability in the European Alps since 1500. Int. J. Climatol. 25, 1855–1880.

CH2018, 2018. CH2018 - Climate Scenarios for Switzerland. Technical Report. Natl. Cent. Clim. Serv.

Chandler, B.M.P., Lovell, H., Boston, C.M., Lukas, S., Barr, I.D., Benediktsson, Í.Ö., Benn, D.I., Clark, C.D., Darvill, C.M., Evans, D.J.A., Ewertowski, M.W., Loibl, D., Margold, M., Otto, J.C., Roberts, D.H., Stokes, C.R., Storrar, R.D., Stroeven, A.P., 2018. Glacial geomorphological mapping: A review of approaches and frameworks for best practice. Earth-Science Rev. 185, 806–846.

Cornelissen, M., Auf der Maur, C., Reitmaier, T., 2022. A Glacially Preserved Mesolithic Rock Crystal Extraction Site in the Swiss Alps. Nor. Archaeol. Rev. 55, 96–102.

Cuffey, K., Paterson, W.S.B., 2010. The Physics of Glaciers, Fourth Edi. ed. Butterworth-Heinemann/Elsevier.

Egli, M., Mirabella, A., Fitze, P., 2001. Clay mineral formation in soils of two different chronosequences in the Swiss Alps. Geoderma 104, 145–175.

Eis, J., van der Laan, L., Maussion, F., Marzeion, B., 2021. Reconstruction of Past Glacier Changes with an Ice-Flow Glacier Model: Proof of Concept and Validation. Front. Earth

Evans, D.J.A., Harrison, S., Vieli, A., Anderson, E., 2012. The glaciation of Dartmoor: The southernmost independent Pleistocene ice cap in the British Isles. Quat. Sci. Rev. 45, 31–53.

Favilli, F., Egii, M., Brandova, D., Ivy-Ochs, S., Kubik, P.W., Maisch, M., Cherubini, P., Haeberli, W., 2009a. Combination of numerical dating techniques using 10be in rock boulders and 14C of resilient soil organic matter for reconstructing the chronology of glacial and periglacial processes in a high alpine catchment during the late Pleistocene and early Holocen. Radiocarbon 51, 537–552.

Favilli, F., Egli, M., Brandova, D., Ivy-Ochs, S., Kubik, P., Cherubini, P., Mirabella, A., Sartori, G., Giaccai, D., Haeberli, W., 2009b. Combined use of relative and absolute dating techniques for detecting signals of Alpine landscape evolution during the late Pleistocene and early Holocene. Geomorphology 112, 48–66.

Feigenwinter, I., Kotlarski, S., Casanueva, A., Fischer, A., Schwierz, C., Liniger, M.A., 2018. Exploring quantile mapping as a tool to produce user tailored climate scenarios for Switzerland. Tech. Rep. MeteoSwiss.

GLAMOS, 2022. Swiss Glacier Length Change. Glacier Monit. Switz. release 20.

Goehring, B.M., Schaefer, J.M., Schluechter, C., Lifton, N.A., Finkel, R.C., Jull, A.J.T., Akçar, N., Alley, R.B., 2011. The Rhone Glacier was smaller than today for most of the Holocene. Geology 39, 679–682.

Grab, M., Mattea, E., Bauder, A., Huss, M., Rabenstein, L., Hodel, E., Linsbauer, A., Langhammer, L., Schmid, L., Church, G., Hellmann, S., Deleze, K., Schaer, P., Lathion, P., Farinotti, D., Maurer, H., 2021. Ice thickness distribution of all Swiss glaciers based on extended ground-penetrating radar data and glaciological modeling. J. Glaciol. 67, 1074–1092.

Grosjean, M., Suter, P.J., Trachsel, M., Wanner, H., 2007. Ice-borne prehistoric finds in the Swiss Alps reflect Holocene glacier fluctuations. J. Quat. Sci. 22, 203–207.

Hajdas, I., 2008. Radiocarbon dating and its applications in Quaternary studies. E&G Quat. Sci. J. 57, 2–24.

Harrison, W.D., Raymond, C.F., Echelmeyer, K.A., Krimmel, R.M., 2003. A macroscopic approach to glacier dynamics. J. Glaciol. 49, 13–21.

Heyman, J., Hättestrand, C., Stroeven, A.P., 2008. Glacial geomorphology of the Bayan Har sector of the NE Tibetan Plateau. J. Maps 4, 42–62.

Holzhauser, H., 2010. Zur Geschichte des Gornergletschers. Ein Puzzle aus historischen Dokumenten und fossilen Hölzern aus dem Gletschervorfeld. Geographica Bernensia, Bern.

Holzhauser, H., Magny, M., Zumbühl, H.J., 2005. Glacier and lake-level variations in west-central Europe over the last 3500 years. The Holocene 15, 789–801.

Hubbard, B., Glasser, N., 2005. Field Techniques in Glaciology and Glacial Geomorphology. John Wiley & Sons Ltd, Chichester.

Huss, M., Sugiyama, S., Bauder, A., Funk, M., 2007. Retreat Scenarios of Unteraargletscher, Switzerland, Using a Combined Ice-Flow Mass- Balance Model. Arctic, Antarct. Alp. Res. 39, 422–431.

Hutter, K., 1983. Theoretical Glaciology: material science of ice and the mechanics of glaciers and ice sheets. D. Reidel Publishing Company and Terra Scientific Publishing Company, Tokyo.

IPCC, 2013. Climate Change 2013: The Physical Science Basis. Contribution of Working Group I to the Fifth Assessment Report of the Intergovernmental Panel on Climate Change. Cambridge University Press, Cambridge, United Kingdom and New York, NY, USA.

Ivy-Ochs, S., Kerschner, H., Maisch, M., Christl, M., Kubik, P.W., Schlüchter, C., 2009. Latest Pleistocene and Holocene glacier variations in the European Alps. Quat. Sci. Rev. 28, 2137–2149.

Ivy-Ochs, S., Kerschner, H., Schlüchter, C., 2007. Cosmogenic nuclides and the dating of Lateglacial and Early Holocene glacier variations: The Alpine perspective. Quat. Int. 164–165, 53–63.

Jóhannesson, T., Raymond, C.F., Waddington, E.D., 1989. A simple method for determining the response time of glaciers, in: Oerlemans, J. (Ed.), Glacier Fluctuations and Climatic Change. Kluwer Academic Publishers, Dordrecht, pp. 343–352.

Kirkbride, M.P., Winkler, S., 2012. Correlation of Late Quaternary moraines: Impact of climate variability, glacier response, and chronological resolution. Quat. Sci. Rev. 46, 1–29.

Kronig, O., Ivy-Ochs, S., Hajdas, I., Christl, M., Wirsig, C., Schlüchter, C., 2018. Holocene evolution of the Triftje- and the Oberseegletscher (Swiss Alps) constrained with 10Be exposure and radiocarbon dating. Swiss J. Geosci. 111, 117–131.

Le Roy, M., Deline, P., Carcaillet, J., Schimmelpfennig, I., Ermini, M., ASTER Team, 2017. 10Be exposure dating of the timing of Neoglacial glacier advances in the Ecrins-Pelvoux massif, southern French Alps. Quat. Sci. Rev. 178, 118–138.

Leonard, K.C., Fountain, A.G., 2003. Map-based methods for estimating glacier equilibrium-line altitudes. J. Glaciol. 49, 329–336.

Leysinger Vieli, G.J.-M.C., Gudmundsson, G.H., 2004. On estimating length fluctuations of glaciers caused by changes in climatic forcing. J. Geophys. Res. Earth Surf. 109, 1–14.

Linsbauer, A., Paul, F., Haeberli, W., 2012. Modeling glacier thickness distribution and bed topography over entire mountain ranges with GlabTop: Application of a fast and robust approach. J. Geophys. Res. 117.

Lüthi, M.P., 2014. Little Ice Age climate reconstruction from ensemble reanalysis of Alpine glacier fluctuations. Cryosph. 8, 639–650.

Mackintosh, A.N., Anderson, B.M., Pierrehumbert, R.T., 2017. Reconstructing Climate from Glaciers. Annu. Rev. Earth Planet. Sci. 45, 649–680.

MeteoSwiss, 2023. Area-mean temperatures of northern Switzerland > 1000 m a.s.l. 1864-2021 (Version 1.1). URL https://www.meteoschweiz.admin.ch/service-und-publikationen/applikationen/ext/climate-swissmean.html

Nicolussi, K., Drescher-Schneider, R., Le Roy, M., Schlüchter, C., 2014. Alpine Gletscherschwankungen während des Holozäns. Geogr. Rundsch. 7, 16–22.

Nicolussi, K., Patzelt, G., 2000. Discovery of early-Holocene wood and peat on the forefield of the Pasterze Glacier, Eastern Alps, Austria. The Holocene 10, 191–199.

Nicolussi, K., Schlüchter, C., 2012. The 8.2 ka event – Calendar-dated glacier response in the Alps. Geology 40, 819–822.

Nussbaumer, S.U., Steinhilber, F., Trachsel, M., Breitenmoser, P., Beer, J., Blass, A., Grosjean, M., Hafner, A., Holzhauser, H., Wanner, H., Zumbühl, H.J., 2011. Alpine climate during the Holocene: A comparison between records of glaciers, lake sediments and solar activity. J. Quat. Sci. 26, 703–713.

Oerlemans, J., 2010. The Microclimate of Valley Glaciers. Igitur, Utrecht Publishing & Archiving Services, Utrecht.

Oerlemans, J., Hoogendoorn, N.C., 1989. Mass-balance gradients and climatic change. J. Glaciol. 35, 399–405.

Paterson, W.S.B., Budd, W.F., 1982. Flow parameters for ice sheet modeling. Cold Reg. Sci. Technol. 6, 175–177.

Pilø, L., Reitmaier, T., Fischer, A., Barrett, J.H., Nesje, A., 2023. Ötzi, 30 years on: A reappraisal of the depositional and post-depositional history of the find. The Holocene 33, 112–125.

Porter, S.C., 1975. Equilibrium-line altitudes of Late Quaternary glaciers in the Southern Alps, New Zealand. Quat. Res. 5, 27–47.

Rea, B.R., Pellitero, R., Spagnolo, M., Hughes, P., Ivy-Ochs, S., Renssen, H., Ribolini, A., Bakke, J., Lukas, S., Braithwaite, R.J., 2020. Atmospheric circulation over Europe during the Younger Dryas. Sci. Adv. 6, 1–14.

Reimer, P.J., Austin, W.E.N., Bard, E., Bayliss, A., Blackwell, P.G., Bronk Ramsey, C., Butzin, M., Cheng, H., Edwards, R.L., Friedrich, M., Grootes, P.M., Guilderson, T.P., Hajdas, I., Heaton, T.J., Hogg, A.G., Hughen, K.A., Kromer, B., Manning, S.W., Muscheler, R., Palmer, J.G., Pearson, C., Van Der Plicht, J., Reimer, R.W., Richards, D.A., Scott, E.M., Southon, J.R., Turney, C.S.M., Wacker, L., Adolphi, F., Büntgen, U., Capano, M., Fahrni, S.M., Fogtmann-Schulz, A., Friedrich, R., Köhler, P., Kudsk, S., Miyake, F., Olsen, J., Reinig, F., Sakamoto, M., Sookdeo, A., Talamo, S., 2020. The IntCal20 Northern Hemisphere Radiocarbon Age Calibration Curve (0-55 cal kBP). Radiocarbon 62, 725–757.

Reitmaier, T., Auf der Maur, C., Reitmeier-Naef, L., Seifert, M., Walser, C., 2016. Spätmesolithischer Bergkristallabbau auf 2800 m Höhe nahe der Fuorcla da Strem Sut (KT. Uri/Graubünden/CH). Archäologisches Korrespondenzblatt 46, 133–148.

Schimmelpfennig, I., Schaefer, J.M., Akçar, N., Koffman, T., Ivy-Ochs, S., Schwartz, R., Finkel, R.C., Zimmerman, S., Schlüchter, C., 2014. A chronology of Holocene and Little Ice Age glacier culminations of the Steingletscher, Central Alps, Switzerland, based on high-sensitivity beryllium-10 moraine dating. Earth Planet. Sci. Lett. 393, 220–230.

Schimmelpfennig, I., Schaefer, J.M., Lamp, J., Godard, V., Schwartz, R., Bard, E., Tuna, T., Akçar, N., Schlüchter, C., Zimmerman, S., Aumaître, G., Bourlès, D., Keddadouche, K., 2022. Glacier response to Holocene warmth inferred from in situ 10Be and 14C bedrock analyses in Steingletscher's forefield (central Swiss Alps). Clim. Past 18, 23–44.

Six, D., Vincent, C., 2014. Sensitivity of mass balance and equilibrium-line altitude to climate change in the French Alps. J. Glaciol. 60, 867–878.

Solomina, O.N., Bradley, R.S., Hodgson, D.A., Ivy-Ochs, S., Jomelli, V., Mackintosh, A.N., Nesje, A., Owen, L.A., Wanner, H., Wiles, G.C., Young, N.E., 2015. Holocene glacier fluctuations. Quat. Sci. Rev. 111, 9–34.

swisstopo, 2023a. Bundesamt für Landestopografie. URL https://map.geo.admin.ch

swisstopo, 2023b. map.geo.admin.ch. URL https://map.geo.admin.ch/

CH2018 Project Team, 2018. CH2018 - Climate Scenarios for Switzerland. Natl. Cent. Clim. Serv.

Thibert, E., Eckert, N., Vincent, C., 2013. Climatic drivers of seasonal glacier mass balances: An analysis of 6 decades at Glacier de Sarennes (French Alps). Cryosph. 7, 47–66.

Vincent, C., 2002. Influence of climate change over the 20th Century on four French glacier mass balances. J. Geophys. Res. Atmos. 107, ACL 4-1-ACL 4-12.

Walker, M., Head, M.J., Berkelhammer, M., Björck, S., Cheng, H., Cwynar, L., Fisher, D., Gkinis, V., Long, A., Lowe, J., Newnham, R., Rasmussen, S.O., Weiss, H., 2018. Formal ratification of the subdivision of the Holocene Series/ Epoch (Quaternary System/Period): Two new Global Boundary Stratotype Sections and Points (GSSPs) and three new stages/ subseries. Episodes 41, 213–223.

Walker, M.J.C., Berkelhammer, M., Björck, S., Cwynar, L.C., Fisher, D.A., Long, A.J., Lowe, J.J., Newnham, R.M., Rasmussen, S.O., Weiss, H., 2012. Formal subdivision of the Holocene Series/Epoch: A Discussion Paper by a Working Group of INTIMATE (Integration of ice-core, marine and terrestrial records) and the Subcommission on Quaternary Stratigraphy (International Commission on Stratigraphy). J. Quat. Sci. 27, 649–659.

Wanner, H., Beer, J., Bütikofer, J., Crowley, T.J., Cubasch, U., Flückiger, J., Goosse, H., Grosjean, M., Joos, F., Kaplan, J.O., Küttel, M., Müller, S.A., Prentice, I.C., Solomina, O., Stocker, T.F., Tarasov, P., Wagner, M., Widmann, M., 2008. Mid- to Late Holocene climate change: an overview. Quat. Sci. Rev. 27, 1791–1828.

Wipf, A., 2001. Gletschergeschichtliche Untersuchungen im spät- und postglazialen Bereich des Hinteren Lauterbrunnentals (Berner Oberland, Schweiz). Geogr. Helv. 56, 133–144.

Zekollari, H., Huss, M., Farinotti, D., 2019. Modelling the future evolution of glaciers in the European Alps under the EURO-CORDEX RCM ensemble. Cryosph. 13, 1125–1146.

Zollinger, B., Alewell, C., Kneisel, C., Meusburger, K., Gärtner, H., Brandová, D., Ivy-Ochs, S., Schmidt, M.W.I., Egli, M., 2013. Effect of permafrost on the formation of soil organic carbon pools and their physical-chemical properties in the Eastern Swiss Alps. Catena 110, 70–85.

Zumbühl, H.J., Nussbaumer, S.U., Wipf, A., 2021. Top of Europe: The Finsteraarhorn–Jungfrau Glacier Landscape, in: Reynard, E. (Ed.), Landscapes and Landforms of Switzerland. World Geomorphological Landscapes. Springer Nature Switzerland AG, Cham, pp. 217–233.

6 Appendix

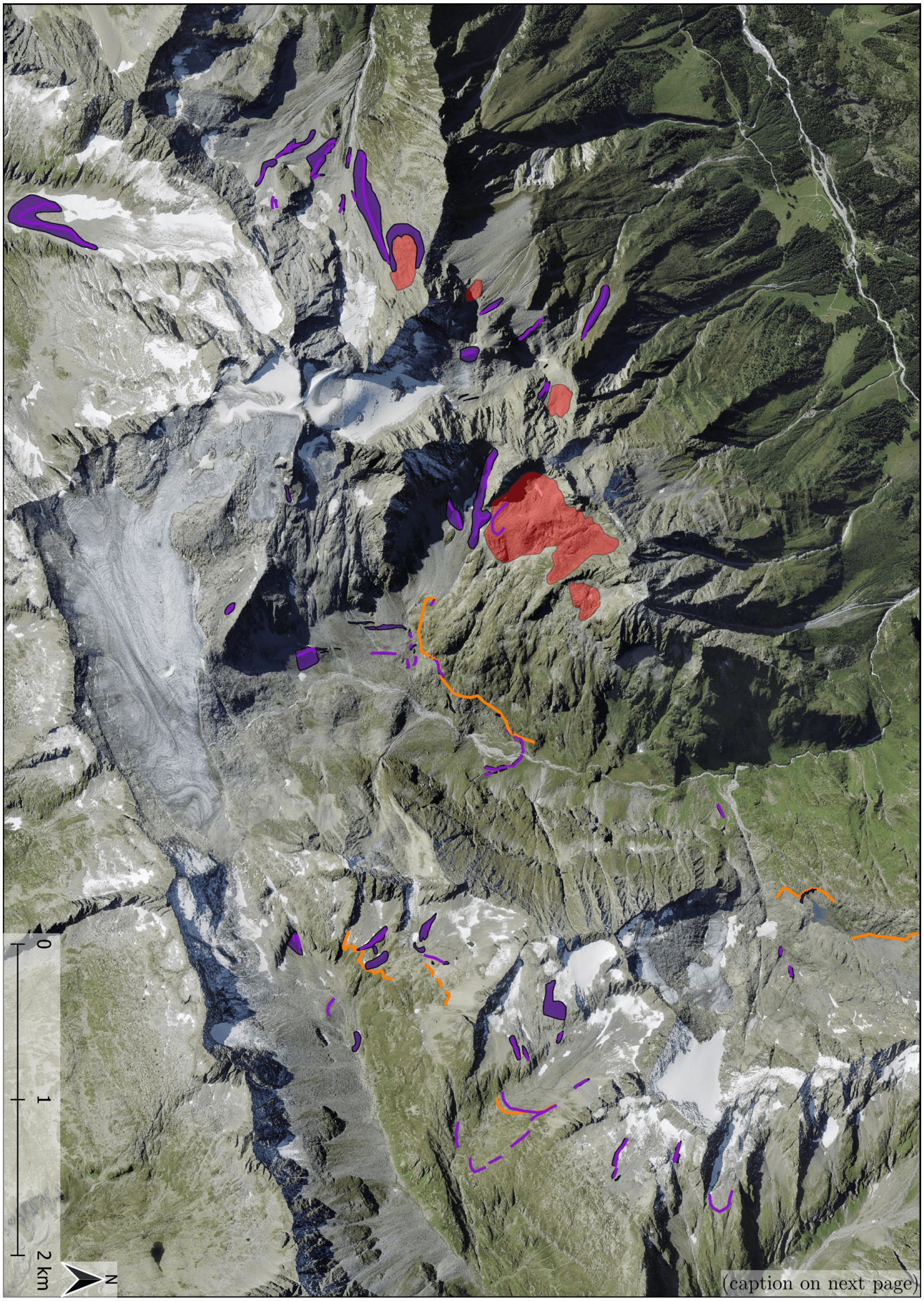

(caption on next page)

Figure 41: *Geomorphological map of the whole area mapped based on aerial images. Background map: swisstopo (2023).*

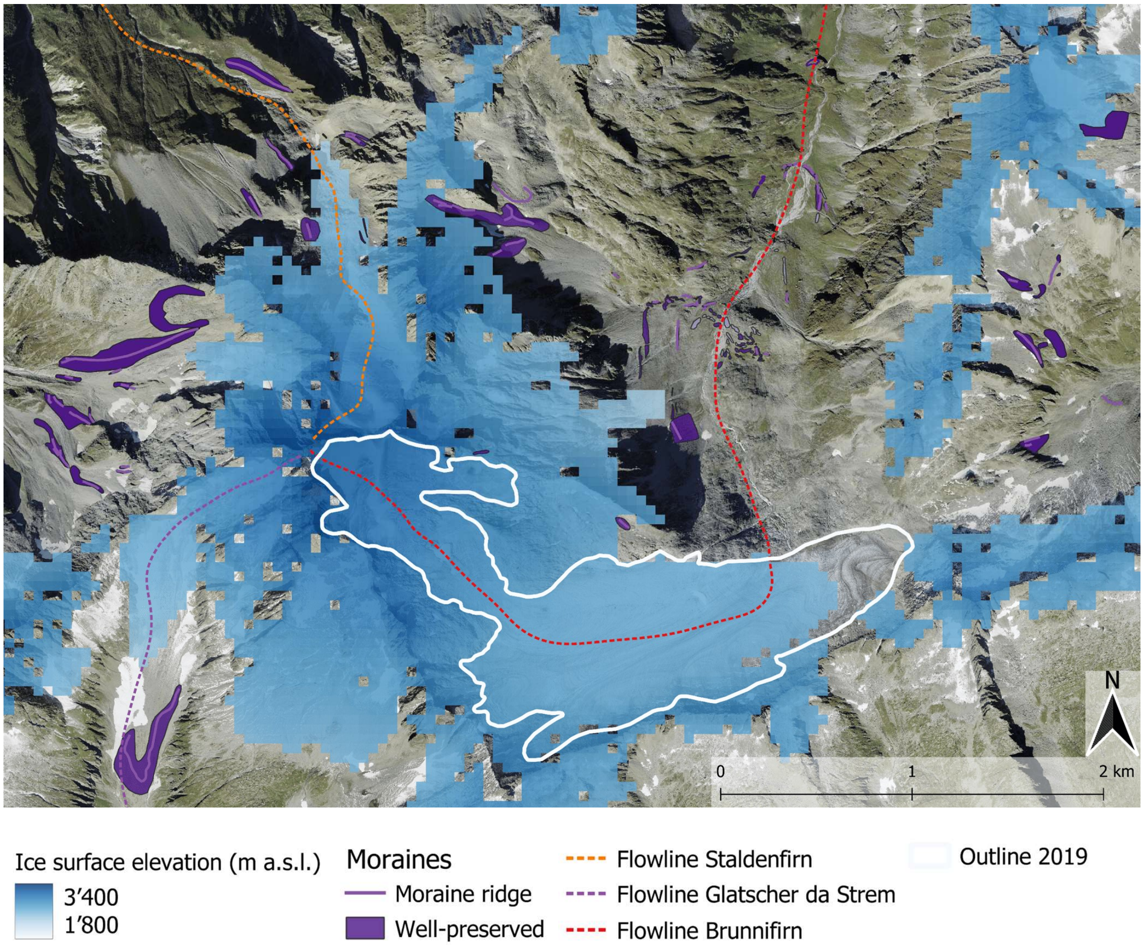

Figure 42: *Steady state output with an ELA of 2730. This is the closest approximation of a steady state to today's extent, as lowering the ELA by just a few meters leads to the steady state extent overflowing the edge of the plain. But compared to the mapped 2019 aerial image glacier outline, the model underestimates the ice extent in the eastern part of the plain but overestimates the eastern flank of Oberalpstock and Staldenfirn and Glatscher da Strem. Background map: swisstopo (2023).*

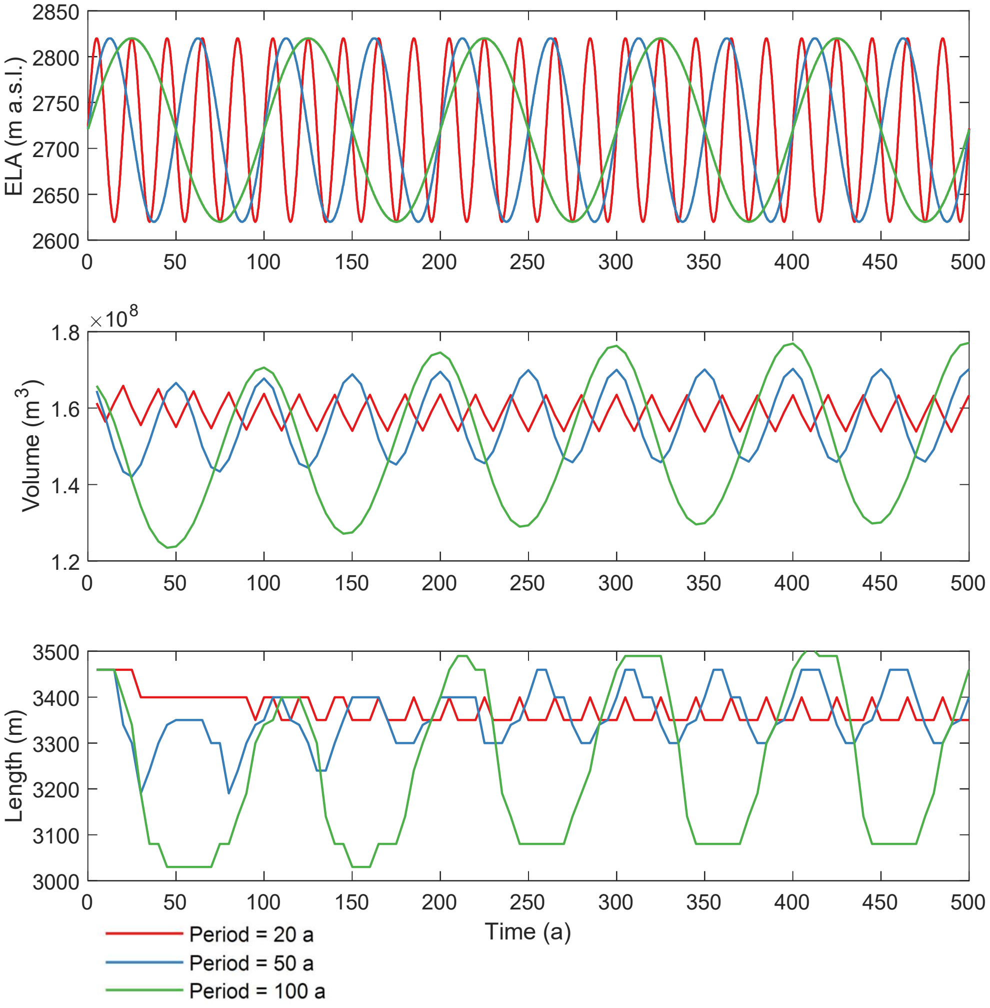

Figure 43: *Sinus ELA forcing around an ELA0 of 2720 m a.s.l., with sinus periods of 20, 50, and 100 years.*

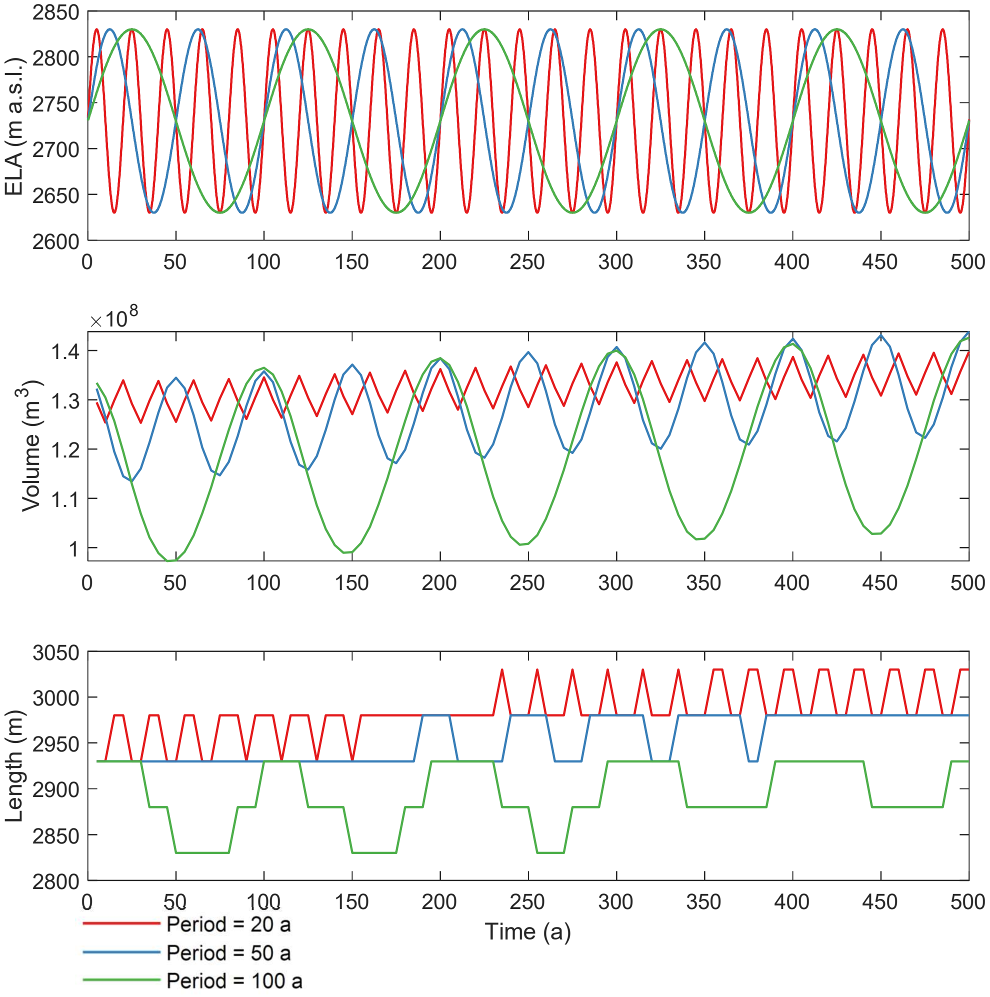

Figure 44: *Sinus ELA forcing around an ELA0 of 2730 m a.s.l., with sinus periods of 20, 50, and 100 years.*

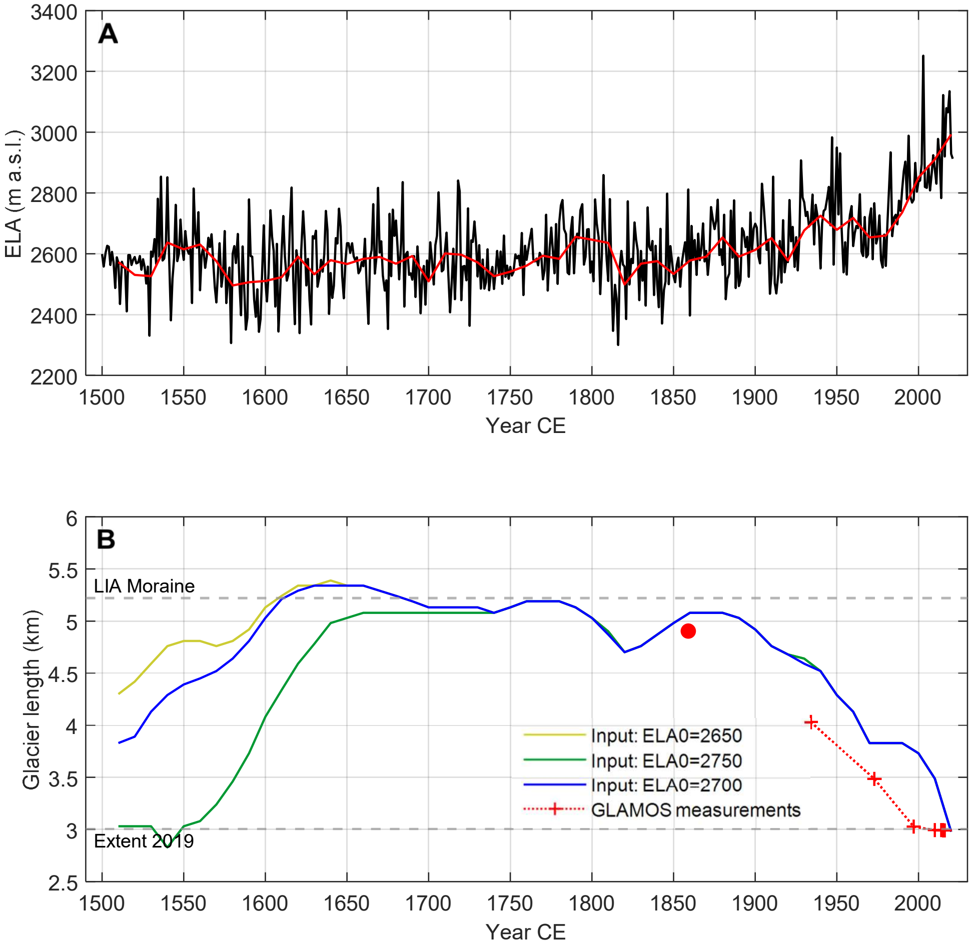

Figure 45: *(A) ELA history used for LIA modeling, with ELA0 = 2700 and* $ELA_{fc} = 120$*. (B) Plot of the length evolution of Brunnifirn with different steady state starting ice geometries (yellow, orange, and green line). The blue line represents an overlap of at least two of the curves, therefore also showing the point when the glacier has adjusted to the climate signal, independent of the input. The red dot is the glacier length on the Siegfried map (data content from 1859 CE, according to swisstopo, 2023). The red crosses display the measurements recorded by GLAMOS.*

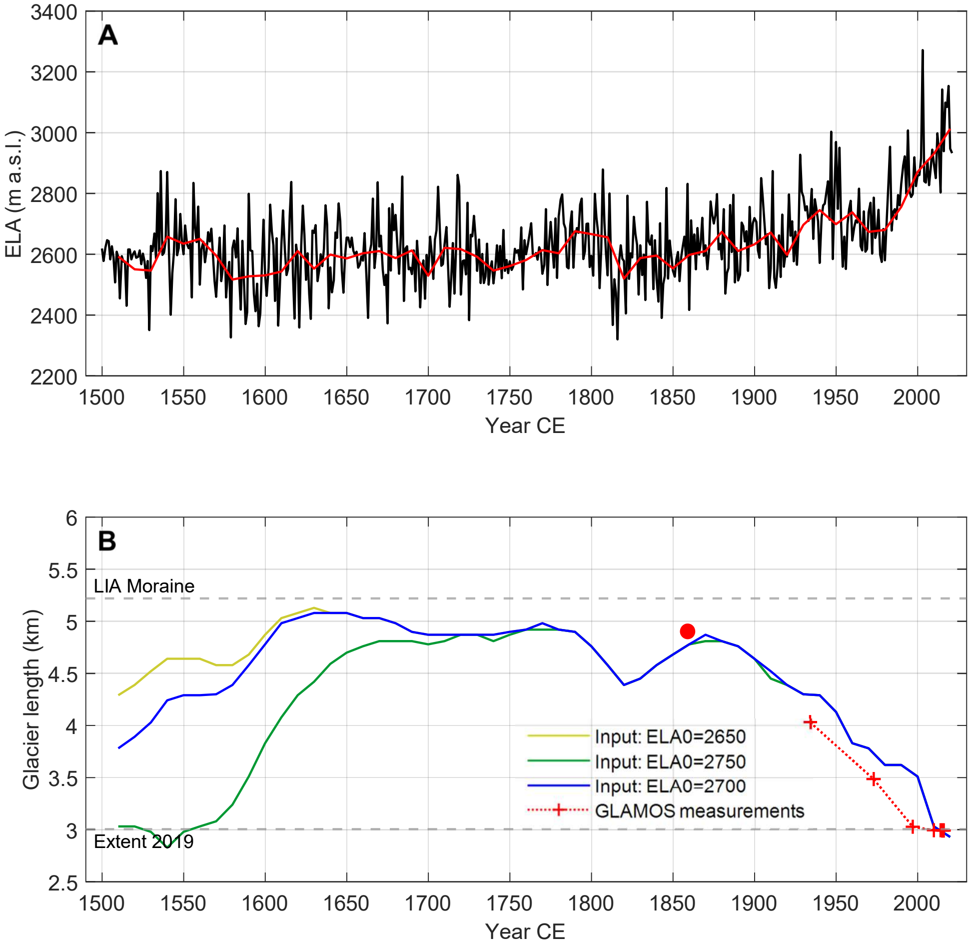

Figure 46: *(A) ELA history used for LIA modeling, with* $ELA0 = 2720$ *and* $ELA_{fc} = 120$. *(B) Plot of the length evolution of Brunnifirn with different steady state starting ice geometries (yellow, orange, and green line). The blue line represents an overlap of at least two of the curves, therefore also showing the point when the glacier has adjusted to the climate signal, independent of the input. The red dot is the glacier length on the Siegfried map (data content from 1859 CE, according to swisstopo, 2023). The red crosses display the measurements recorded by GLAMOS.*

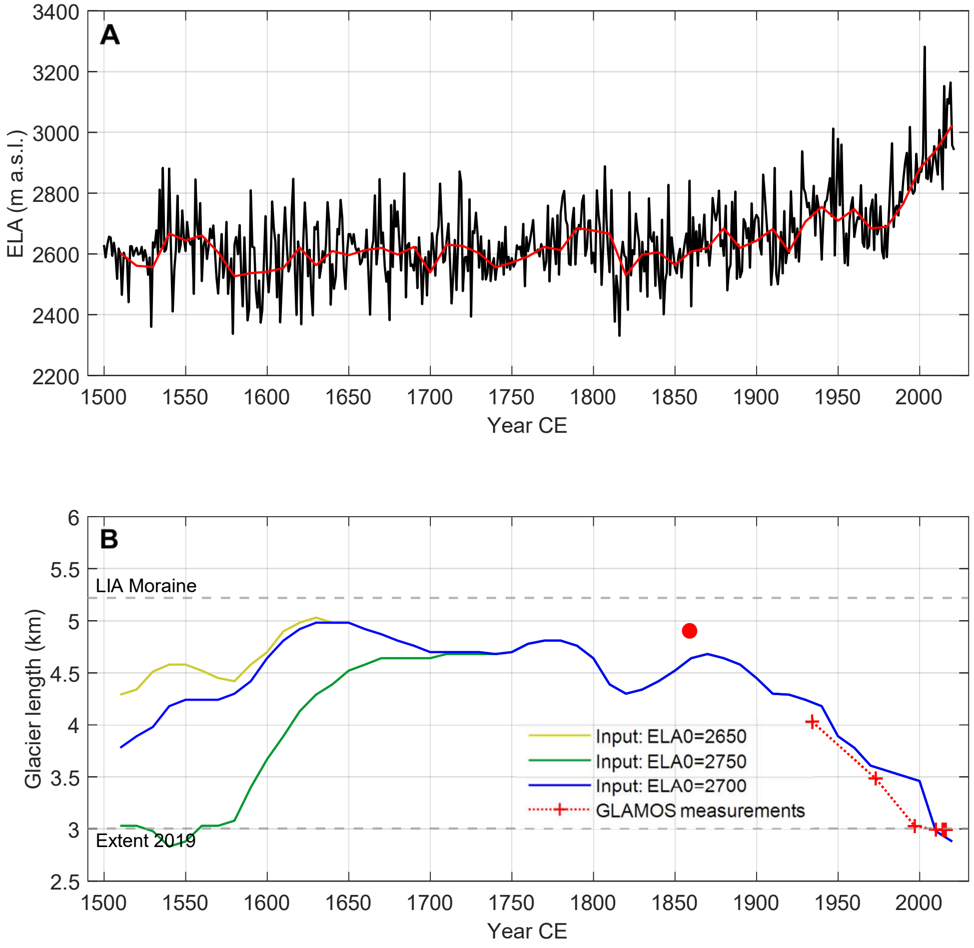

Figure 47: *(A) ELA history used for LIA modeling, with ELA = 2730 and* $ELA_{fc} = 120$*. (B) Plot of the length evolution of Brunnifirn with different steady state starting ice geometries (yellow, orange, and green line). The blue line represents an overlap of at least two of the curves, therefore also showing the point when the glacier has adjusted to the climate signal, independent of the input. The red dot is the glacier length on the Siegfried map (data content from 1859 CE, according to swisstopo, 2023). The red crosses display the measurements recorded by GLAMOS.*

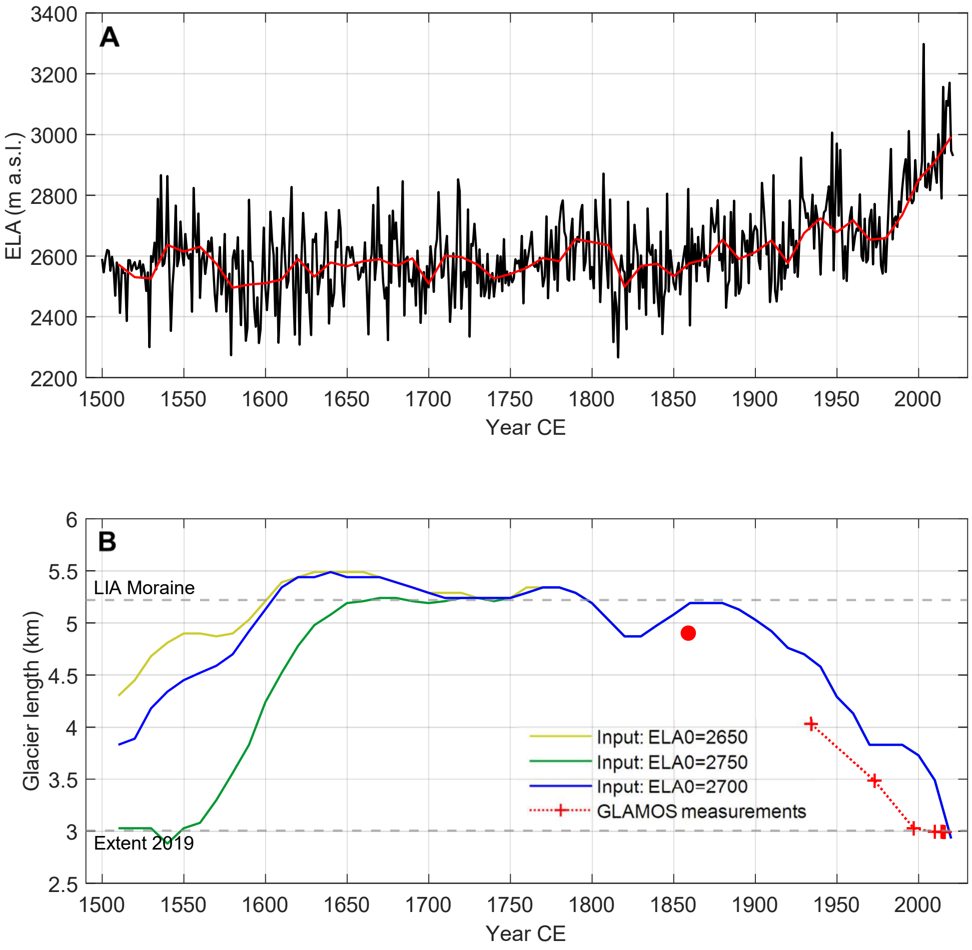

Figure 48: *(A) ELA history used for LIA modeling, with* $ELA0 = 2700$ *and* $ELA_{fc} = 130$*. (B) Plot of the length evolution of Brunnifirn with different steady state starting ice geometries (yellow, orange, and green line). The blue line represents an overlap of at least two of the curves, therefore also showing the point when the glacier has adjusted to the climate signal, independent of the input. The red dot is the glacier length on the Siegfried map (data content from 1859 CE, according to swisstopo, 2023). The red crosses display the measurements recorded by GLAMOS.*

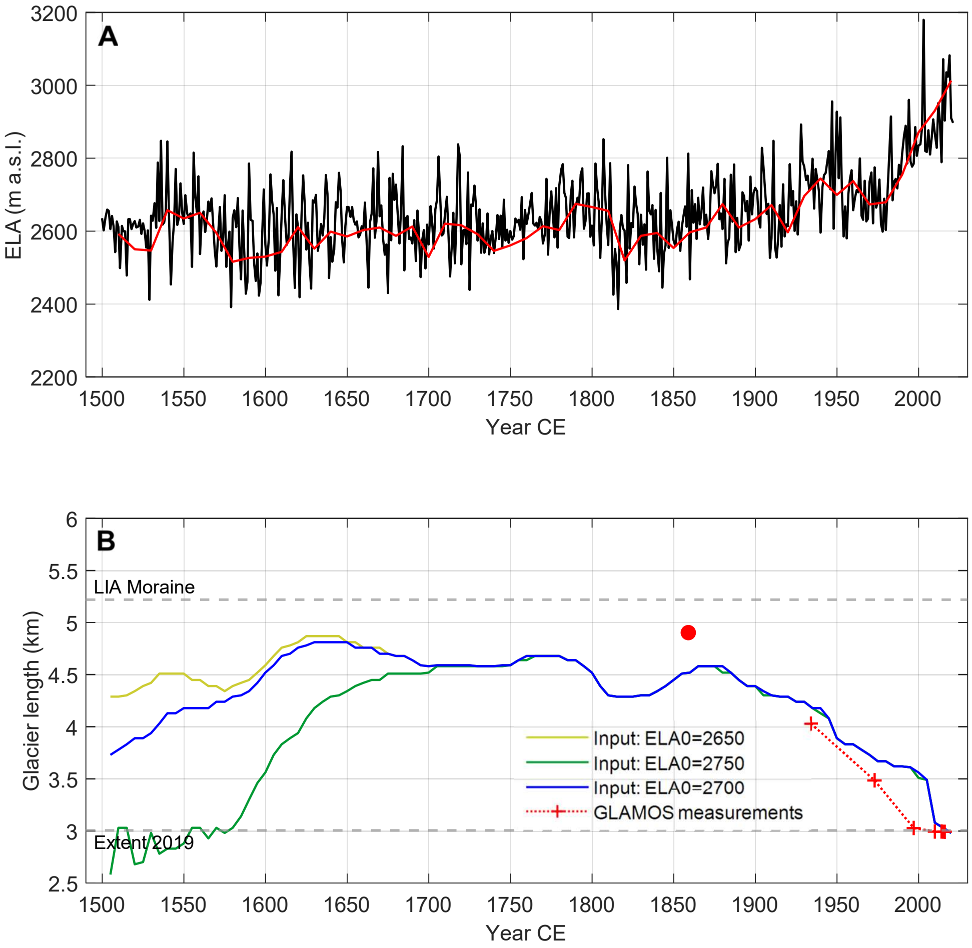

Figure 49: *(A) ELA history used for LIA modeling, with ELA0 = 2720 and* ELA_{fc} *= 100. (B) Plot of the length evolution of Brunnifirn with different steady state starting ice geometries (yellow, orange, and green line). The blue line represents an overlap of at least two of the curves, therefore also showing the point when the glacier has adjusted to the climate signal, independent of the input. The red dot is the glacier length on the Siegfried map (data content from 1859 CE, according to swisstopo, 2023). The red crosses display the measurements recorded by GLAMOS.*

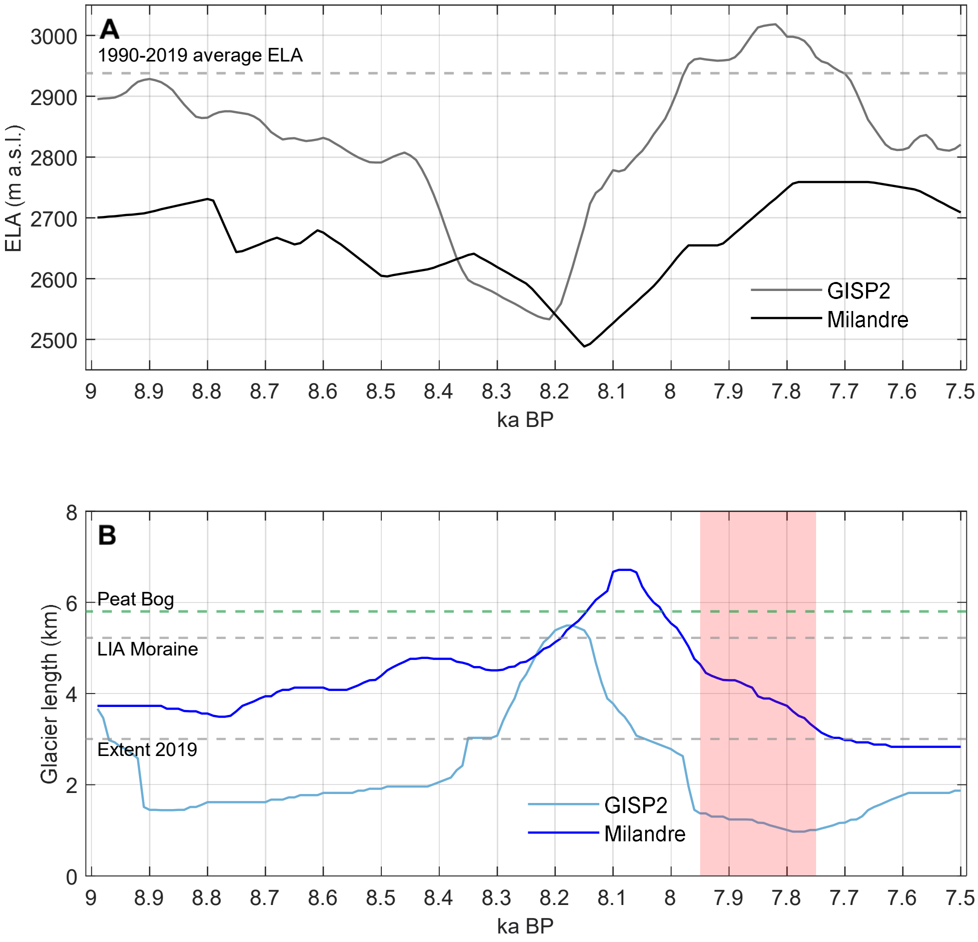

Figure 50: *Holocene modeling of the period the archeological artifacts are dated for (red box in plot B). Modeling was started well before the cold interval around 8.2 ka to eliminate any bias of the input geometry (steady state for 2720 m a.s.l. ELA). A) ELAs calculated for GISP2 and Milandre temperature reconstructions ($ELA_{fc} = 130$), with linear interpolation between data points. B) Brunnifirn length modeled from the two different ELA calculations. The gray dotted lines show known glacier extent as reference, the green dotted line shows the position of the peat bog which was radiocarbon age dated to ca 3.8–3.5 ka BP.*

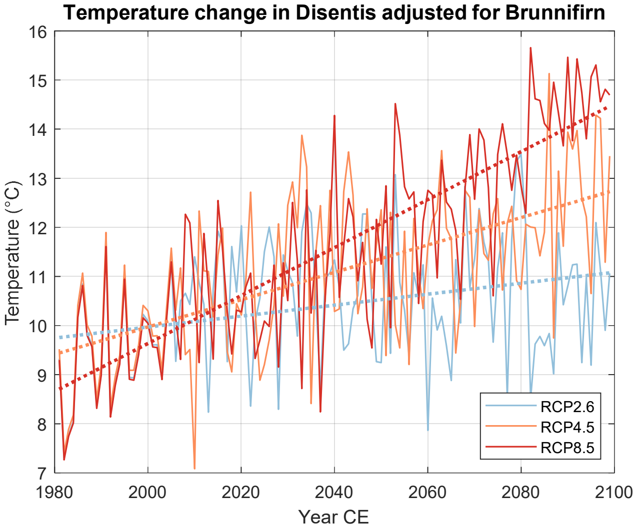

Figure 51: *CH2018 simulation (MPICSC-REMO1_MPIESM) temperature projections for three RCPs for Disentis (closest station to Brunnifirn).*

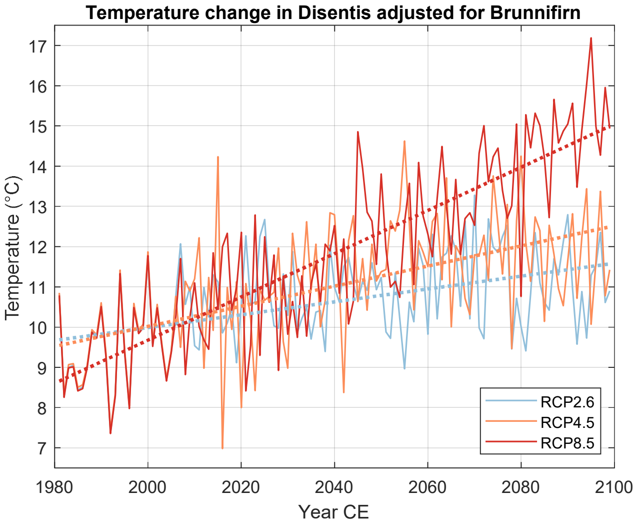

Figure 52: *CH2018 simulation (MPICSC-REMO2_MPIESM) temperature projections for three RCPs for Disentis (closest station to Brunnifirn).*

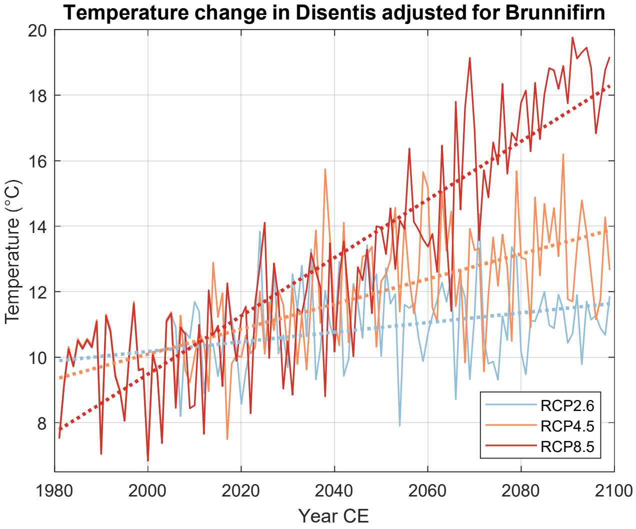

Figure 53: *CH2018 simulation (SMHI-RCA_ECEARTH) temperature projections for three RCPs for Disentis (closest station to Brunnifirn).*

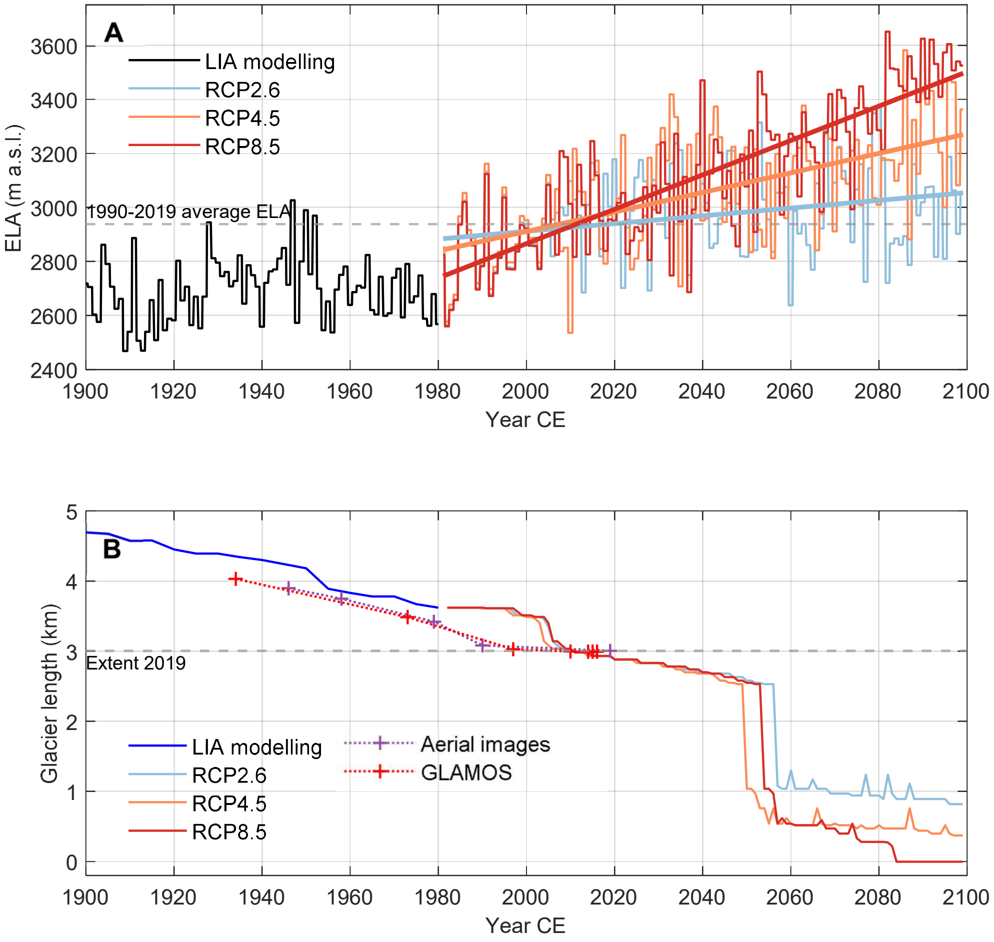

Figure 54: *Future evolution of Brunnifirn from 1981–2099 CE for three RCPs (CH2018 simulation MPICSC-REMO1_MPIESM), with result 1980 CE result of the 1500–2020 CE modeling. A) The bold lines are trends for the three RCPs. B) The almost vertical length change before 2060 CE marks the disappearance of a large dead ice body that remains in the plain. The steep upper part of the glacier however disconnects from the part in the plain already around 2030–2040 CE.*

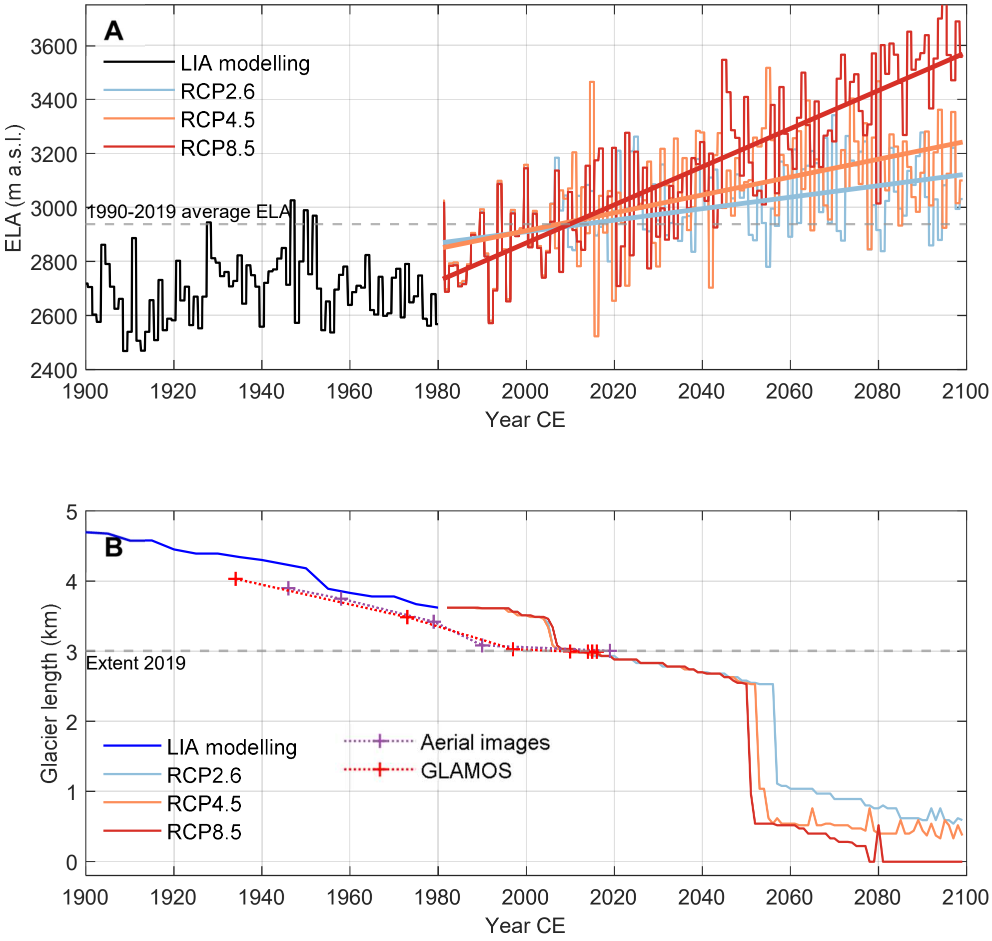

Figure 55: *Future evolution of Brunnifirn from 1981–2099 CE for three RCPs (CH2018 simulation MPICSC-REMO2_MPIESM), with result 1980 CE result of the 1500–2020 CE modeling. A) The bold lines are trends for the three RCPs. B) The almost vertical length change before 2060 CE marks the disappearance of a large dead ice body that remains in the plain. The steep upper part of the glacier however disconnects from the part in the plain already around 2030–2040 CE.*

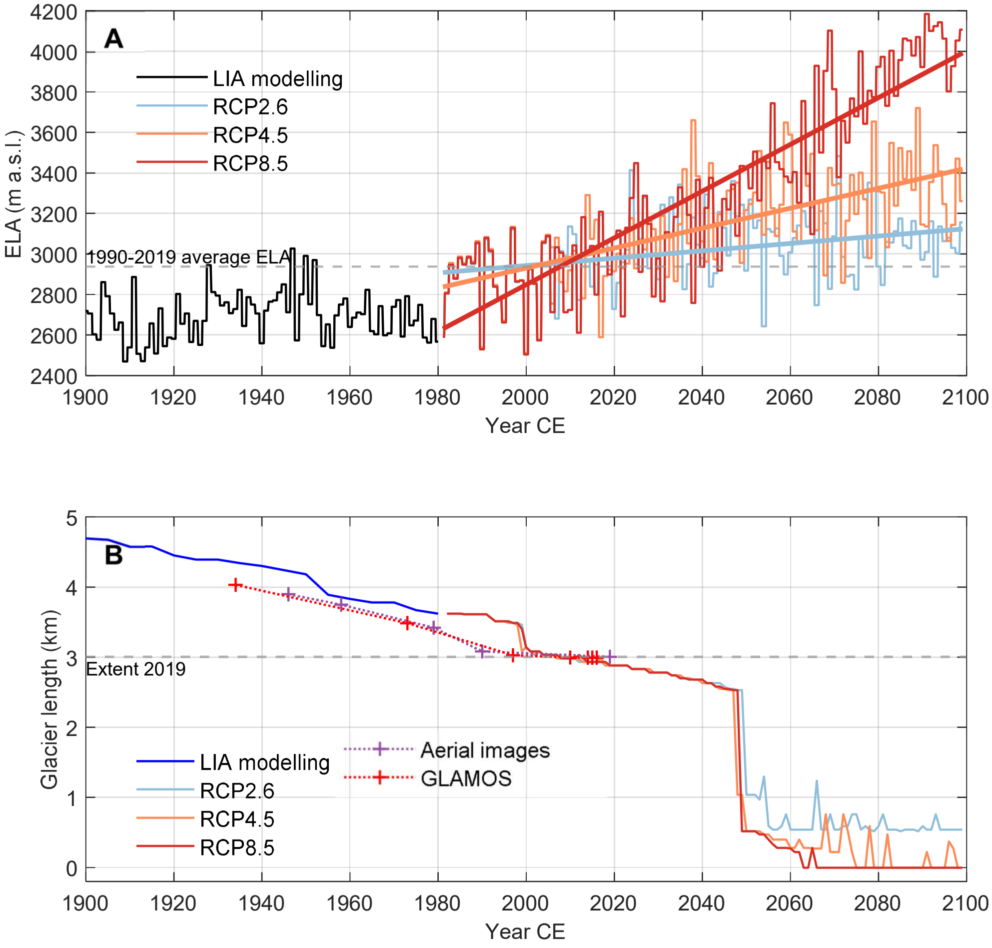

Figure 56: *Future evolution of Brunnifirn from 1981–2099 CE for three RCPs (CH2018 simulation SMHI-RCA_ECEARTH), with result 1980 CE result of the 1500–2020 CE modeling. A) The bold lines are trends for the three RCPs. B) The almost vertical length change before 2060 CE marks the disappearance of a large dead ice body that remains in the plain. The steep upper part of the glacier however disconnects from the part in the plain already around 2030–2040 CE.*

Personal declaration

I hereby declare that the submitted thesis is the result of my own, independent work. All external sources are explicitly acknowledged in the thesis.

J. Davidson

Zürich, 30.06.2023 Jonathan Davidson